TRANSPORTATION RESEARCH RECORD

510

Formerly issued as Highway Research Record

Soil Mechanics

7 reports prepared for the 53rd Annual Meeting of the Highway Research Board

subject areas

23 highway drainage
25 pavement design
26 pavement performance
31 bituminous materials and mixes
33 construction
34 general materials
61 exploration-classification (soils)
62 foundations (soils)
63 mechanics (earth mass)

TRB

TRANSPORTATION RESEARCH BOARD

NATIONAL RESEARCH COUNCIL

Washington, D. C., 1974

Transportation Research Record 510
Price $3.80
Edited for TRB by Marianne Cox Wilburn

subject areas
23 highway drainage
25 pavement design
26 pavement performance
31 bituminous materials and mixes
33 construction
34 general materials
61 exploration-classification (soils)
62 foundations (soils)
63 mechanics (earth mass)

These papers report research work of the authors that was done at institutions named by the authors. The papers were offered to the Transportation Research Board of the National Research Council for publication and are published here in the interest of the dissemination of information from research, one of the major functions of the Transportation Research Board.

Before publication, each paper was reviewed by members of the TRB committee named as its sponsor and accepted as objective, useful, and suitable for publication by the National Research Council. The members of the review committee were chosen for recognized scholarly competence and with due consideration for the balance of disciplines appropriate to the subject concerned.

Responsibility for the publication of these reports rests with the sponsoring committee. However, the opinions and conclusions expressed in the reports are those of the individual authors and not necessarily those of the sponsoring committee, the Transportation Research Board, or the National Research Council.

Each report is reviewed and processed according to the procedures established and monitored by the Report Review Committee of the National Academy of Sciences. Distribution of the report is approved by the President of the Academy upon satisfactory completion of the review process.

The National Research Council is the principal operating agency of the National Academy of Sciences and the National Academy of Engineering, serving government and other organizations. The Transportation Research Board evolved from the 54-year-old Highway Research Board. The TRB incorporates all former HRB activities but also performs additional functions under a broader scope involving all modes of transportation and the interactions of transportation with society.

LIBRARY OF CONGRESS CATALOGING IN PUBLICATION DATA

National Research Council. Highway Research Board. Soil mechanics.

(Transportation research record; 510)

1. Soil mechanics—Addresses, essays, lectures. 2. Roads—Foundations—Addresses, essays, lectures. 3. Pavements—Addresses, essays, lectures. I. Title. II. Series.
TE7.H5 no. 510 [TE210] 380.5'08s [625.7'32]
ISBN 0-309-02354-8 74-32373

CONTENTS

FOREWORD

This RECORD will be of interest to soils engineers and designers concerned with the theories of pavement design and performance, pipes and culverts, reinforced earth, and bearing capacities.

Allen and Thompson in their study of resilient response of granular materials show that the existing state of stress significantly influences the resilient modulus determination and that factors such as load duration, stress sequence, and repetitions have negligible effect. Poisson's ratio is greatly overestimated in the normal constant confining pressure test but can be more accurately expressed as a function of the principal stress ratio. McLean and Monismith found through repeated load test studies that, within the range studied, subgrade stiffness appeared to have little influence on the accumulation of pavement deformations in the asphalt-bound layer, and the effect of the stiffness of the asphalt concrete itself was significant. Kennedy made a study of the variation, both within the project and the state, of tensile strength, modulus of elasticity, and Poisson's ratio for black-base materials in an effort to provide limits of variability for projected tensile and elastic pavement design systems. It was concluded that a useful single variation value could not be established for the state because characteristic values were project dependent.

Spannagel, Davis, and Bacher present the analysis of large-scale field studies of flexible pipe culverts that led them to recommend that the ring compression method with a safety factor of 4 and a 70 percent increase in density be adopted for future designs.

Chang, Forsyth, and Beaton make a recommendation based on field performance records that reinforced earth embankments be designed using Rankine's state-of-stress theory and a newly introduced strain energy principle.

Livneh and Greenstein describe a method for determining the critical bearing capacity of a footing on saturated, undrained clays. Failure is shown to occur to the surface when it is determined by depth-dependent anisotropic strength properties than when it is determined by previously accepted theories. Krizek and Alonso present a new solution to the analysis of the deformational behavior of beams on nonhomogeneous bases. Strict limitation on differential settelements may impose additional requirements to refine the ordinary analysis and be able to present a probabilistic answer with greater confidence.

RESILIENT RESPONSE OF GRANULAR MATERIALS SUBJECTED TO TIME-DEPENDENT LATERAL STRESSES

John J. Allen, Department of Civil Engineering,
United States Air Force Academy; and
Marshall R. Thompson, Department of Civil Engineering,
University of Illinois at Urbana-Champaign

Present methods of determining the resilient parameters (modulus of deformation and Poisson's ratio) of granular materials for use in the analysis of pavement structures subjected to moving wheel loads are based on the results of laboratory repeated-load triaxial tests in which the minor principal stress (chamber pressure) is held constant. However, as a wheel load moves over an element of an actual pavement structure, the element is subjected to both time-dependent lateral and vertical stresses. The purpose of this study was to determine the effects of this nonconstant state of stress on the observed resilient properties of granular materials. Based on the current literature, certain factors thought to affect the resilient properties of granular materials were identified. Among these factors, which were later investigated during the laboratory phase, were density level, type of material, load duration, and number of load repetitions. Nonlinear, finite-element analyses of typical pavement sections were used to establish typical horizontal and vertical stress pulses. The characteristic stress pulses were used to test specimens during the laboratory investigation. It was shown that factors such as load duration, stress sequence, and number of repetitions have negligible effects on the resilient parameters. Nonlinear regression analyses of the laboratory data indicated that the resilient modulus is significantly influenced by the state of stress in the material and may be expressed as a function of the first invariant of the stress tensor. Poisson's ratio may be expressed as a function of the principal stress ratio. The effects of density and material type are small compared with the stress-dependent effects. The resilient modulus determined by the constant-confining-pressure test was found to vary insignificantly from that determined by the variable-confining-pressure test. However, the constant-confining-pressure test data greatly overestimate Poisson's ratio because of the anisotropic nature of the material and the greater volume change that is observed in that type of test.

•ACCURATE prediction of the fatigue life of flexible pavements depends on proper assessment of stress and strain in the pavement under moving loads. Accuracy in pavement structural analysis has been facilitated by finite-element analytical techniques and layered, elastic computer solutions. But, paving materials must be characterized for use with these computer techniques. Therefore, efforts have been made to determine essential stress-strain relations for pavement components.

OBJECT

The object of this research was to assess the effects of nonconstant lateral pressures on the resilient response of granular materials. Predictive equations for material

Publication of this paper sponsored by Committee on Strength and Deformation Characteristics of Pavement Sections.

stiffness and Poisson's ratios were developed and are considered accurate for use in various analytical techniques, insofar as they are applied to the proper boundary value problem. That is, these are pseudoelastic material parameters that define the response of an unbound granular base-course material to stresses applied at typical vehicle speeds. These results are not intended to serve as a model for predicting accumulated plastic deformations (rutting). But, they have direct application to the problem of predicting transient, "resilient" pavement deflections, and, therefore, serve as a step toward the successful prediction of flexible pavement fatigue life.

Despite the knowledge of the heavy influence of confining stresses on the resilient parameters, there have been no published results of tests where lateral stresses were varied simultaneously with axial stress on a time scale that would simulate transient wheel loadings. Because this condition represents the stress that occurs in an actual pavement structure subjected to moving wheel loads, the purpose of this research was to simulate field conditions in the laboratory by repeated-load, variable-confining-pressure, triaxial tests.

STRESS PULSES IN FLEXIBLE PAVEMENT SYSTEMS

Three pavement structural sections were analyzed by a nonlinear finite-element technique:

1. A runway section consisting of 3 in. (7.6 cm) of asphalt concrete, 6 in. (15.2 cm) of granular base, 15 in. (38.1 cm) of granular subbase over a subgrade with a CBR equal to 4;
2. A highway section consisting of 3 in. (7.6 cm) of asphalt concrete, 6 in. (15.2 cm) of granular base, 10 in. (25.4 cm) of granular subbase over a subgrade with a CBR equal to 4; and
3. An "inverted" section similar to the highway section except that the granular subbase was replaced by a 10-in.- (25.4-cm-) thick lime-stabilized subgrade layer.

A uniform surface pressure of 100 psi (690 kPa) distributed over a circular area with a 10-in. (25.4-cm) radius was applied to the runway section. For the other 2 sections the surface pressure was 80 psi (552 kPa) and the radius was 6 in. (15.2 cm). All material properties were chosen as representative values that were determined from a literature survey.

For all 3 sections, the shapes of the stress distributions were related to their depth within the section. The major principal stress pulse and the vertical stress pulse, although generally sinusoidal, were peaked more sharply in the upper part of the base course and had shallower slopes in the lower base and subbase. Major principal stresses are always greater than vertical stresses, except directly under the center of the load where they are equal. Therefore, the major principal stress pulse was somewhat longer than the vertical stress pulse. This difference increased with depth. Barksdale reported the same trends (2).

Radial and minor principal stress pulses were similar in shape for the runway and highway sections. These pulse shapes also were related to depth within the system. In the upper portions of the base, these pulses were more or less flat-topped. In the extreme upper portion of the base the stresses were not exactly under the center of the load, but at a slight radial offset. Both types became more sinusoidal as depth increased.

Analysis of the inverted section revealed significant changes in stress distributions. Although the vertical and major principal stress pulses were the same shape as those for the highway section, their magnitudes were as much as 100 percent greater throughout the granular layer. More significant, though, was the drastic increase in the radial and minor principal stresses throughout the granular layer of the inverted section. The reduction in confining pressure beneath the center of the load was eliminated completely and a sinusoidal pulse shape resulted. The magnitude of the minor principal stress pulse directly under the load increased by 500 to 800 percent. As discussed by Allen, the increased stress levels in the granular layers of the inverted section exert significant influence over the load response of the pavement structure (1). The use of a buried

stabilized layer is 1 method of exploiting the stress-dependent nature of granular paving materials to the designer's advantage.

The half-sinusoid was selected as the basic pulse shape for this study because it is the most general shape of all stress distributions and because most standard laboratory function generators, in combination with hydraulic testing equipment, can apply it. Simulation of stress at various depths within the granular layer was accomplished by varying the pulse duration and magnitude.

LABORATORY TESTING PROGRAM

Materials

The following materials were tested during this study:

1. A well-graded crushed limestone,
2. A well-graded siliceous gravel, and
3. A blend of the gravel and limestone.

The blend was obtained by adding equal percentages of the crushed stone and gravel on the No. 4 sieve to the gravel material passing the No. 4. The maximum size of the aggregate was 1½ in. (3.81 cm) with 5 percent passing the No. 200 sieve. The plasticity index was 5 for the crushed stone and 9 for the gravel. All specimens were prepared to the same gradation.

Specimen Preparation

All specimens were prepared on the chamber base plate by drop-hammer compaction in a 6- by 12-in. (15.2- by 30.5-cm) split mold that attached to the base plate by tie rods and wing nuts. The hammer had a 2.0-in. (5.1-cm) diameter striking face, weighed 10 pounds (4.5 kg), and had a fall of 18 in. (45.7 cm). Specified densities were attained by varying the number of layers per specimen and the number of blows per layer.

Each specimen was encased in 2 latex membranes to prevent leakage during the test. This procedure was effective because when moisture contents were determined after testing, they varied only minimally from the original moisture contents.

Nine specimens were tested during the primary test series (3 materials and 3 density levels). Table 1 gives the properties of the specimens. The high density and accompanying moisture content given in Table 1 corresponded to maximum density and optimum moisture resulting from an AASHO T 180 compaction. The low density and optimum moisture content corresponded to the maximum density and optimum moisture from the AASHO T 99 test. The intermediate levels were moisture-density values between the peaks of the 2 compaction curves.

Because the object of this study was to compare the response of the specimens to the 2 types of stress pulses (variable and constant confining pressures), and because these were nondestructive tests, only 1 specimen of each material at any density level was tested. The preliminary test series indicated that any 1 specimen could be tested at all stress levels without significantly affecting the results. This procedure eliminated the possibility that unplanned specimen-to-specimen variations in density and moisture content would occur.

Testing Equipment and Instrumentation

The laboratory investigation portion of this study was conducted at the U.S. Army Corps of Engineers Construction Engineering Research Laboratory at Champaign, Illinois. The unique aspect of this study, that is, the requirement that the triaxial chamber confining pressure be varied simultaneously with the axial load, was satisfied by a closed-loop testing system. Axial stress was applied to the specimen through a hydraulic-actuated piston. The chamber pressure was varied by a hydraulic-actuated piston that reacted directly on the chamber fluid; water, in this case. Program input was provided by 2 function generators, 1 connected to the axial load controller and the other connected to the confining pressure controller. It was necessary to use 2 function generators to allow for a slight delay in the confining pressure pulse. This delay was

caused by compressibility of the chamber fluid and friction loss in the line connecting the chamber and the chamber pressure supply. This procedure made it possible to apply lateral and axial stress pulses to the specimen simultaneously.

The axial load was monitored by a load cell mounted on the test frame above the triaxial chamber. Chamber pressure was monitored by a pressure transducer installed at the base of the triaxial chamber. Axial deformation was measured over the central half of the specimen by 2 optical trackers.

Radial deformation was measured by sensors [4-in.- (10.2-cm-) diameter, disk-shaped coils of wire] that were mounted at midheight of the specimen and held in place by a 2-in.- (5.1-cm-) wide rubber strip cut from a triaxial membrane.

A dial gauge mounted on top of the triaxial chamber and a linear variable differential transformer on the actuator of the test frame were used to monitor nonrecoverable deformations and provided a backup system for obtaining resilient strain data. All stress and deformation data were recorded on an 8-track oscillograph printer.

Preliminary Tests

To aid in designing the primary test series, the following 3 preliminary tests, described in detail by Allen (1), were carried out on the crushed stone and gravel specimens:

1. A stress history test in which the specimens were subjected to 10,000 stress repetitions at 2 stress levels;
2. A stress sequence test in which the specimens were subjected to 100 stress repetitions at each of several increasing and decreasing stress levels; and
3. A stress pulse duration test in which the pulse duration was varied from 0.04 to 1.00 second.

These tests on both material types yielded results similar to those reported by Hicks (8). Specifically, the resilient response of these materials after 25 to 100 stress repetitions represented the response determined after several thousand stress repetitions; 1 specimen could be used to measure the resilient response over a wide range of stress levels, and these stresses could be applied in any order; and, the resilient response of these materials was affected only minimally by variations from 0.04 to 1.00 second in stress pulse duration.

Based on the preliminary test results, the stress levels given in Table 2 were selected for the primary test series. They were applied to each specimen in the order given and had a pulse duration of 0.15 sec and a frequency of 20 repetitions per min.

PRIMARY TEST SERIES

Methods of Computing Resilient Modulus, E_r, and Resilient Poisson's Ratio, ν_r

The resilient modulus, as computed from results of constant-confining-pressure triaxial tests (CCP tests), is the ratio of the repeated deviator stress, σ_1-σ_3, to recoverable axial strain, ϵ_a. The resilient Poisson's ratio is the ratio of recoverable lateral strain, ϵ_l, to recoverable axial strain, ϵ_a. This method of computation is the same as would apply to an isotropic, linear, elastic material under uniaxial stress conditions. The nature of the CCP test, in which the specimen consolidates under a constant chamber pressure before the dynamic increment of stress is applied in the axial direction, has led to general acceptance of this method of determining resilient parameters. However, the nature of the variable-confining-pressure triaxial test (VCP test), in which lateral stress is applied dynamically and simultaneously with axial stress, is such that to compute the resilient modulus as described above would ignore the effect of Poisson's ratio on axial strains and overestimate the modulus. Therefore, it was necessary to use the 3-dimensional stress-strain relations for isotropic, linear, elastic material:

Table 1. Test specimens.

Specimen	Material	Density (lb/ft^3)	Moisture (percent)	Saturation (percent)
HD-1	Crushed stone	138.0, high	5.7	78
MD-1	Crushed stone	134.0, intermediate	6.3	73
LD-1	Crushed stone	130.0, low	7.0	70
HD-2	Gravel	139.4, high	6.3	82
MD-2	Gravel	134.0, intermediate	6.5	74
LD-2	Gravel	131.0, low	6.7	69
HD-3	Blend	139.5, high	6.3	88
MD-3	Blend	134.5, intermediate	6.8	78
LD-3	Blend	131.0, low	7.2	74

Note: 1 lb/ft^3 = 16 kg/m^3.

Table 2. Test schedule.

Stress Level (psi)			Confining Pressure	Stress Level (psi)			Confining Pressure
σ_3	σ_1	σ_1/σ_3		σ_3	σ_1	σ_1/σ_3	
2	8	4	Variable	8	56	7	Variable
2	12	6	Variable	8	12	1.5	Constant
2	16	8	Variable	8	24	3	Constant
2	8	4	Constant	8	40	5	Constant
2	12	6	Constant	8	56	7	Constant
2	16	8	Constant	11	22	2	Constant
5	10	2	Constant	11	44	4	Constant
5	15	3	Constant	11	66	6	Constant
5	25	5	Constant	11	22	2	Variable
5	35	7	Constant	11	44	4	Variable
5	45	9	Constant	11	66	6	Variable
5	10	2	Variable	15	25	1.6	Variable
5	15	3	Variable	15	45	3	Variable
5	25	5	Variable	15	60	4	Variable
5	35	7	Variable	15	75	5	Variable
5	45	9	Variable	15	25	1.6	Constant
8	12	1.5	Variable	15	45	3	Constant
8	24	3	Variable	15	60	4	Constant
8	40	5	Variable	15	70	4.7	Constant

Note: All stress levels were applied for 100 repetitions. One pulse duration of 0.15 second was used.
1 psi = 6.89 kPa.

Table 3. Regression equations for E_r models from primary test data.

Specimen	Type of Test	Model, $E_r = f(\theta)$			Model, $E_r = f(\sigma_3)$		
		Equation	Correlation Coefficient	Standard Error	Equation	Correlation Coefficient	Standard Error
HD-1	VCP	$6,635\theta^{0.40}$	0.930[a]	3,144	$18,010\sigma_3^{0.28}$	0.669[b]	6,338
MD-1	VCP	$1,793\theta^{0.70}$	0.992[a]	1,463	$8,556\sigma_3^{0.57}$	0.794[a]	7,014
LD-1	VCP	$2,113\theta^{0.65}$	0.982[a]	2,058	$8,410\sigma_3^{0.57}$	0.819[a]	6,227
HD-2	VCP	$7,766\theta^{0.32}$	0.767[a]	3,996	$18,480\sigma_3^{0.19}$	0.515[c]	5,338
MD-2	VCP	$6,995\theta^{0.33}$	0.906[a]	2,202	$15,738\sigma_3^{0.23}$	0.664[b]	3,897
LD-2	VCP	$1,613\theta^{0.69}$	0.973[a]	2,033	$7,924\sigma_3^{0.51}$	0.781[a]	5,473
HD-3	VCP	$6,891\theta^{0.45}$	0.980[a]	2,035	$18,951\sigma_3^{0.35}$	0.832[a]	5,638
MD-3	VCP	$7,725\theta^{0.33}$	0.981[a]	1,042	$15,806\sigma_3^{0.26}$	0.841[a]	2,890
LD-3	VCP	$4,562\theta^{0.43}$	0.856[a]	3,367	$14,516\sigma_3^{0.24}$	0.498[c]	5,648
HD-1	CCP	$2,376\theta^{0.68}$	0.997[a]	1,149	$12,454\sigma_3^{0.55}$	0.845[a]	7,896
MD-1	CCP	$4,928\theta^{0.46}$	0.973[a]	1,950	$14,254\sigma_3^{0.39}$	0.872[a]	4,115
LD-1	CCP	$3,083\theta^{0.59}$	0.962[a]	3,132	$11,068\sigma_3^{0.53}$	0.909[a]	4,813
HD-2	CCP	$4,596\theta^{0.50}$	0.741[a]	8,063	$11,128\sigma_3^{0.54}$	0.803[a]	7,157
MD-2	CCP	$8,016\theta^{0.31}$	0.803[a]	3,551	$14,729\sigma_3^{0.31}$	0.838[a]	3,247
LD-2	CCP	$2,849\theta^{0.56}$	0.882[a]	4,289	$8,517\sigma_3^{0.55}$	0.916[a]	3,641
HD-3	CCP	$5,989\theta^{0.48}$	0.932[a]	4,254	$16,433\sigma_3^{0.45}$	0.922[a]	4,542
MD-3	CCP	$6,459\theta^{0.37}$	0.829[a]	3,977	$13,379\sigma_3^{0.37}$	0.873[a]	3,471
LD-3	CCP	$2,966\theta^{0.60}$	0.882[a]	4,962	$9,079\sigma_3^{0.58}$	0.914[a]	4,260

[a]Significant at $\alpha = 0.001$. [b]Significant at $\alpha = 0.01$. [c]Significant at $\alpha = 0.05$.

Table 4. Regression equations for υ_r models from primary test data.

Specimen	Type of Test	$\upsilon_r = f(\sigma_1/\sigma_3)$	Correlation Coefficient	Standard Error
HD-1	VCP	$0.62 - 0.19 (\sigma_1/\sigma_3) + 0.04 (\sigma_1/\sigma_3)^2 - 0.002 (\sigma_1/\sigma_3)^3$	0.907[a]	0.026
MD-1	VCP	$0.47 - 0.07 (\sigma_1/\sigma_3) + 0.02 (\sigma_1/\sigma_3)^2 - 0.001 (\sigma_1/\sigma_3)^3$	0.838[a]	0.045
LD-1	VCP	$0.60 - 0.14 (\sigma_1/\sigma_3) + 0.02 (\sigma_1/\sigma_3)^2 - 0.0007 (\sigma_1/\sigma_3)^3$	0.881[a]	0.036
HD-2	VCP	$-0.12 + 0.45 (\sigma_1/\sigma_3) - 0.09 (\sigma_1/\sigma_3)^2 + 0.005 (\sigma_1/\sigma_3)^3$	0.645[b]	0.085
MD-2	VCP	$0.46 + 0.01 (\sigma_1/\sigma_3) - 0.01 (\sigma_1/\sigma_3)^2 + 0.002 (\sigma_1/\sigma_3)^3$	0.889[a]	0.026
LD-2	VCP	$0.70 - 0.22 (\sigma_1/\sigma_3) + 0.04 (\sigma_1/\sigma_3)^2 - 0.002 (\sigma_1/\sigma_3)^3$	0.925[a]	0.027
HD-3	VCP	$0.49 + 0.01 (\sigma_1/\sigma_3) - 0.01 (\sigma_1/\sigma_3)^2 + 0.001 (\sigma_1/\sigma_3)^3$	0.766[a]	0.037
MD-3	VCP	$0.50 - 0.02 (\sigma_1/\sigma_3) - 0.003 (\sigma_1/\sigma_3)^2 + 0.0006 (\sigma_1/\sigma_3)^3$	0.561[c]	0.048
LD-3	VCP	$0.52 - 0.07 (\sigma_1/\sigma_3) + 0.006 (\sigma_1/\sigma_3)^2 + 0.0002 (\sigma_1/\sigma_3)^3$	0.840[a]	0.026
HD-1	CCP	$-0.17 + 0.30 (\sigma_1/\sigma_3) - 0.04 (\sigma_1/\sigma_3)^2 + 0.002 (\sigma_1/\sigma_3)^3$	0.895[a]	0.047
MD-1	CCP	$0.29 + 0.12 (\sigma_1/\sigma_3) - 0.01 (\sigma_1/\sigma_3)^2 + 0.0006 (\sigma_1/\sigma_3)^3$	0.746[a]	0.060
LD-1	CCP	$-0.01 + 0.28 (\sigma_1/\sigma_3) - 0.04 (\sigma_1/\sigma_3)^2 + 0.002 (\sigma_1/\sigma_3)^3$	0.723[a]	0.096
HD-2	CCP	$-0.14 + 0.46 (\sigma_1/\sigma_3) - 0.06 (\sigma_1/\sigma_3)^2 + 0.003 (\sigma_1/\sigma_3)^3$	0.429[d]	0.208
MD-2	CCP	$0.95 - 0.22 (\sigma_1/\sigma_3) + 0.04 (\sigma_1/\sigma_3)^2 - 0.002 (\sigma_1/\sigma_3)^3$	0.654[b]	0.144
LD-2	CCP	$-0.04 + 0.32 (\sigma_1/\sigma_3) - 0.05 (\sigma_1/\sigma_3)^2 + 0.003 (\sigma_1/\sigma_3)^3$	0.953[a]	0.056
HD-3	CCP	$-0.16 + 0.37 (\sigma_1/\sigma_3) - 0.05 (\sigma_1/\sigma_3)^2 + 0.003 (\sigma_1/\sigma_3)^3$	0.868[a]	0.073
MD-3	CCP	$-0.02 + 0.27 (\sigma_1/\sigma_3) - 0.03 (\sigma_1/\sigma_3)^2 + 0.001 (\sigma_1/\sigma_3)^3$	0.828[a]	0.091
LD-3	CCP	$-0.09 + 0.36 (\sigma_1/\sigma_3) - 0.05 (\sigma_1/\sigma_3)^2 + 0.003 (\sigma_1/\sigma_3)^3$	0.729[a]	0.121

[a]Significant at $\alpha = 0.001$. [b]Significant at $\alpha = 0.01$. [c]Significant at $\alpha = 0.02$. [d]Significant at $\alpha = 0.1$.

Figure 1. VCP test results—$E_r = f(\theta)$ model, specimen MD-1.

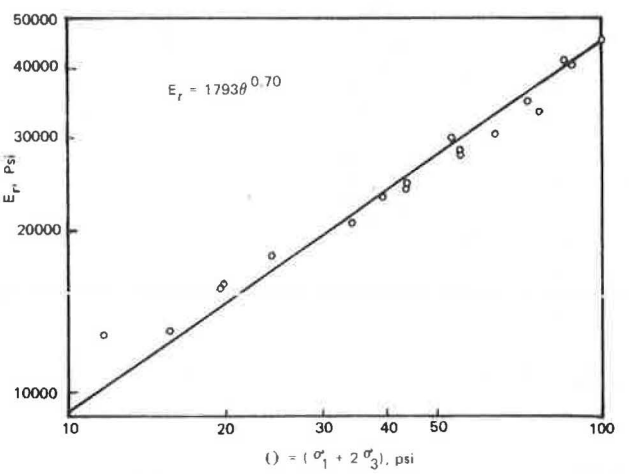

Figure 2. VCP test results—$\upsilon_r = f(\sigma_1/\sigma_3)$ model, specimen LD-2.

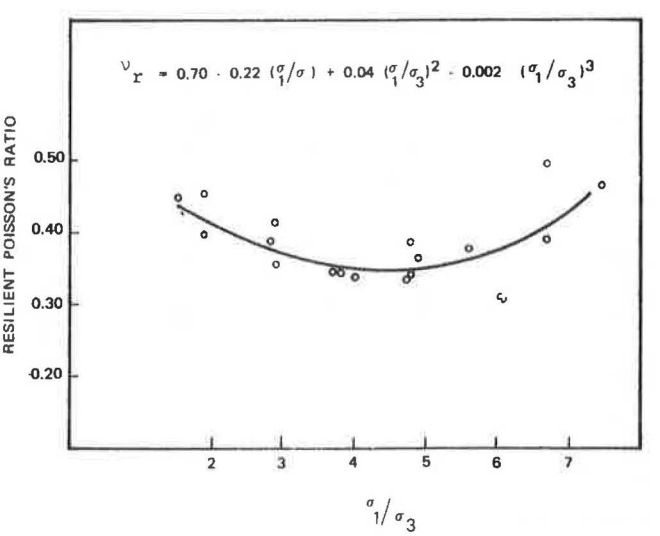

$$\epsilon_a = \frac{1}{E_r}(\sigma_a - 2\nu_r\sigma_r)$$
$$\epsilon_\ell = \frac{1}{E_r}[\sigma_a - \nu_r(\sigma_a + \sigma_r)] \quad (1)$$

where

σ_a = axial stress,
σ_r = radial stress,
ϵ_a = recoverable axial strain,
ϵ_ℓ = recoverable lateral (radial) strain,
E_r = resilient modulus, and
ν_r = resilient Poisson's ratio.

Statistical Analysis of Data

The VCP and CCP test data were analyzed by using linear regression techniques. E_r and ν_r were correlated with stress parameters σ_3; σ_1/σ_3; $\sigma_1 - \sigma_3$; and θ, the sum of the principal stresses. Comparison of the correlation coefficients and standard errors of the various models made possible selections of the models that most accurately fit the laboratory data. The data were analyzed by nonlinear regression techniques and the following models resulted:

$$E_r = K\,\theta^n$$
$$E_r = K'\sigma_3^{n'}$$
$$\nu_r = b_0 + b_1(\sigma_1/\sigma_3) + b_2(\sigma_1/\sigma_3)^2 + b_3(\sigma_1/\sigma_3)^3 \quad (2)$$

where

K, n, K′, n′, and b = constants from regression analysis;
$\theta = \sigma_1 + 2\sigma_3$;
σ_3 = minor principal stress; and
σ_1 = major principal stress.

The model for E_r based on θ yielded the highest correlation coefficients and lowest standard errors of all the models. But, the considerable scatter in the data associated with the σ_3 model resulted because it did not account for the effects of the axial stress on E_r. It is included because it has been proposed by other investigators. Tables 3 and 4 give the results of the statistical analyses.

Effects of Stress

Primary test results demonstrated that the resilient material parameters were affected much more significantly by changes in stress than by changes in any other factors. For example, the resilient modulus changed by as much as 400 percent over the range of stress encountered in a typical pavement system. The VCP and CCP test data show variations in the resilient modulus computed for different values of σ_1 at any 1 value of σ_3.

The model relating E_r to the first invariant of the stress tensor, θ, reduced the scatter in the data by accounting for the effects of all 3 principal stresses. Figure 1 shows this relation for intermediate density crushed stone, specimen MD-1. The higher correlation coefficients and lower standard errors associated with the θ model as compared to the σ_3 model also were obtained for the other specimens. The increase in E_r as θ increased is evident; Figure 1 indicates a 400 percent increase in E_r as θ increased from 10 to 80 psi (69 to 552 kPa). Although data from only 1 specimen are presented in Figure 1, the same trends were evident from the results obtained for all specimens.

The stress-dependent nature of the resilient Poisson's ratio is shown in Figure 2. The best fit to the laboratory data was obtained for all specimens by expressing ν_r as a function of σ_1/σ_3 (Eq. 2). Figure 2 shows this relationship for the VCP test data from

low density gravel, specimen LD-2. Of interest is the relatively flat slope of the curve through the range 2 to 7. This indicates that, because this range of stress ratios is typical of that found in pavement systems, pavement analyses that are based on a representative constant value of Poisson's ratio for granular layers might be appropriate. The validity of this observation is strengthened by the fact that the VCP test results for all specimens yielded for the same range of σ_1/σ_3 Poisson's ratio values very close to those shown in Figure 2.

Figure 3 shows ν_r values from the CCP test on the same specimen as shown in Figure 2. This figure, typical of the CCP results for all specimens, differs in 2 respects from the typical VCP results shown in Figure 2. First, the curve is concave downward throughout the range of interest, whereas the curve in Figure 2 is concave upward. Second, the values of ν_r are much higher (> 0.50) throughout the same range of σ_1/σ_3 for the CCP results than for the VCP. This contrast may indicate that the CCP test conditions caused the specimen to undergo more volume change than did the VCP test.

Effects of Density

The effects of variations in dry density, γ_d, on E_r are shown in Figure 4. In general, density effects were more pronounced at lower values of θ than at higher values. As Figure 4 indicates, there was a general trend of increasing E_r values as γ_d increased. The convergent regression lines in Figure 4 reveal that, at large values of θ, lower density specimens may exhibit stiffer load response than higher density specimens.

The VCP test data showed very slight differences in ν_r values for various density levels. High density specimens had lower values of ν_r than did the lower density specimens, although there were exceptions. For the gravel and blend specimens, the low density specimens showed lower ν_r values except at the upper extreme of σ_1/σ_3 values. No trends were evident from the CCP data, except that ν_r, obtained from the CCP test, was always greater than that obtained from the VCP test data. Again, this would seem to indicate that greater volume changes are caused by the CCP test conditions.

Effects of Type of Material

Figure 5 shows the effects of type of material on the resilient modulus. The intersecting regression lines indicate that the differences in the moduli for different materials were functions of stress. For all specimens the crushed stone generally yielded greater values for the resilient modulus than did the gravel throughout the entire range of θ values.

The VCP test results indicate almost identical values of ν_r for all 3 materials at the lowest density level. There is not much difference between the regression lines for the other density level specimens, but gravel displayed consistently higher values of Poisson's ratio than did crushed stone or blend material. Again, the relatively flat nature of the regression curves from 2 to 7 was noted.

The CCP test data show considerably more variation in ν_r values for different material types, but no firm conclusions can be reached. Crushed stone displayed the lowest values of ν_r for the high and low density specimens, but gravel yielded the highest values for the high density specimens, the intermediate values of ν_r for the low density specimens, and the lowest Poisson's ratio for the intermediate density specimens. Here, too, the CCP test results yielded consistently higher values of Poisson's ratio than did the VCP results.

Plastic Deformations

Although no direct attempts were made to measure the plastic (nonrecoverable) deformations associated with the individual stress pulses, data are available that show total plastic deformations accumulated by each specimen throughout the test series (1). These data indicate that nonrecoverable deformations associated with the CCP test exceeded those associated with the VCP test for every specimen.

Figure 3. CCP test results—$\upsilon_r = f(\sigma_1/\sigma_3)$ model, specimen LD-2.

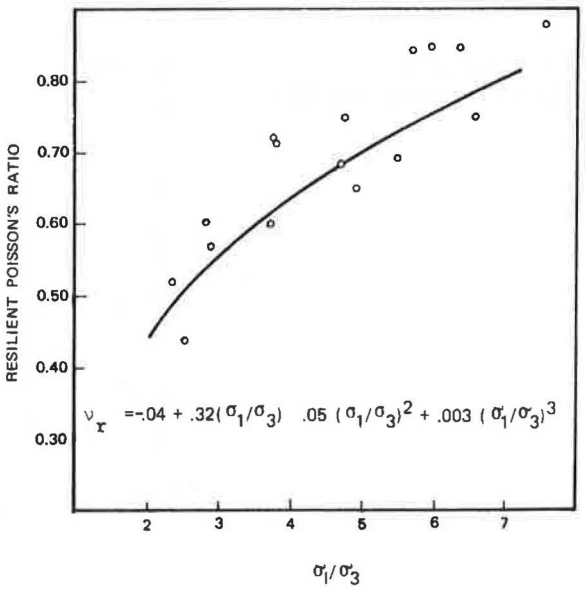

Figure 4. VCP test results—$E_r = f(\theta)$ model, specimens HD-2, MD-2, and LD-2.

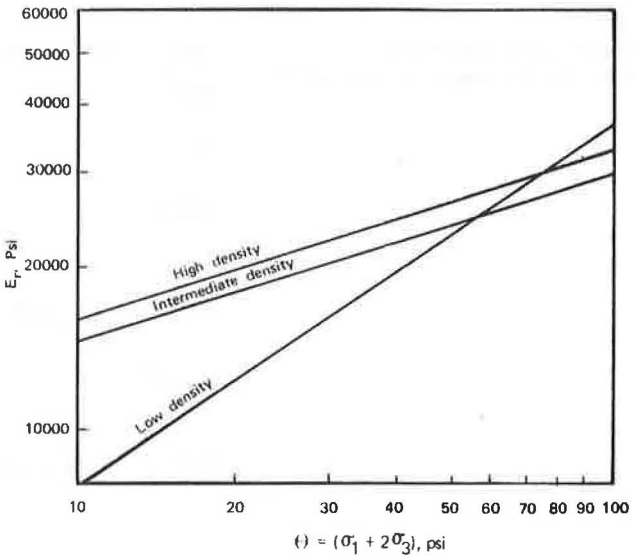

Figure 5. VCP test results—$E_r = f(\theta)$ model, specimens LD-1, LD-2, and LD-3.

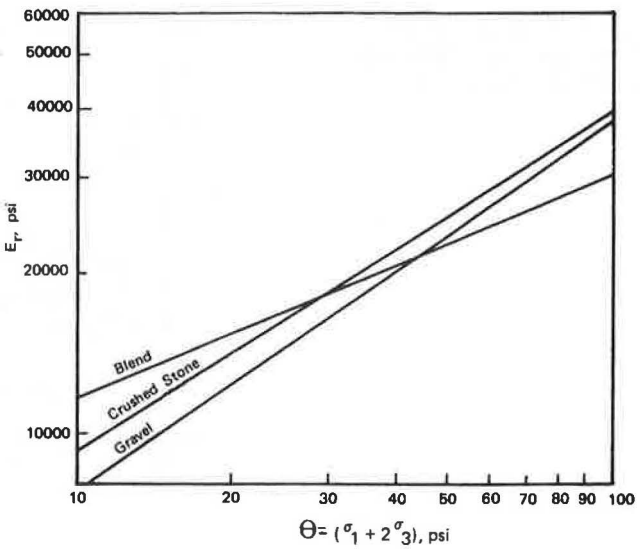

Figure 6. VCP and CCP test results—$E_r = f(\theta)$ model, specimen MD-1.

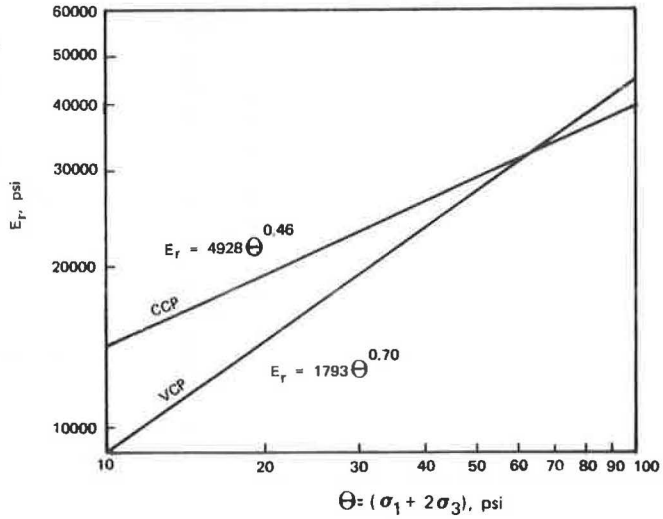

Figure 7. VCP and CCP test results—$E_r = f(\theta)$ model, specimen HD-2.

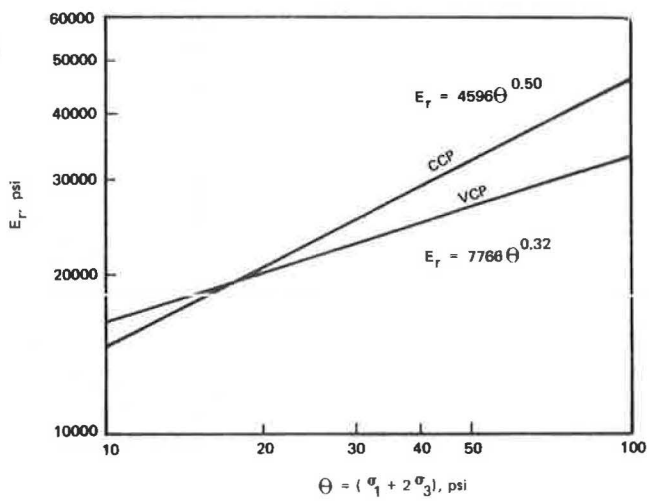

Figure 8. Comparison of VCP and CCP test results—$E_r = f(\theta)$ model, specimens HD-3 and MD-3.

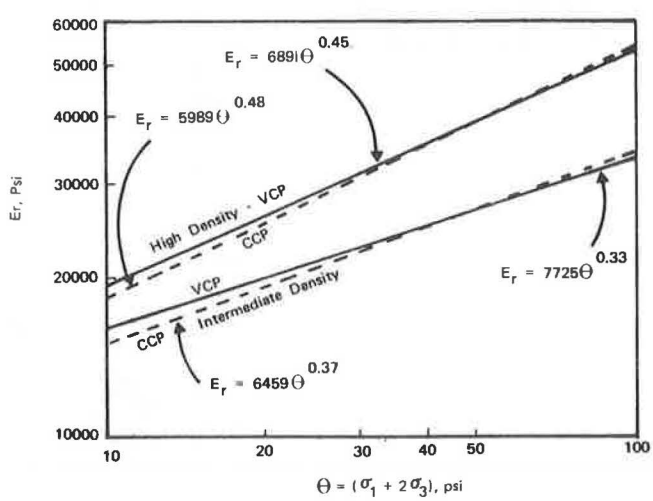

Anisotropic Behavior

Elastic isotropic materials cannot have a Poisson's ratio value in excess of 0.5. However, as was reported earlier, the CCP test results yielded values of ν_r consistently in excess of 0.5. Certainly, a percentage of the large lateral deformations involved are due to the nonuniform stress and strain states within the specimens; but, it can also be assumed that these results indicate anisotropic behavior by granular materials. The same conclusion has been reached by Moore, Britton, and Scrivner (9); Barksdale and Hicks (4); and Dehlen (5).

At principal stress ratios, σ_1/σ_3, in the range from 2 to 7, which is typical of those thought to exist in granular layers of flexible pavement systems, this anisotropic behavior was not observed in the VCP test series, as evidenced by the consistently lower Poisson's ratio values. However, at stress ratios approaching hydrostatic conditions, the measured lateral deformations were so large as to be incompatible with isotropic material properties. This indicates that the stiffness of the material was less in the lateral direction than in the axial direction. Dehlen (5) reported similar cross-isotropic behavior of sands. Despite the evidence of some degree of anisotropic properties of the materials tested, the VCP test data indicate that, in the proper range of stress states, such behavior only minimally influences the results.

Comparison of VCP and CCP Test Results

Test results for the crushed stone and gravel materials indicate that the CCP test yielded slightly higher values of E_r throughout the range of θ values for the intermediate and low density specimens than did the VCP test. This was also true for the low density blend specimen for values of θ greater than 15 psi (103 kPa). The difference in E_r values in each case was maximum for values of θ near 10 psi (69 kPa), the lower extreme for θ. At this point, the CCP test on the intermediate density crushed stone specimen showed E_r to be approximately 50 percent greater than the VCP test data indicated. This difference diminished as θ increased because the regression lines converged at higher θ values. However, the differences in E_r for the other specimens were considerably smaller, 30 percent at maximum. Figures 6 and 7 show the variation in E_r for the CCP and VCP test data derived from specimens MD-1 and HD-2.

Similar results were obtained from the high density crushed stone and gravel specimens. For gravel, the CCP and VCP test regression lines intersected at a θ value near 17 psi (117 kPa); so for most of the range of interest the CCP test results yielded higher values of E_r. But for the crushed stone specimen, the point of intersection was at a θ value of 35 psi (241 kPa).

For 2 specimens, the high and intermediate density blend specimens, the VCP and CCP test data resulted in almost identical regression lines for E_r, as shown in Figure 8.

It would appear that, in general, the CCP test data overestimated the resilient modulus as compared to the VCP test data. However, 2 observations should be made. First, this phenomenon was not observed for all specimens. Second, in the cases where it did occur, the magnitude of the difference in E_r was not constant because of the intersecting or convergent nature of the regression lines; therefore, the magnitude of the difference depends on the value of θ for which the values of E_r are calculated. The differences in the results of the 2 types of test may or may not be significant for pavement response to load because the modulus throughout the granular layers was determined from existing stress. The significance of these differences in predictive equations for E_r is discussed by Allen (1).

The CCP test data for all specimens yielded significantly higher values for the resilient Poisson's ratio than did the VCP data, which indicates correspondingly greater volume change. It can be shown that the volumetric strain of a specimen, $\Delta v/v$, is equal to the first invariant of the strain tensor, $\epsilon_1 + 2\epsilon_3$, for the triaxial test specimen. Detailed test data (not included in this paper) showed that at almost all stress levels applied during the CCP test, the $\Delta v/v$ calculated from the sum of the principal strains would indicate that the specimen increased in volume. However, applying the same procedure to the VCP test results would show little, if any, volume increase. Therefore, the

conditions of the CCP test are such that inordinate degrees of volume change are imposed on the specimen, thereby yielding results that erroneously overestimate Poisson's ratio.

CONCLUSIONS

Conclusions derived from the results of this investigation are as follows:

1. The resilient response of well-graded granular materials was independent of stress pulse duration. Therefore, any pulse duration in the range of those applied to pavement elements by wheel loads moving at speeds of about 15 to 70 mph (24 to 113 km/h) may be used in laboratory investigations.
2. The resilient response of a specimen determined after 25 to 100 stress repetitions was representative of the response after several thousand stress repetitions.
3. One specimen may be used to measure the resilient response over the entire range of stress levels. In addition, the stress sequence tests revealed that these stress levels could be applied to the specimen in any order without error.
4. The testing variable that affected the resilient response of the granular specimens most significantly was the applied state of stress. The stress-dependent nature of the resilient parameters is typified by the form of the predictive equations for E_r and ν_r (Eqs. 1 and 2).
5. Variations in the dry density of the specimen affected the resilient parameters. In general, the resilient modulus increased as density increased. Poisson's ratio showed no consistent variation with changes in density. The values of ν_r were very similar for all specimens at corresponding values of σ_1/σ_3 for the VCP test.
6. The effects of type of material on the resilient parameters were slight when compared to the effects of changes in stress. In general, crushed stone yielded slightly higher values of E_r than did gravel. The modulus of the blend material was normally between those of the other materials. Poisson's ratio varied only minimally from one material to another. The values of ν_r calculated for the gravel normally exceed those for the crushed stone.
7. Indications of anisotropic behavior were observed for both the CCP and VCP tests. Although it was not possible to measure the stiffness in both the lateral and axial directions, it appeared that each specimen was less stiff laterally.
8. As compared to the VCP test, the CCP test greatly overestimated Poisson's ratio. Most likely, some of the large lateral deformations observed were due to nonuniform stress and strain within the specimen. But, because the VCP test yielded values of ν_r in the range of 0.35 and 0.40, conditions of the CCP test could impose greater amounts of volume change on the specimens, as indicated by the computed values of ν_r consistently in excess of 0.50.
9. Values of the resilient modulus computed from CCP test data exceeded E_r values computed from the VCP tests for most stress levels. The magnitude of the difference was itself a function of stress and, thus, nonconstant.
10. Although the CCP test yielded unacceptably high values of Poisson's ratio, the use of a constant value from ν_r for granular paving materials in the range of 0.35 to 0.40 adequately represented this parameter for pavement analysis. This conclusion is based on the relatively flat slope of the regression line for ν_r over a range of σ_1/σ_3 from 2 to 7.

Before conclusions can be drawn regarding the significance of the variations in resilient parameters obtained by different test procedures (CCP or VCP), it is first necessary to examine these differences in the context of their effects on the response of a pavement structure to wheel loadings.

REFERENCES

1. Allen, J.J. The Effects of Non-Constant Lateral Pressures on the Resilient Response of Granular Materials. Univ. of Illinois at Urbana-Champaign, PhD dissertation, May 1973.
2. Barksdale, R.D. Compressive Stress Pulse Times in Flexible Pavements for Use in Dynamic Testing. Highway Research Record 345, 1971, pp. 32-44.

3. Barksdale, R. D. Repeated Load Test Evaluation of Base Course Materials. Georgia Inst. of Tech., Atlanta, Proj. E20-609, Dec. 1971.
4. Barksdale, R. D., and Hicks, R. G. Material Characterization and Layered Theory for Use in Fatigue Analyses. HRB Spec. Rept. 140, 1973, pp. 20-48.
5. Dehlen, G. L. The Effect of Non-Linear Material Response on the Behavior of Pavements Subjected to Traffic Loads. Univ. of California, Berkeley, PhD dissertation, 1969.
6. Dunlap, W. A. A Report on a Mathematical Model Describing the Deformation Characteristics of Granular Materials. Texas Transportation Institute, Texas A&M Univ., College Station, Tech. Rept. 1, Study 2-8-62-67, 1963.
7. Gray, J. E. Characteristics of Graded Base Course Aggregates Determined by Triaxial Tests. Nat. Crushed Stone Assoc., Washington, D.C., Engineering Bull. 12, July 1962.
8. Hicks, R. G. Factors Influencing the Resilient Properties of Granular Materials. Univ. of California, Berkeley, PhD dissertation, 1970.
9. Moore, W. M., Britton, S. C., and Scrivner, R. H. A Laboratory Study of the Relation of Stress to Strain for a Crushed Limestone Base Material. Texas Transportation Institute, Texas A&M Univ., College Station, Res. Rept. 99-5F, Study 2-8-65-99, Sept. 1970.
10. Morgan, J. R. The Response of Granular Materials to Repeated Loadings. Proc. Third Conference of Australian Road Research Board, Sydney, 1966, pp. 1178-1192.
11. Seed, H. B., Mitry, F. G., Monismith, C. L., and Chan, C. K. Prediction of Flexible Pavement Deflections from Laboratory Repeated-Load Tests. NCHRP Rept. 35, 1967.

ESTIMATION OF PERMANENT DEFORMATION IN ASPHALT CONCRETE LAYERS DUE TO REPEATED TRAFFIC LOADING

D. B. McLean, E. W. Brooker and Associates, Edmonton, Alberta, Canada; and
C. L. Monismith, Institute of Transportation and Traffic Engineering, University of California, Berkeley

Methodology to permit estimation of permanent deformation (rutting) in pavement structures from repeated load triaxial compression and creep tests is discussed. Techniques to estimate the distortion characteristics of asphalt concrete and the use of these data together with linear viscoelastic theory to predict rutting in asphalt-bound layers of pavement structures are concentrated on. Although there is little field data to demonstrate the development of rutting with load repetitions under controlled conditions, Hofstra and Klomp have presented such data from test track studies. The use of the repeated load test data together with elastic theory gives the same form of relation of rut depth versus load applications measured by Hofstra and Klomp suggesting that the procedure has potential to examine this facet of design. When used to study the influence of various parameters on pavement response, this approach led to the following: Subgrade stiffness appears to have little influence on the accumulation of rutting in the asphalt-bound layer, at least for the stiffness range examined; asphalt concrete stiffness exerts significant influence on rutting in the asphalt-bound layer; and rut depth in the asphalt layer is independent of layer thickness for the range examined. The procedure in which the creep test was used to estimate rutting provided estimates that were very small. Moreover, the shape of the rut depth versus the application relation determined by using this methodology did not resemble the form reported by Hofstra and Klomp. These observations require that a careful evaluation be made to ascertain the reasons for these apparent discrepancies.

•IT is possible to analyze the pavement structure within a reasonable framework to ascertain effects of load and environmental factors on pavement response. After comparing the results of such analyses with the limiting response characteristics of the pavement materials or a predetermined condition (e.g., limiting rut depth or surface friction coefficient), pavement performance can be judged. Then, appropriate action can be taken to minimize specific distress modes.

This paper is concerned with the distortion mode of distress and the permanent deformation (rutting) that results from repeated traffic loading. Renewed interest has developed in this phase of the design process as evidenced by the recent work of Heukelom and Klomp (1); Barksdale (2); Romain (3); Elliot (4); Elliot, Moavenzadeh, and Findakly (5); and Hofstra and Klomp (6). Figure 1 shows a subsystem of the pavement design system that permits consideration of the distortion mode. This paper concentrates primarily on structural analysis estimating distortion characteristics, and distortion prediction.

LABORATORY TEST PROGRAM

The measurement of the permanent deformation characteristics of asphalt-bound materials (and other structural pavement materials) requires that the materials be

Publication of this paper sponsored by Committee on Strength and Deformation Characteristics of Pavement Sections.

Figure 1. Distortion subsystem.

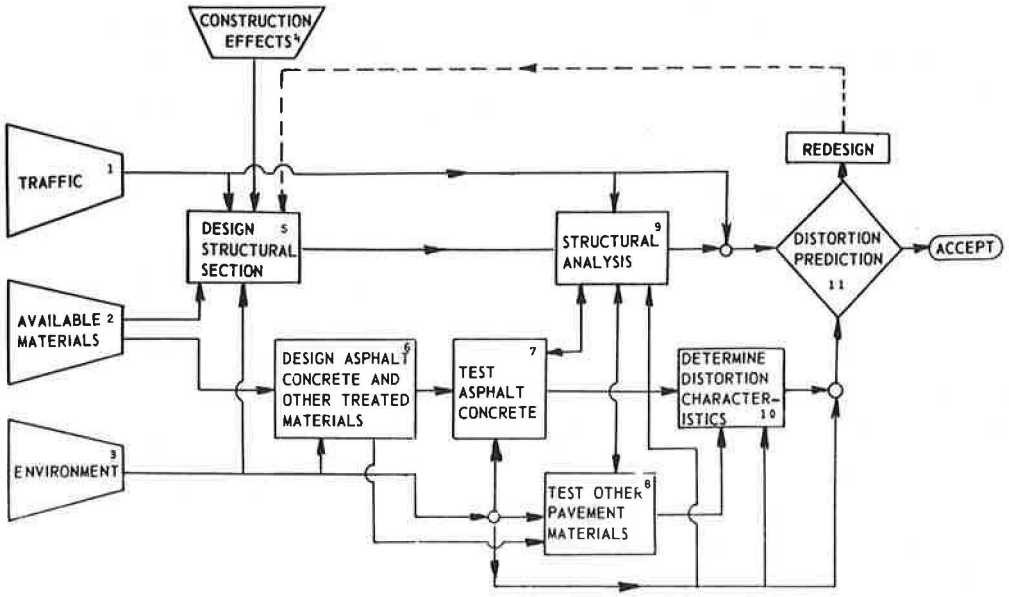

Figure 2. Extension test results, 67 F.

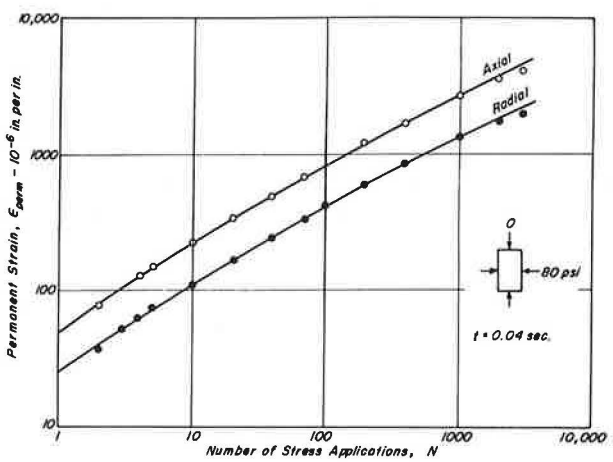

tested under representative service conditions, which include realistic stress states, times of loading, and temperatures.

McLean (7) prepared a detailed analysis of loading and temperature conditions. Test conditions that resulted from this analysis are summarized briefly in the Appendix. Loading times had the same dependency as those suggested by Barksdale (2).

To simulate different loading conditions, the repeated load triaxial-compression equipment developed by Dehlen (8) was used. Use of this equipment permited independent application of axial and radial stresses in repeated loading. The Appendix contains a brief description of the equipment and procedures used to test asphalt concrete specimens in repeated loading.

Creep testing also was performed on asphalt concrete to be used in the predictive procedure, VESYS II, developed by the Federal Highway Administration (FHWA) to estimate the accumulation of permanent deformation (9). This test procedure also is described in the Appendix.

Test Results

Results of repeated load tests over a range in temperatures are shown in Figures 2, 3, and 4. Each figure shows a different type of test and associated terminology. The following are stress states and their locations for thick, asphalt-bound layers:

1. Extension—near the surface,
2. Compression—center of layer, and
3. Tension—near the lower boundary.

Interestingly, the slopes of the strain versus number of stress application curves were essentially the same regardless of the type of test used to induce the permanent deformation.

The strain data shown in Figures 2, 3, and 4 were corrected for volume strains according to the following relation:

$$\epsilon^{p}_{corr} = \epsilon^{p}_{measured} - \tfrac{1}{3}\,[\Delta V/V] \qquad (1)$$

where $\Delta V/V$ = volume strain.

Axial creep compliance from extension tests over a range of temperatures is shown in Figure 5. Rather than use strain as in Figures 2, 3, and 4, a creep compliance was determined from the following:

$$\Psi_E(t) = \frac{\epsilon_A(t)}{\sigma_A - \sigma_R} \qquad (2)$$

where

$\Psi_E(t)$ = axial creep compliance,
$\epsilon_A(t)$ = axial strain,
σ_A = applied axial stress, and
σ_R = radial stress.

Compression tests also were conducted; results were of the same form as shown in Figure 5.

Analyses

The technique used to estimate rutting fitted to data similar to the data shown in Figures 2, 3, and 4 the following third order polynomial by using a least squares procedure:

$$\log \epsilon^{p} = C_0 + C_1 \log N - C_2 (\log N)^2 + C_3 (\log N)^3 \qquad (3)$$

Figure 3. Compression test results, 85 F.

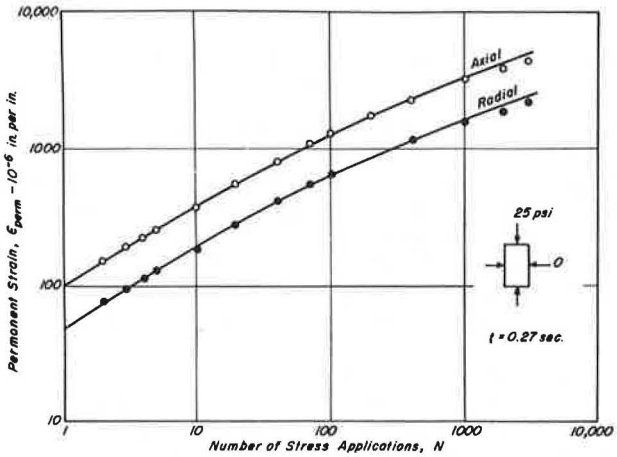

Figure 4. Tension test results, 100 F.

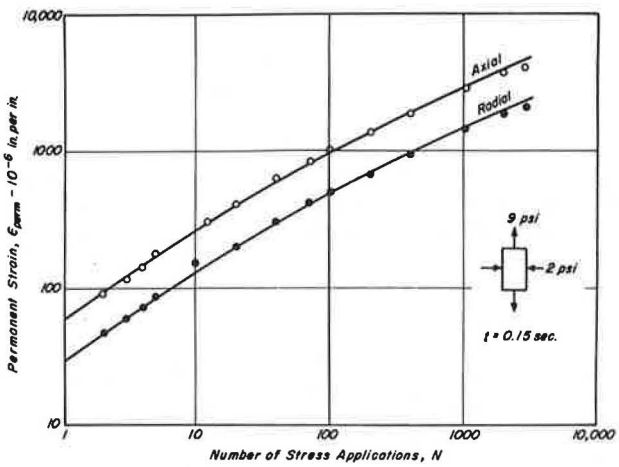

Figure 5. Axial creep compliance from extension tests.

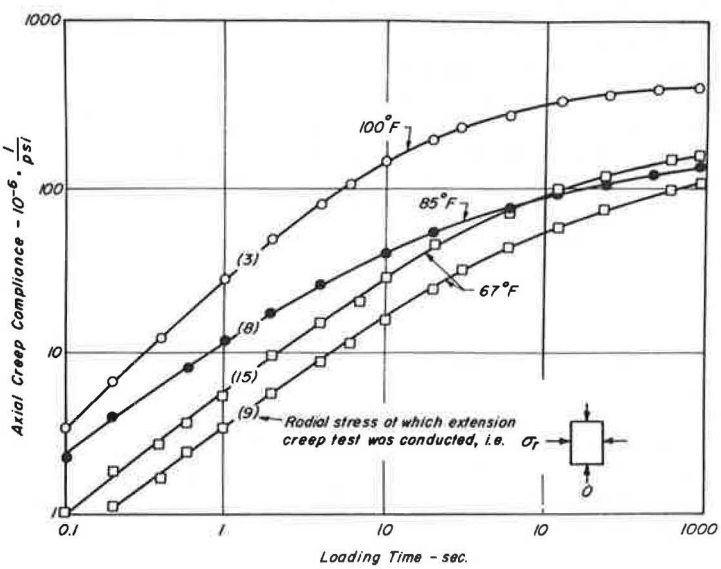

where

ϵ^p = plastic strain (corrected for volume change) and
N = number of stress applications.

The influences of stress state, time of loading, and temperature are reflected in the coefficients C_0, C_1, C_2, and C_3.

In developing the least squares relationships it was found that the polynomials were very sensitive to the first and last data points. To reduce the sensitivity, the first data point (N = 1) was eliminated because seating errors tended to influence the initial readings. Because the majority of tests were stopped at less than 10,000 repetitions, the data were linearly extrapolated to $N = 10^5$ to control the fit at large numbers of repetitions; this must be considered a suitable technique until additional data become available.

For this mix, analyses of the data do not indicate any apparent trends with temperature, stress level, stress direction, or elastic strain for the coefficients C_1, C_2, and C_3. Unfortunately, however, no analyses were performed to define the independence of the coefficients or their interdependence. The results of the analyses are as follows:

Coefficient	Mean	Standard Deviation
C_1	0.85	0.14
C_2	0.013	0.006
C_3	-0.14	0.06

The coefficient C_0 (in this case, the logarithm of permanent deformation resulting from initial load application) appeared to depend on a number of factors including stress, strain, and temperature. To combine the influence of stress and strain on C_0 at a particular temperature the following relationship was developed:

$$\epsilon_1^p = K(\sigma_d \cdot \epsilon_e)^n \qquad (4)$$

where

$\epsilon_1^p = 10^{C_0}$, permanent strain at first load repetition;
$\sigma_d = \sigma_A - \sigma_R$, stress difference in triaxial compression;
ϵ_e = elastic strain; and
K, n = experimentally determined coefficients.

Figure 6 shows data and regression lines that conform to Eq. 4 for axial and radial deformations including both extension and compression results. This form permits making an estimate of permanent deformation in pavement structure that results from an applied load at the surface.

Data from the repeated load tests can be examined in other ways. To illustrate the variations in total, elastic, and permanent strain, data for the specimen whose permanent strain characteristics are shown in Figure 4 are plotted in Figure 7. The permanent strain per load application relationship shown in this figure was obtained by differentiating the curve of the form of Eq. 3, which had been fitted to the data of Figure 4. In Figure 7, after about 100 stress repetitions, the permanent strain per cycle was small.

ANALYSIS OF PAVEMENT STRUCTURES

To estimate permanent deformation from repetitive traffic loading, Heukelom and Klomp (1), Barksdale (2), and Romain (3) suggested the elastic layer theory to compute stresses and strains. They also suggested using these values to estimate permanent deformations from appropriate constitutive relationships. Viscoelastic layer theory, together with creep data incorporated in an analysis such as that developed by Elliott et al. (4) and included in the FHWA program VESYS II, can be used also to estimate permanent deformation.

Figure 6. Repeated load triaxial compression test results.

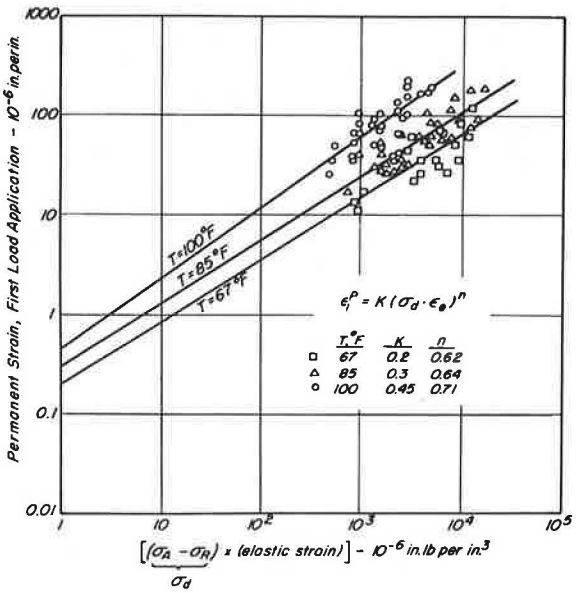

Figure 7. Variations in total, elastic, and permanent strain, tension test, 100 F.

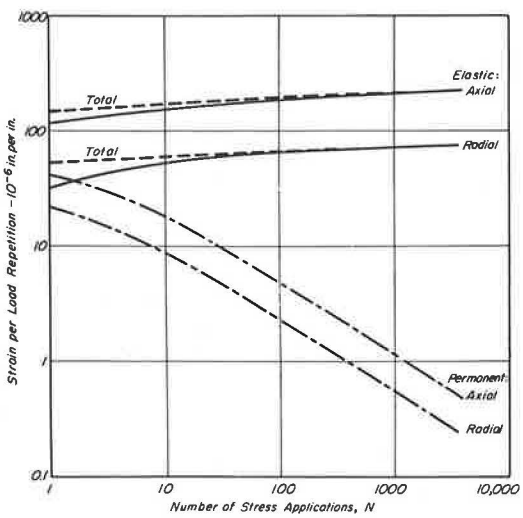

Figure 8. Schematic of pavement system used to estimate permanent deformation.

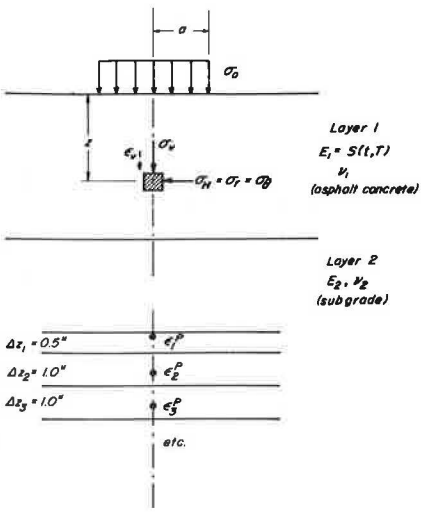

Elastic Analysis

In this procedure the elastic layer program CHEV 5L and the relationships represented by Eqs. 3 and 4 were used. For simplicity, the computations were done for a 2-layer system (asphalt concrete directly on subgrade) and for a load applied to a single circular area. The procedure suggested by Barksdale (2), where the layer under consideration is subdivided into a series of layers, was followed. Computations were performed at 1-in. (2.5-cm) intervals throughout the depth of the upper layer and at the boundaries—all on the axis of the loaded area. Also, the upper layer was assumed to have a constant stiffness modulus.

To permit the use of Eqs. 3 and 4 it was first necessary to compute σ_d and ϵ_e of Eq. 4. These were determined, as shown in Figure 8, with the aid of the computer program by assuming

$$\sigma_d = \sigma_v - \sigma_H \tag{5}$$

and

$$\epsilon_e = \epsilon_v \tag{6}$$

where

σ_v = vertical stress,
σ_H = horizontal stress (radial and tangential stresses are equal for the condition analyzed), and
ϵ_v = vertical strain.

These values were then used for a number of load repetitions to compute permanent strains, which, in turn, permitted permanent deformation in the layer to be obtained from the relation

$$\delta^p = \sum_{i=1}^{n} (\epsilon_i^p \Delta z_i) \tag{7}$$

where

δ^p = rut depth or permanent deformation in the upper (asphalt-bound) layer and
ϵ_i^p = permanent strain in subdivided layer (Fig. 8).

A series of pavement systems were studied by this procedure to ascertain the influence of various factors on the accumulation of permanent deformation.

To ensure that the procedure under investigation was reasonable, rut depth versus number of load repetitions obtained under controlled conditions by Hofstra and Klomp (6) was included for comparison. Their data were obtained by subjecting an 8-in. (20-cm) layer of asphalt concrete resting directly on a subgrade to a 1,500-lb (6 700-N) wheel load with a contact pressure of 70 psi (485 kPa) in a laboratory test track. About 200,000 load repetitions were applied at a temperature of 86 F (30 C).

Computations were made by using the procedure described above with the same asphalt concrete stiffness as that reported by Hofstra and Klomp, 155,000 psi (1 070 MPa), and the same subgrade modulus, 28,000 psi (193 MPa). The mix tested by Hofstra and Klomp contained a 40-50 penetration asphalt cement and was considered an overasphalted mix because it had less than 2 percent air voids. The mix whose data were reported in the previous section contained an 85-100 penetration asphalt cement and had a void content in the range of 4 to 6 percent. At the 86 F (30 C) temperature and time of loading reported by Hofstra and Klomp, this mix exhibited a stiffness of 2.5×10^5 psi (17 200 MPa). In a comparison of the results, the form of the load-deformation relationship is more important than the absolute magnitude of the deformations.

Table 1 contains the parameters used in the computations for 5 cases. Results of these computations are shown in Figure 9 for comparison with the Hofstra and Klomp

Table 1. Data used for sensitivity studies of permanent deformation estimation.

Condition	Coefficients of Equation 4		Coefficients of Equation 3		
	K	n	C_1	C_2	C_3
1. Mean	0.37	0.66	0.85	-0.14	0.013
2. K_{mean} + 10 percent	0.41	0.66	0.85	-0.14	0.013
3. K_{mean} + 10 percent	0.37	0.72	0.85	-0.14	0.013
4. Max. of range	0.37	0.66	1.23	-0.33	0.032
5. Min. of range	0.37	0.66	0.62	-0.035	0.0027

Figure 9. Rut depths, computed data versus Hofstra and Klomp data.

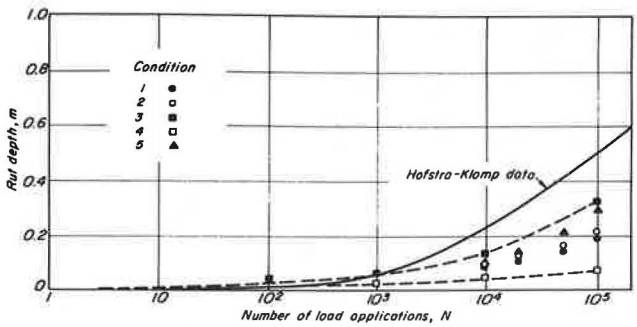

Figure 10. Stress and strain distributions.

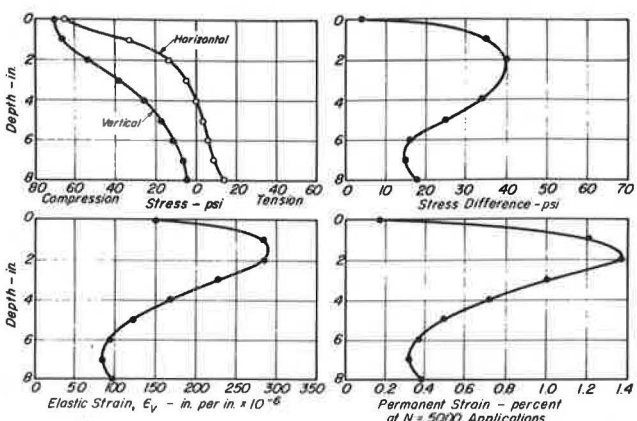

Note: 8-in. (20-cm) layer of asphalt concrete pavement subjected to 1,500-lb (6 700-N) wheel load with a contact pressure of 70 psi (485 kPa)

Figure 11. Stiffness versus temperature.

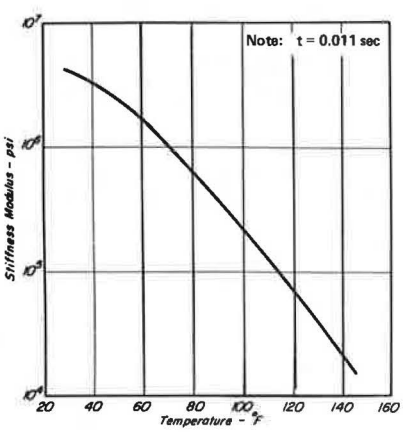

data. Although the mixtures were different, the shapes of the curves were similar, indicating the potential of this procedure.

Figure 10 shows the distribution of elastic stresses and strains and permanent strains with depth for the mean condition given in Table 1 (at N = 5,000 stress applications for permanent strain). In Figure 10 the distribution of permanent strain is similar in shape to the distributions of stress difference and elastic vertical strain. Hofstra and Klomp observed that the distribution of permanent strain was fairly uniformly distributed in the layers of each section of the laboratory test track pavements. A number of factors might contribute to this difference. For example, time of loading was assumed constant with depth (constant stiffness modulus). The analyses of Barksdale (2) and McLean (7) indicated an increase in loading time with depth, which, in turn, reduced the stiffness. As will be seen, this could influence the distribution of permanent strain.

To examine the influence of material characteristics, temperature, and pavement thickness, a series of solutions was developed by using this procedure. Two subgrade stiffnesses—5,000 psi (34 500 kPa) and 10,000 psi (69 000 kPa)—were used. The stiffness versus temperature relationship shown in Figure 11 was used for the asphalt concrete layer. [The time of loading of 0.011 sec corresponds to that associated with the vertical stress at intermediate depth in a 12-in. (30.5-cm) layer for a vehicle speed of 60 mph (27 m/s) (7).] The other factors are given in Table 2. Mean values for the coefficients C_1, C_2, and C_3 as given in Table 1 were used. Computations were made for a 4,500-lb (20 000-N) wheel load with a contact pressure of 80 psi (550 kPa).

The influence of the stiffness of the asphalt concrete on rut depth is shown in Figure 12. Reducing the stiffness by a factor of 2 increased the permanent deformation more than proportionally, indicating that the influence of stiffness modulus of the asphalt concrete was substantial and that the procedure recommended for stiffness estimation using the characteristics of the asphalt in the mix (11, 12), considered accurate within a factor of 2, requires careful evaluation for use in this part of the design process.

Figure 13 shows, at least for this set of circumstances [h_1 = 12 in. (30.5 cm)], that the subgrade stiffness had practically no effect on the accumulation of permanent deformation in the asphalt concrete layer. But, subgrade stiffness will influence the total permanent deformation at the pavement surface (a factor not considered in this analysis); and, for a given thickness, h_1, total deformation will increase as the stiffness is reduced.

The influence of layer thickness on permanent deformation within the asphalt-bound layer is shown in Figure 14 to be minimal. This same result was reported by Hofstra and Klomp in their laboratory test track study. This comparison as well as those illustrated earlier indicates that the elastic theory for stress and strain distribution and a constitutive relationship determined from laboratory repeated load tests have the potential to assist in estimating permanent deformation accumulation in thick, asphalt-bound layers.

Viscoelastic Analysis

In this section the VESYS II procedure was used to examine the accumulation of permanent deformation in the same structure discussed in the previous section.

This procedure used a creep compliance determined from laboratory tests. Two conditions were used for compliance determination—compression and extension. Table 3 gives a summary of measured compliance values together with those determined from equations that were fit to the data. The 2 test techniques resulted in different compliance values, which, in turn, influenced rut depth prediction.

Results of the first part of the program are given in Table 4 and form the basis for subsequent calculations. Deflections computed from the data are shown in Figure 15 as a function of time for a 4,500-lb (20 000-N), single-wheel load with a contact pressure of 80 psi (550 kPa). In this system, the thickness of the asphalt layer (h_1) was taken as 12 in. (30.5 cm), and the subgrade modulus was assumed to be 5,000 psi (34 500 kPa).

In the portion of the program estimating the accumulation of permanent deformation, the time of loading (load assumed to vary with time as a Haversine function), t,

Table 2. Factors used in deformation analysis.

Temperature (F)	E_1 psi x 10^6	ν_1[a]	Coefficients of Equation 4[b]	
			K	n
72	1.0	0.21	0.22	0.62
85	0.51	0.28	0.32	0.66
100	0.225	0.36	0.44	0.70
114	0.1	0.43	0.56	0.73
126	0.05	0.50	0.63	0.76

Note: °C = 5/9 (°F - 32). 1 psi = 6.9 kPa.

[a] ν is a function of mixture stiffness or temperature or both.
[b] Dependent on temperature (see Fig. 6).

Figure 12. Influence of stiffness modulus on permanent deformation.

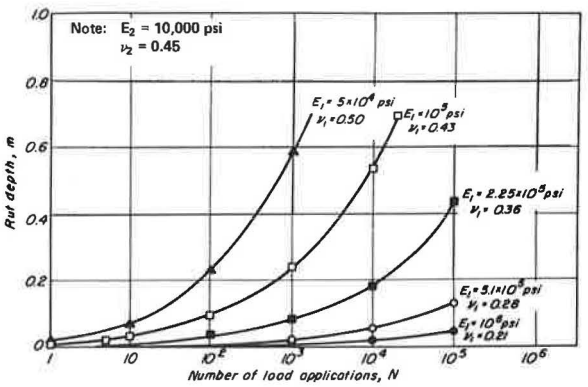

Figure 13. Influence of subgrade stiffness on permanent deformation.

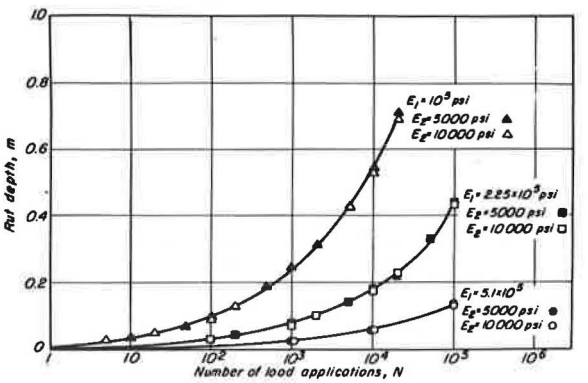

Figure 14. Influence of pavement thickness on permanent deformation.

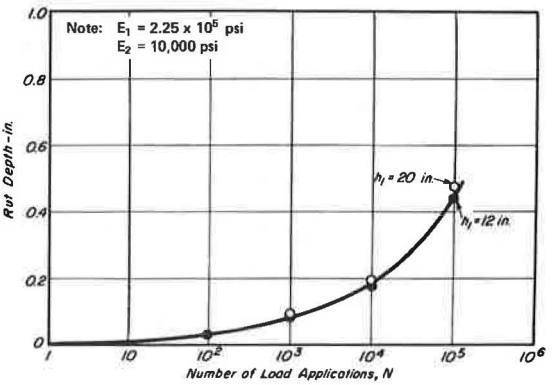

Table 3. Axial creep compliance values, measured and fitted.

Time (sec)	Compression, 85 F		Compression, 100 F		Extension, 85 F		Extension, 100 F	
	Measured[a]	Fitted[a]	Measured[a]	Fitted[a]	Measured[a]	Fitted[a]	Measured[a]	Fitted[a]
0.1	4.1	7.1	13.5	16.6	4.1	5.2	13.5	17.1
0.5		11.0		22.9		9.4		28.6
1.0	15.5	15.1	32.0	29.1	13.0	13.7	43.5	40.9
5.0		29.2		49.8		31.2		99.9
10	34.5	34.0	55.0	55.3	39.0	40.3	141.0	141.0
50		45.3		66.0		70.1		270.0
100	48.8	49.2	69.5	69.3	85.0	84.3	315.0	310.0
500		59.1		77.5		124.0		389.0
1,000	65.0	63.5	82.0	81.1	140.0	136.0	405.0	407.0
5,000		78.3		93.5		183.0		444.0
10,000	86.0	86.5	101.0	101.0	222.0	223.0	470.0	469.0
50,000		109.0		123.0		341.0		539.0
100,000		112.0		126.0		358.0		549.0

Note: °C = 5/9 (°F - 32). Multiply compliance values by 0.145 to convert to 1/MPa.

[a]These values are in 10^{-6} in./in./psi.

Table 4. Axial creep compliance data, coefficients for Dirichlet series.

δ_i (1/sec)	$G_i \times 10^{-6}$			
	Compression (85 F)	Compression (100 F)	Extension (85 F)	Extension (100 F)
50	1.9	-14.8	-4.1	-13.8
5.0	-21.0	-33.8	-19.3	-41.4
0.05	-16.5	-15.8	-35.1	-201.0
0.005	-12.4	-10.6	-61.5	-135.0
0.0005	-14.3	-10.1	-14.6	-24.9
0.00005	-41.8	-40.7	-225.0	-134.0
0	112.0	126.0	360.0	550.0

Note: Dirichlet series equation is $J(t) = \sum_{i=1}^{n} G_i \exp \delta_i t$.

°C = 5/9 (°F - 32).

Figure 15. Computed deflection versus time.

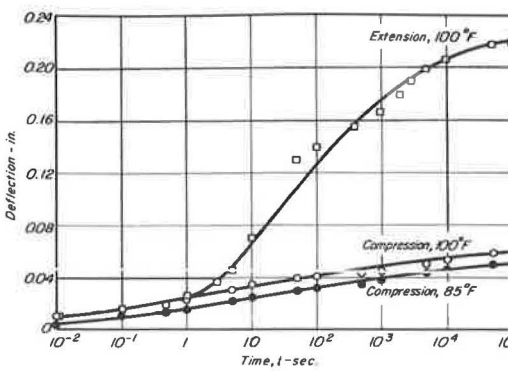

Figure 16. Computed permanent deformation versus number of load applications by using VESYS II; t = 0.25 sec, T = 2.5 sec.

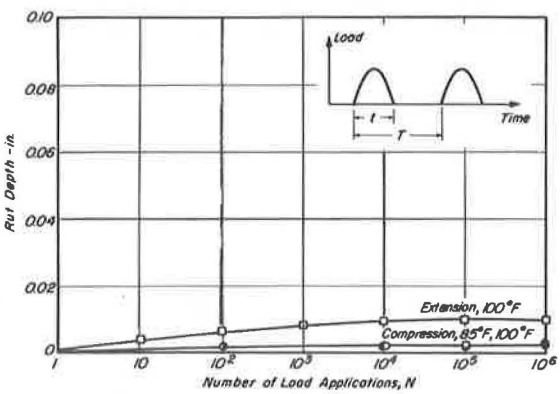

Figure 17. Computed permanent deformation versus number of load applications by using VESYS II; t = 0.50 sec, T = 1.0 sec.

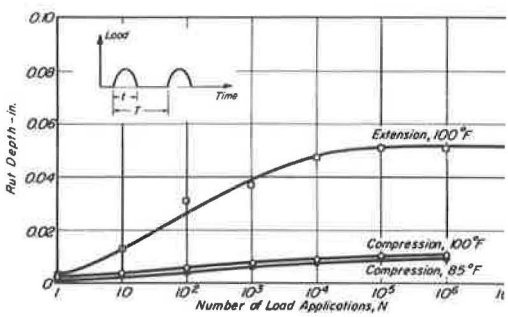

and the total length of time before the next load is applied, T, are variables. Two conditions were used:

1. t = 0.25 sec, T = 2.5 sec (Fig. 16) and
2. t = 0.50 sec, T = 1.0 sec (Fig. 17).

In Figures 16 and 17, the permanent deformations that were estimated were substantially less than those computed earlier for essentially the same conditions. Moreover, the accumulation of permanent deformation with number of load applications by this procedure did not exhibit the same shape as that observed in the studies of Hofstra and Klomp. The reasons for these differences are not clear.

SUMMARY

Two procedures to predict permanent deformation in asphalt-bound layers by using laboratory-determined materials response were presented. One used repeated load triaxial compression tests and elastic theory; the other used a static creep test and viscoelastic theory.

Hofstra and Klomp presented data on rutting versus load repetitions under controlled conditions from studies on a laboratory test track. The repeated load test data and elastic theory provided the same form of relationship of rut depth versus load applications that was measured by Hofstra and Klomp. This suggests that the procedure can be used to examine this facet of the design problem. This approach, when used to study the influence of a number of parameters on pavement response, resulted in the following observations:

1. Subgrade stiffness appeared to have little influence on the accumulation of permanent deformation in the asphalt-bound layer—at least for the range in stiffnesses examined here;
2. Asphalt concrete stiffness exerted a significant influence on rutting in the asphalt-bound layer; and
3. Like the measurements of Hofstra and Klomp, the calculation procedure indicated that rut depth in the asphalt layer was independent of layer thickness for the range examined.

The creep test procedure estimated very little rutting. Moreover, the shape of the rut depth versus the application relationship determined by this methodology did not resemble the form reported by Hofstra and Klomp. These observations indicate that a careful evaluation must be made of this procedure to ascertain the reasons for these discrepancies.

In the judgment of the authors, neither of the methods is suitable for present design inplementation.

ACKNOWLEDGMENTS

The authors wish to acknowledge the support provided by the staff and facilities of the Institute of Transportation and Traffic Engineering, University of California, Berkeley. The investigation was supported in part by the Transportation Laboratory of the California Department of Transportation and the Federal Highway Administration. Neither agency has reviewed the findings.

REFERENCES

1. Heukelom, W., and Klomp, A. J. G. Consideration of Calculated Strains at Various Depths in Connection With the Stability of Asphalt Pavements. Proc. Second Internat. Conf. on Structural Design of Asphalt Pavements, Univ. of Michigan, Ann Arbor, 1967.
2. Barksdale, R. D. Laboratory Evaluation of Rutting in Base Course Materials. Proc. Third Internat. Conf. on Structural Design of Asphalt Pavements, Univ. of Michigan, Ann Arbor, 1972.
3. Romain, J. E. Rut Depth Prediction in Asphalt Pavements. Proc. Third Internat. Conf. on Structural Design of Asphalt Pavements, Univ. of Michigan, Ann Arbor, 1972.

4. Elliott, J. F., and Moavenzadeh, F. Moving Load on Viscoelastic Layered System, Phase II. Dept. of Civil Engineering, Massachusetts Institute of Technology, Cambridge, Mass., Rept. R69-64, Sept. 1969.
5. Elliott, J. F., Moavenzadeh, F., and Findakly, H. Moving Load on Viscoelastic Layered Systems, Phase II—Addendum. Dept. of Civil Engineering, Massachusetts Institute of Technology, Cambridge, Mass., Res. Rept. R70-20, April 1970.
6. Hofstra, A., and Klomp, A. J. G. Permanent Deformation of Flexible Pavements Under Simulated Road Traffic Conditions. Proc. Third Internat. Conf. on Structural Design of Asphalt Pavements, Univ. of Michigan, Ann Arbor, 1972.
7. McLean, D. B. Permanent Deformation Characteristics of Asphalt Concrete. Univ. of California, Berkeley, PhD dissertation, 1974.
8. Dehlen, G. L. The Effect of Non-Linear Material Response on the Behavior of Pavements Subjected to Traffic Loads. Univ. of California, Berkeley, PhD dissertation, 1969.
9. Kenis, W. J., and McMahon, T. F. Advance Notice of FHWA Pavement Design System and a Design Check Procedure. Presented at AASHO Design Committee Meeting, Oct. 1972.
10. Mendelson, A. Plasticity: Theory and Practice. Macmillan Publishing Co., Riverside, N. J., 1968.
11. Van der Poel, C. A General System Describing the Viscoelastic Properties of Bitumens and Its Relation to Routine Test Data. Jour. Appl. Chem., Vol. 4, Part 5, May 1954, pp. 221-236.
12. Heukelom, W., and Klomp, A. J. G. Road Design and Dynamic Loadings. Proc. Assoc. of Asphalt Paving Technologists, Minneapolis, Vol. 33, 1964, pp. 92-125.

APPENDIX

TRIAXIAL COMPRESSION TEST PROGRAM

Loading Conditions

In this investigation the pavement was represented as a multilayer elastic system in which the material properties were varied to reflect their nonlinear response characteristics. The magnitudes of applied stresses that resulted from loads applied to dual tires lie within the shaded areas shown in Figure 18. Examination of varying stress at varying distances from a point provided an indication of the shape of the stress-time curve to be used. Recommended shapes are given in Table 5. Also included in this table are suggestions for the stress conditions to be utilized. Time of loading, t, data that are shown in Figure 19 and referenced in Table 5 indicate that the horizontal stress was usually longer than the vertical. This might exert a substantial influence on the deformation characteristics of asphalt concrete.

Equipment

The triaxial compression test system used in this phase of the investigation was developed by Dehlen (8). In this system the axial and radial stresses can be independently applied. This independence, as shown in Figure 21, was obtained by loading the specimen axially from the bottom with a loading area equal to that of the specimen; a Bellofram was used to seal the axial loading piston. Axial compression or tension was applied by a double-acting 4-in.- (10.2-cm-) diameter Bellofram piston. Radial pressure was obtained by filling the chamber with silicone oil and by applying air pressure to it through a Bellofram piston interface.

A pneumatic timer control unit was developed for the system consisting of 4 pneumatic timer elements. Figure 22 shows how it functioned. Two elements were activated at the start of the cycle and provided signals of duration t_1 and t_2. Signal t_1 was the "on-time" signal to either the axial or radial loading system. Signal t_2 introduced a delay before the third element was activated. This element provided an "on" signal of

Figure 18. Probable ranges of stress combinations in layer combinations in layer 1 (asphalt layer) of a 2-layer system.

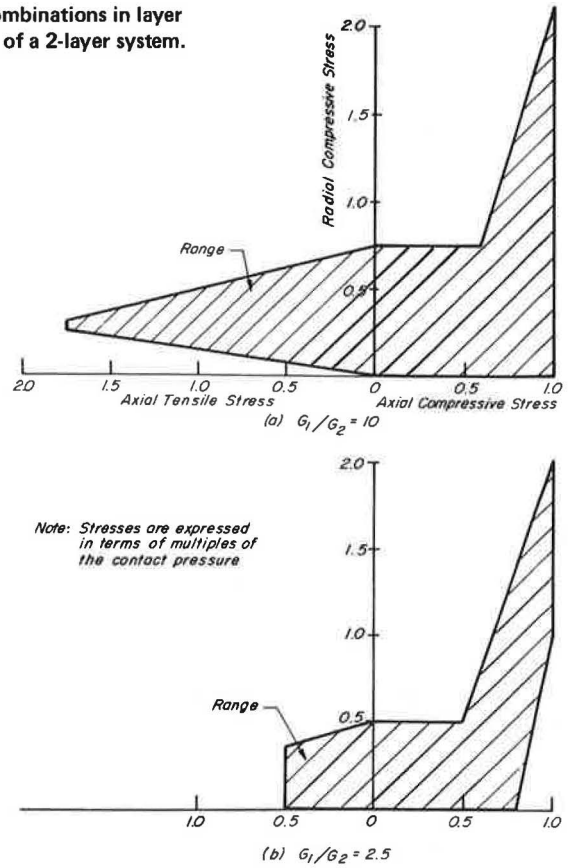

Table 5. Summary of stress-time conditions.

Location and Stress Direction	Shape of Stress-Time Curve	Horizontal-Vertical t Ratio	Horizontal-Vertical Stress Ratio
Near surface			
Vertical	Square	See Figure 19	Less than $1 < \frac{\sigma_v}{\sigma_h} < 5.0$
Horizontal	Triangle	See Figure 19	Less than $1 < \frac{\sigma_v}{\sigma_h} < 5.0$
Intermediate depth			
Vertical	Triangle	See Figure 19	Horizontal stresses may be zero, tensile, or compressive
Horizontal	Triangle	See Figure 19	Horizontal stresses may be zero, tensile, or compressive
Bottom			
Vertical	Triangle	1.0	See Figure 20
Horizontal	Triangle	1.0	See Figure 20

Figure 19. Horizontal-vertical t ratio, range in modular ratios.

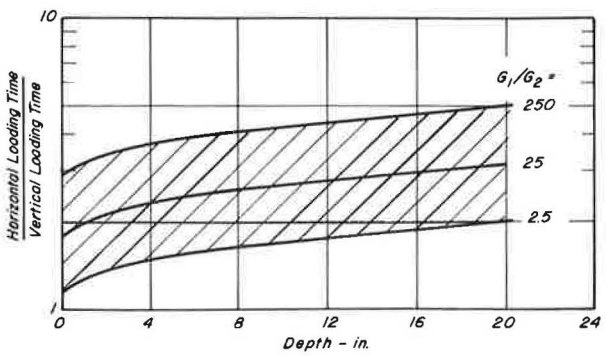

Figure 20. Horizontal-vertical stress ratio at the base of layer 1 versus modular ratio of the 2 layers.

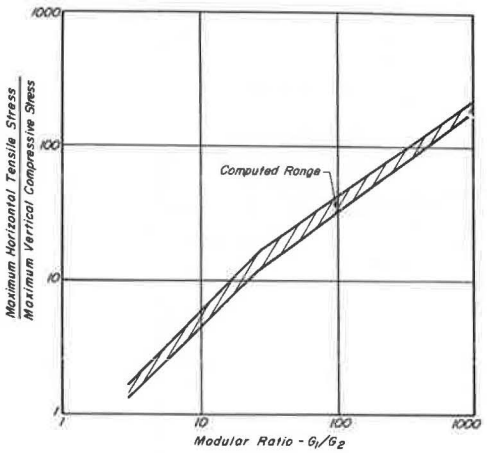

Figure 21. Triaxial apparatus that permits independent variation of axial and radial stresses.

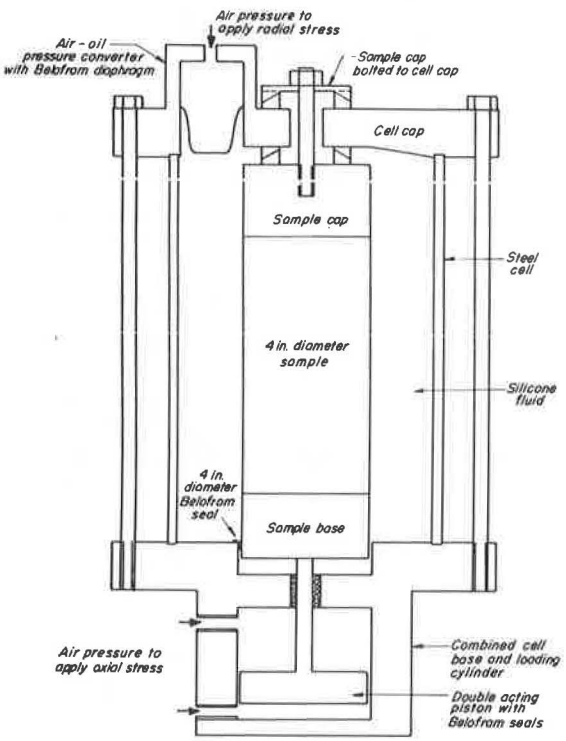

Figure 22. Timer signal outputs.

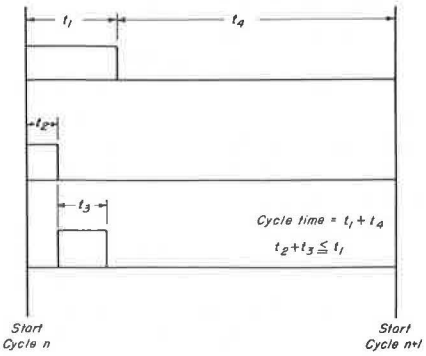

Figure 23. Triaxial loading system for repetitive loading tests.

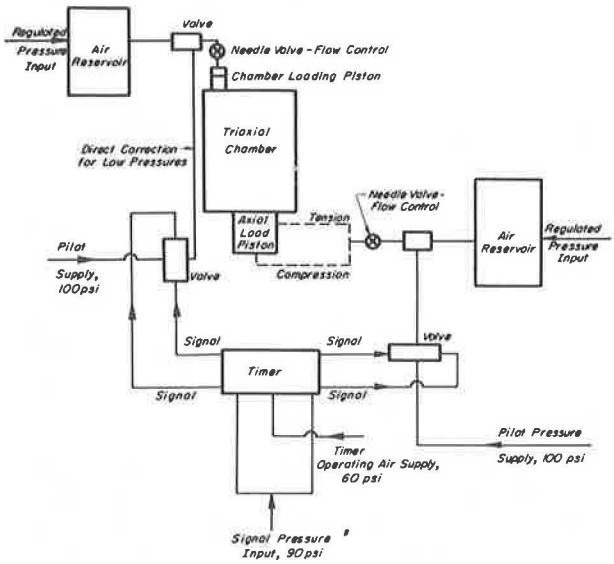

Figure 24. Triaxial loading system for creep tests.

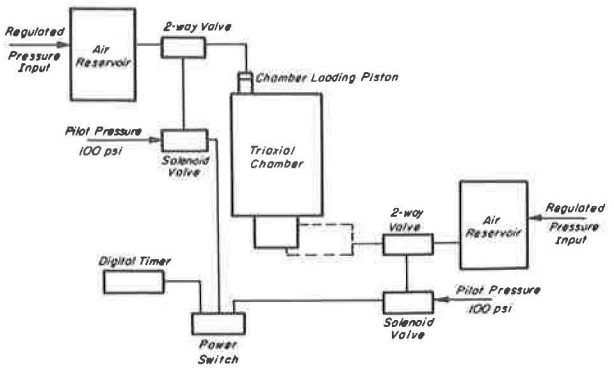

duration t_3 to the second loading element. The fourth timer element controlled the off-load of the system. Times t_1 to t_4 were adjustable from zero to 30 sec.

Output signals from the timer involved only a small line flow of air, insufficient to operate large air valves. Therefore, a booster system was required as shown in Figure 23. By using this approach and maintaining short flow distances from air reservoirs to the loading pistons, rise times (time from zero to full load) could be reduced to 0.007 sec. When longer load rise times were required, needle valves were introduced to control the air flow rates. Because of limitations imposed by valve response times, the minimum load duration that could be obtained was 0.035 sec.

This equipment also was used for creep tests. For these tests the timer portion of the repetitive loading system was replaced by a digital clock reading to 0.01 min. The main air valves were operated by using electric solenoid valves. A main switch activated the solenoid valves and timer simultaneously. System components are shown in Figure 24. Use of high air pilot pressures resulted in rapid valve response times with the result that load rise times were less than 0.01 sec in all tests. Loading times of less than 1 min were measured by using the timer portion of the Sanborn recorder system. Times greater than 1 min were established from the digital clock.

Deformations in the specimens were measured by using linear variable differential transformers firmly attached to the specimens.

Procedures

Repeated Loading—The 3 loading conditions studied in the laboratory were chosen because the pneumatic loading equipment could not completely simulate actual conditions. These were

1. Horizontal compression midway between the loaded areas (by extension tests);
2. Horizontal stress near the point of zero (by unconfined compression tests); and
3. Axial tension and radial compression with the same loading time at the base of the layer (by tension tests).

Because of the time-dependent recovery properties of asphalt concrete, the amount of permanent deformation was expected to depend on the time interval between load applications. In preliminary tests deformation recovery approached zero at a cycle time of 6 sec. This value was selected for use in the study.

Creep Loading—Prior conditioning influenced the response of asphalt concrete in creep loading. In this study the procedure that finally was adopted included the application of a larger stress than that to be used in test for a period of 10 min followed by 2 repetitions of the desired stress applied for a period of 15 min. Recovery times of 1 to 1.5 hours were allowed between each load application. Deformations from the second or third application were used to compute compliance relationships. The 2 loading conditions were unconfined axial compression and axial extension.

TENSILE AND ELASTIC CHARACTERISTICS OF BLACK-BASE MATERIALS

Thomas W. Kennedy, Center for Highway Research,
University of Texas at Austin

This paper summarizes the findings of a study conducted to evaluate the tensile strength, modulus of elasticity, and Poisson's ratio of black-base materials and to determine the variations in these properties for use in elastic and stochastic pavement design systems. Field cores of black-base materials from 10 recently completed highway pavement projects in Texas were tested by using the indirect tensile test. Mean values for the tensile and elastic properties were established, and the variation about these mean values was estimated. The average tensile strength, modulus of elasticity, and Poisson's ratio for all 10 projects were 105 psi (723.95 kN/m^2), 58.2×10^3 psi (401.28×10^3 kN/m^2), and 0.27 respectively; however, the mean values for the individual projects varied considerably. Tensile strengths ranged from 84 to 157 psi (579.16 to 1082.48 kN/m^2), moduli ranged from 38.6×10^3 to 91.5×10^3 psi (266.14×10^3 to 630.87×10^3 kN/m^2), and Poisson's ratios ranged from 0.16 to 0.34. Significant variation also occurred in each project, and the magnitude of this project variation differed. The average coefficients of variation for the 10 projects were 23 percent for strength, 33 percent for modulus, and 25 percent for Poisson's ratio. The ranges of project coefficients for strength, modulus, and Poisson's ratio were 14 to 27 percent, 24 to 59 percent, and 38 to 67 percent respectively. Because of the significant project differences, it was concluded that a single variation value could not be established for the state and that characteristic values were project dependent.

•MOST current pavement design procedures are empirical and deterministic; they use exact values of input and present the results as exact values. At a 1970 workshop on the structural design of asphalt pavements (1), 1 of the areas of research considered the most pressing was the application of probabilistic or stochastic concepts to pavement design. The workshop stated the problem as follows:

> So that designers can better evaluate the reliability of a particular design, it is necessary to develop a procedure that will predict variations in the pavement system response due to statistical variations in the input variables, such as load, environment, pavement geometry, and material properties including the effects of construction and testing variables. As part of this research it will be necessary to include a significance study to determine the relative effect on the system response of variations in the different input variables.

Other researchers (2) also have pointed out the need to apply probabilistic or stochastic concepts to the design parameters of design models. Current research at the Center for Highway Research has developed a design procedure for flexible pavements (3, 4, 5, 6). Trial use of this design system by the Texas Highway Department revealed a definite need to consider the random nature of many of the input variables to estimate design reliability, that is, the probability that the pavement system will perform its intended function over its design life and under the conditions encountered (2).

Publication of this paper sponsored by Committee on Strength and Deformation Characteristics of Pavement Sections.

In response to this need, a theory and procedures have been developed based on classic reliability theory that will allow probabilistic design concepts to be applied to flexible pavement design (2). The method makes it possible to design for a desired level of reliability through the consideration of the variabilities and uncertainties associated with pavement design. The probabilistic theory has been applied to the Texas flexible pavement system, which was originally a deterministic model.

The state of the art has advanced to the point where, in addition to considering the stochastic nature of input variables, the theory of elasticity should be applied to design (7). The first step in this direction is determining the elastic and tensile properties of pavement materials in the roadway. If at the same time an estimate is made of the variations in these properties from point to point in the pavement and for different locations in the state, then a flexible pavement design system based on elastic theory and incorporating stochastic considerations can be developed and implemented. The purpose of this paper is to summarize the findings of a study to estimate the magnitude of the tensile and elastic properties and the variation of these properties for black-base materials from actual pavements in Texas.

EXPERIMENTAL PROGRAM

The principal objectives of this investigation were

1. To characterize black-base materials by tensile and elastic properties, specifically by tensile strength, Poisson's ratio, and modulus of elasticity and
2. To estimate the variation in these properties that can be expected for an in-place pavement, but not necessarily to establish the cause of the variation.

To accomplish these objectives, field cores of black-base materials from 10 recently completed highway pavement projects in Texas were tested by using the indirect tensile test. Mean values for the tensile and elastic properties were established, and the variation about these mean values was estimated. The density of the black-base material also was estimated, and the variations about the means were computed.

The total variation for the elastic and tensile characteristics is composed of many parts. There is inherent material variation, and some testing error, which is the variation that would occur when replicate specimens are prepared and tested under closely controlled laboratory conditions. In field construction additional variation probably would be introduced because the construction process is relatively uncontrolled. Additional variation also may be introduced during construction because of inherent material variation as well as variation caused by the environment, changes in the constituents of the mix, changes in contractor or construction technique, and other factors. Both horizontal and vertical pavement variations will occur. For example, there could be differences between the various lifts of black-base and asphalt concrete; these differences would be of interest because the lower portion of a pavement layer is subjected to the highest load-induced tensile stresses.

To estimate the variation introduced by construction, we obtained core samples from a small area in each pavement. The scatter in test results from this "clustered" sample would then provide an estimate of the variation caused by construction, the inherent variation of the material, and testing. The total variation was estimated from the variation in test results for cores taken along each roadway and for cores from different projects. To estimate the properties and variation differences that occur vertically or between layers, each core was sawed to produce specimens from each layer in the core.

Projects Tested and Core Sampling

A summary of the projects tested is given in Table 1. Figure 1 shows the geographical distribution of the Texas Highway Department districts from which the pavement cores were obtained. As given in Table 1, various black-base materials and different aggregates and asphalt were tested.

Originally, it was planned that a small number of cores would be taken from selected paving projects throughout Texas. However, the Texas Highway Department routinely

Table 1. Description of black-base projects.

District and Project	Cores	Specimens	Distance (miles)	Asphalt		Aggregate
				Type	Weight Percent	
2-A	38	76	15.0	AC-20	5.5	Crushed limestone, field sand
8-A	11	16	3.3	AC-20	5.5 to 6.2	Crushed limestone, sand, gravel
13-A	11	14	8.0	AC-20	4.2	Pit-run gravel
13-B	19	28	4.3	AC-20	4.0 to 4.9	Pit-run gravel
13-C	13	16	3.0	AC-20	4.0 to 4.4	Pit-run gravel
15-A	27	49	10.9	AC-10	5.1	Pit-run gravel
17-B	50	100	19.1	AC-10	4	Brazos River gravel
				AC-20	4	Brazos River gravel
18-B	6	12	0.9	AC-20	5.5 to 6.5	Pea gravel, field sand
19-A	22	54	19.3	AC-20	4.8 to 5.6	Gravel, crushed slag, sand
19-B	18	36	15.2	AC-20	4.3 to 6.4	Gravel, crushed slag, sand

Note: 1 mile = 1.6 km.

Figure 1. Texas highway districts from which black-base cores were obtained.

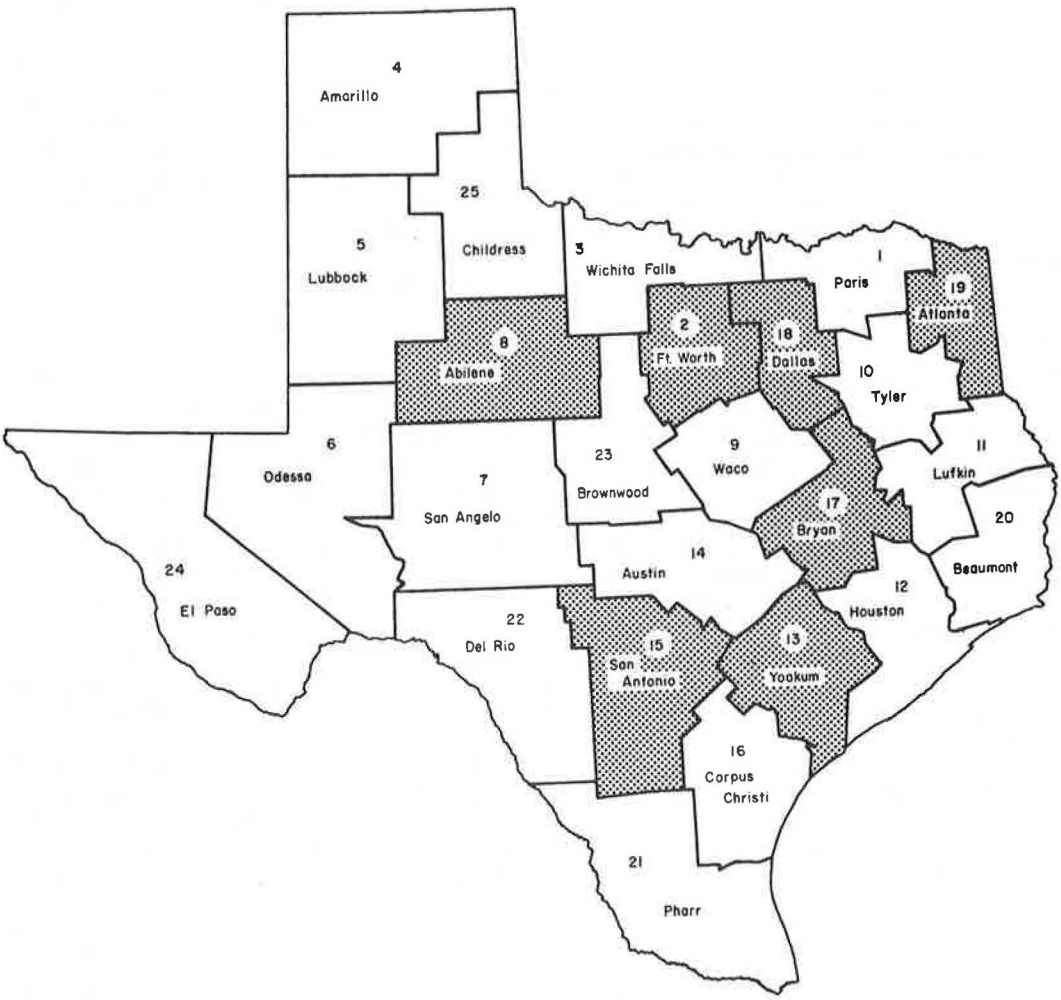

takes a large number of cores from newly completed pavements to determine pavement thickness. Because more information could be obtained by testing these cores than by testing a smaller number of cores taken solely for this study, arrangements were made with the Texas Highway Department to obtain cores from recently constructed pavements that had not been subjected to traffic.

As shown in Figure 2, the Texas Highway Department normally cores black-base pavement layers at regular intervals. But, when a section of pavement is encountered in which the thickness is less than design thickness, cores are taken at smaller regular intervals until the thickness reaches design thickness. Then, cores are taken at the larger intervals. These samples obtained in a systematic fashion can be considered random because the sampling does not coincide with any variation distribution that may exist in the pavement.

One method of estimating the additional variation that results from construction would be to test cores clustered in the pavement. Considering the total length of a project, a group of cores obtained at very small intervals approximates a cluster and is the most economical approach for obtaining cores for most projects. Along-the-road variation (variation during construction that results from changes in pit source, weather, and the like) may be estimated from the cores obtained at large intervals.

Specimen Preparation

Both 4-in. (101.6-mm) and 6-in. (152.4-mm) black-base cores were tested. The cores were sawed at the interface between lifts; thus, each specimen represented 1 lift. Each specimen was approximately 2 in. (50.8 mm) thick. The paving projects were multilane roadways in which the 2 main directional lanes (for example, northbound and southbound) were treated as separate roadways. In addition, the various lifts were considered as separate roadways because they were constructed at different times during construction.

Before testing, we measured and weighed the specimen to estimate density.

Method of Test

The tensile and elastic properties of the paving materials were estimated by using the indirect tensile test procedure originally recommended by Hudson and Kennedy (8) and later modified slightly by Hadley, Hudson, and Kennedy (9). The test involved loading a cylindrical specimen with compressive loads that acted along the vertical diametral plane as shown in Figure 3. To distribute the load and maintain a constant loading area, the compressive load was applied through a ½-in.-(12.7-mm-)wide steel loading strip, which was curved at the strip-specimen interface and had a radius of curvature equal to the radius of the specimen. The loading configuration shown in Figure 3 gave a relatively uniform tensile stress perpendicular to the direction of the applied load that ultimately caused the specimen to fail by splitting or rupturing along the vertical diameter. By measuring the applied load at failure and by continuously monitoring the loads and the horizontal and vertical deformations of the specimen, the tensile strength, Poisson's ratio, and modulus of elasticity of the specimen could be estimated.

The basic test equipment used in this study was the same as that previously used at the University of Texas (9, 10) and included a loading system and a means of monitoring the applied loads, the horizontal deformation of the specimen, and the vertical deformation of the specimen (Fig. 4). In this study, a closed loop electrohydraulic system was used to accurately control the deformation rate of 2 in. (50.8 mm) per min. All tests were conducted at a room temperature of approximately 75 F (23.9 C).

The loading device that was used in this study was a modified, commercially available die set with upper and lower platens constrained to remain parallel during the test. Mounted on the upper and lower platens were ½-in.-(12.7-mm-)wide curved steel loading strips. The load was monitored with a load cell to obtain electrical readouts that could be recorded continuously. A device consisting of 2 cantilevered arms with strain gauges attached measured horizontal deformations. A direct-current, linear variable differential transformer measured vertical deformations and controlled the vertical

Figure 2. Typical core sampling plan.

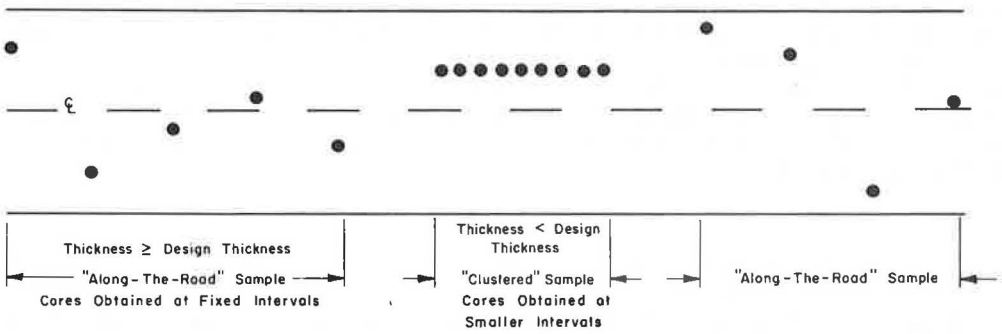

Figure 3. Specimen failing under compressive load.

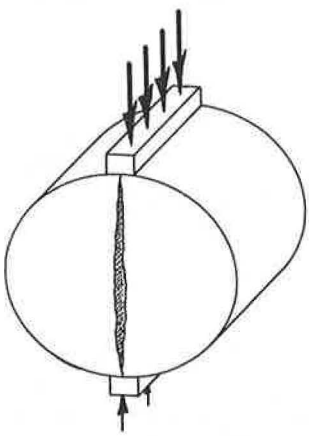

Figure 4. Indirect tensile test equipment.

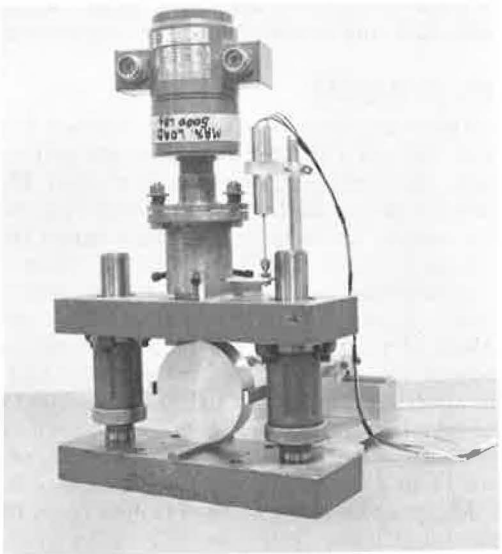

deformation rate during the test by providing an electrical signal related to the movement between the upper and lower platens. The loads and deformations were monitored by 2 X-Y plotters; 1 recorded load and horizontal deformation and 1 recorded load and vertical deformation. Points picked from the X-Y plots were used as input for computer program MODLAS 9, which was developed at the Center for Highway Research to calculate the tensile and elastic properties of materials tested by the indirect tensile test. Included in the printout were estimates of Poisson's ratio, modulus of elasticity, tensile strength, and density for each specimen tested.

ANALYSIS AND EVALUATION

Summaries of the test results for the 10 black-base projects are given in Tables 2, 3, and 4; only 1 of the projects had clustered samples. The parameters estimated by using the indirect tensile test were tensile strength, modulus of elasticity, and Poisson's ratio. Density was estimated by measuring the dimensions and weight of the specimens.

One of the objectives of this study was to obtain an estimate of the variation in material properties existing in a highway pavement; the coefficient of variation, V (the sample standard deviation divided by the sample mean), was used because it related the variation to the mean. For the coefficient of variation to be a valid and meaningful test statistic, it must be assumed that the material property being analyzed is normally distributed about some mean value. Studies have shown that the variability of highway materials and properties follows a normal distribution (2, 7, 11).

Tensile Strength

The mean tensile strengths (Tables 2 and 3) for the various projects ranged from 53 to 157 psi (365.42 to 1082.48 kN/m^2) and averaged 102 psi (703.27 kN/m^2). The lower extreme value was from project 13, which produced very rough cores that were difficult to test and which may have produced low strength values. If project 13 is eliminated, the tensile strengths range from 84 to 157 psi (579.16 to 1082.48 kN/m^2) with an average of 105 psi (723.95 kN/m^2).

In addition to the fact that the various black-base materials were composed of different aggregates and asphalts and had different strengths, as indicated by the coefficient of variation of the means (27 percent with project 13 and 23 percent without project 13), the various projects also had different coefficients of variation. Thus, the coefficients for the individual projects are more meaningful than the overall coefficient of variation. These coefficients ranged from 14 to 40 percent and averaged 26 percent. After eliminating project 13, which exhibited larger variations, the range was 14 to 27 percent with an average of 21 percent.

Many specimens were obtained from the same core by sawing specimens from the individual lifts. Because these lifts were placed at different times, these specimens can be considered to be independent of each other. On the other hand, the properties of the material in the lifts at any given location determine the behavioral characteristics of the pavement at that location. Thus, a comparison was made to determine whether there were strength differences between layers. This comparison indicated that there was no significant difference in the tensile strength of the specimens from the various layers at a confidence level of 95 percent.

Table 4 gives the results of the analysis of the clustered samples for the 1 project that had a significant number of cores for analysis. It can be seen from Table 4 that although the mean tensile strengths essentially were unchanged, the variation for the clustered samples generally was reduced. However, because of the limited number of comparisons, no definite conclusion can be made.

Modulus of Elasticity

Mean modulus values (Tables 2 and 3) varied from 35.0×10^3 to 91.5×10^3 psi (241.32×10^3 to 630.87×10^3 kN/m^2) and averaged 58.8×10^3 psi (405.42×10^3 kN/m^2). The coefficient of variation of the mean modulus values was 36 percent indicating project differences. Eliminating project 13 did not significantly change these values, which varied from

Table 2. Test results for black-base projects.

District and Project	Specimens	Distance (miles)	Tensile Strength Mean (psi)	Tensile Strength V (percent)	Modulus of Elasticity Mean (10^3 psi)	Modulus of Elasticity V (percent)	Poisson's Ratio Mean	Poisson's Ratio V (percent)	Density Mean (pcf)	Density V (percent)
2-A	76	15.0	84	20	38.6	32	0.34	39	127.0	2.4
8-A	16	3.3	112	14	91.5	29	0.28	40	138.4	2.6
13-A	14	8.0	87	40	44.9	46	0.16	58	—[a]	—[a]
13-B	28	4.3	104	36	87.3	62	0.16	73	—[a]	—[a]
13-C	16	3.0	53	40	35.0	40	0.26	57	—[a]	—[a]
15-A	49	10.9	157	17	86.1	59	0.23	47	140.4	2.2
17-B	100	19.1	105	27	55.2	44	0.24	41	136.0	2.3
18-B	12	0.9	107	25	42.2	24	0.20	64	135.1	2.3
19-A	54	19.3	95	20	55.2	33	0.32	38	141.6	1.7
19-B	36	15.2	88	21	64.7	34	0.16	67	136.1	3.6

Note: 1 mile = 1.6 km. 1 psi = 6.9 kN/m^2. 1 pcf = 16 kg/m^3.
[a]Not attainable.

Table 3. Summary of Table 2 test results.

Item	Tensile Strength Mean (psi)	Tensile Strength V (percent)	Modulus of Elasticity Mean (10^3 psi)	Modulus of Elasticity V (percent)	Poisson's Ratio Mean	Poisson's Ratio V (percent)	Density Mean (pcf)	Density V (percent)
Weighted average								
With project 13	102	26	58.8	40	0.25	52	—	—
Without project 13	105	21	58.2	36	0.27	48	—	2.4
Range								
With project 13	104	26	56.5	38	0.18	35	—	—
Without project 13	73	13	52.9	35	0.18	29	—	1.9
V of Means, percent								
With project 13	27	—	36	—	28	—	—	—
Without project 13	23	—	33	—	25	—	—	—

Note: 1 psi = 6.9 kN/m^2. 1 pcf = 16 kg/m^3.

Table 4. Clustered and along-the-road test results for district 15, project 15-A.

Sample	Specimens	Distance	Tensile Strength Mean (psi)	Tensile Strength V (percent)	Modulus of Elasticity Mean (10^3 psi)	Modulus of Elasticity V (percent)	Poisson's Ratio Mean	Poisson's Ratio V (percent)	Density Mean (pcf)	Density V (percent)
Along the road	49	10.9 miles	157	17	86.1	59	0.23	47	140.4	2.2
Cluster 1	7	250 feet	146	11	73.2	42	0.21	44	141.7	1.2
Cluster 2	6	250 feet	151	18	71.6	36	0.31	41	140.2	2.9
Cluster 3	7	250 feet	159	9	75.8	20	0.33	24	142.0	0.8

Note: 1 psi = 6.9 kN/m^2. 1 pcf = 16 kg/m^3. 1 mile = 1.6 km. 1 ft = 0.3 m.

38.6×10^3 to 91.5×10^3 psi (266.14×10^3 to 630.87×10^3 kN/m^2) and averaged 58.2×10^3 psi (401.28×10^3 kN/m^2). Coefficients of variation within projects ranged from 24 to 62 percent and averaged 40 percent. After eliminating project 13, the coefficients ranged from 24 to 59 percent and the average was reduced to 36 percent. A comparison of the moduli of the layers comprising a given core indicated no significant differences existed between layers at a confidence level of 95 percent.

An analysis of the clustered samples (Table 4) indicates that the variation of modulus values for the clustered samples was reduced. But as with tensile strength it is felt that no definite conclusion could be made.

Poisson's Ratio

Mean Poisson's ratio values (Tables 2 and 3) ranged from 0.16 to 0.34 and averaged 0.25 with project 13 and 0.27 without project 13. The coefficient of variation of these means was 25 percent, which was approximately the same magnitude as the coefficient for strength. The variation in Poisson's ratio for each project was large, ranging from 39 to 73 percent with an average of 52 percent. With the elimination of project 13, the range was 39 to 67 percent and the average was reduced to 48 percent. This large range of coefficients probably resulted because the Poisson's ratio is very sensitive to small errors in the deformation measurements. Once again the comparison of values from the layers comprising a core indicated no significant differences between layers; the analysis of clustered samples (Table 4) indicated that the variation was reduced although the mean values for the clusters varied.

Density

A comparison of the mean densities for each project (Tables 2 and 3) has no meaning because different aggregates were used. The coefficients of variation of the densities for each project were generally small; they ranged from 1.7 to 3.6 and averaged 2.4 percent. The magnitudes of these variations were consistent with values reported from previous studies (12), which indicated low coefficients of variation for density.

General Discussion

The following values and ranges are based on the results of this study:

1. Average tensile strength was 105 psi (723.95 kN/m^2) in a range from 84 to 157 psi (579.16 to 1082.48 kN/m^2);
2. Average modulus of elasticity was 58.2×10^3 psi (401.28×10^3 kN/m^2) in a range from 38.6×10^3 to 91.5×10^3 psi (266.14×10^3 to 630.87×10^3 kN/m^2); and
3. Average Poisson's ratio was 0.27 in a range from 0.16 to 0.34.

For design purposes, estimates of variation also must be obtained for each property. The coefficient of variation for various projects ranged from 14 to 27 percent for tensile strength, 24 to 59 percent for modulus of elasticity, and 38 to 67 percent for Poisson's ratio. This large range of values coupled with the different mean values indicates that the amount of variation is project dependent and that a given value cannot be assigned for the state.

The coefficients of variation as given in Table 4 for tensile strength, modulus of elasticity, and Poisson's ratio for the clustered samples were somewhat smaller than for the along-the-road sample, indicating that additional variation was introduced by along-the-road changes. But, because of the limited number of projects, no definite conclusions could be made.

These estimates of variation included a number of components such as testing, inherent, construction, and along-the-road variation. Ideally, estimates of these components should be made to separate the variation for testing and sampling from that for material and construction because testing and sampling variation should not enter into design considerations. Results from previous studies (13) indicated that at least 50 percent or more of overall variation could be assigned to sampling and testing. Thus, for design purposes it might be desirable to reduce the magnitude of the variance.

The reduction probably should be greater for modulus and Poisson's ratio than for strength because additional error is introduced in deformation measurements.

CONCLUSIONS

General

Because the projects were different, and because different types of asphalt and aggregate were used, the coefficients of variation for individual projects were more meaningful than an overall coefficient for all projects. Very little variation in density (generally less than 3 percent) was encountered. Results of the clustered sample analyses indicated that additional variation was introduced along the roadway, but no definite conclusions could be made without additional investigation involving a more carefully designed core sampling plan to obtain clustered samples.

Tensile Strength

Mean tensile strength values varied from 84 to 157 psi (579.16 to 1082.48 kN/m^2) and averaged 105 psi (723.95 kN/m^2). The coefficient of variation of the mean values was 23 percent. No significant differences in tensile strength were found between the various layers or lifts at a confidence level of 95 percent. The within-project coefficients of variation were moderate; they ranged from 14 to 27 percent and averaged 21 percent.

Modulus of Elasticity

Mean modulus values varied from 38.6×10^3 to 91.5×10^3 psi (266.14×10^3 to 630.87×10^3 kN/m^2) and averaged 58.2×10^3 psi (401.28×10^3 kN/m^2). The coefficient of variation of the mean modulus values was 33 percent, which was slightly higher than that for tensile strength.

No significant differences in modulus of elasticity were found between the various layers or lifts at a confidence level of 95 percent. Coefficients of variation for each project ranged from 24 to 59 percent and averaged 36 percent.

Poisson's Ratio

Mean Poisson's ratio values ranged from 0.16 to 0.34 and averaged 0.27. The coefficient of variation of the mean values was 25 percent, which was approximately equal to those obtained for strength and modulus. Coefficients of variation for each project ranged from 38 to 67 percent and averaged 48 percent.

ACKNOWLEDGMENTS

This investigation was conducted at the Center for Highway Research at the University of Texas at Austin. The author wishes to thank the sponsors, the Texas Highway Department, and the Federal Highway Administration. The contents of this report reflect the views of the author, who is responsible for the facts and the accuracy of the data presented herein. The contents do not necessarily reflect the official views or policies of the Federal Highway Administration.

REFERENCES

1. Structural Design of Asphalt Concrete Pavement Systems. HRB Spec. Rept. 126, 1971, 207 pp.
2. Darter, M. I., and Hudson, W. R. Probabilistic Design Concepts Applied to Flexible Pavement System Design. Texas Highway Department, Austin; Texas Transportation Institute, Texas A&M Univ., College Station; and Center for Highway Research, Univ. of Texas at Austin, Prelim. Res. Rept. 123-18, May 1973.
3. Hudson, W. R., McCullough, B. F., Scrivner, F. H., and Brown, J. L. A Systems Approach Applied to Pavement Design and Research. Texas Highway Department, Austin; Texas Transportation Institute, Texas A&M Univ., College Station; and Center for Highway Research, Univ. of Texas at Austin, Res. Rept. 123-1, March 1970.

4. Brown, J. L., Buttler, L. J., and Orellana, H. E. A Recommended Texas Highway Department Pavement Design System User's Manual. Texas Highway Department, Austin; Texas Transportation Institute, Texas A&M Univ., College Station; and Center for Highway Research, Univ. of Texas at Austin, Res. Rept. 123-2, March 1970.
5. Haas, R. C. G. Developing a Pavement Feedback Data System. Texas Highway Department, Austin; Texas Transportation Institute, Texas A&M Univ., College Station; and Center for Highway Research, Univ. of Texas at Austin, Res. Rept. 123-4, Feb. 1971.
6. Strom, O. G., Hudson, W. R., and Brown, J. L. A Pavement Feedback Data System. Texas Highway Department, Austin; Texas Transportation Institute, Texas A&M Univ., College Station; and Center for Highway Research, Univ. of Texas at Austin, Res. Rept. 123-12, May 1972.
7. McCullough, B. F., Brown, J. L., Hudson, W. R., and Scrivner, F. H. Annual Report to Area III Research Advisory Committee on Important Pavement Research Needs, 1970-1971. Texas Highway Department, Austin; Texas Transportation Institute, Texas A&M Univ., College Station; and Center for Highway Research, Univ. of Texas at Austin, Res. Rept. 123-7, April 1971.
8. Hudson, W. R., and Kennedy, T. W. An Indirect Tensile Test for Stabilized Materials. Center for Highway Research, Univ. of Texas at Austin, Res. Rept. 98-1, Jan. 1968.
9. Hadley, W. O., Hudson, W. R., and Kennedy, T. W. Evaluation and Prediction of the Tensile Properties of Asphalt-Treated Materials. Center for Highway Research, Univ. of Texas at Austin, Res. Rept. 98-9, May 1971.
10. Hadley, W. O., Hudson, W. R., and Kennedy, T. W. A Method of Estimating Tensile Properties of Materials Tested in Indirect Tension. Center for Highway Research, Univ. of Texas at Austin, Res. Rept. 98-7, July 1970.
11. Sherman, G. B. In Situ Materials Variability. HRB Spec. Rept. 126, 1971, pp. 180-188.
12. The AASHO Road Test: Report 2—Materials and Construction. HRB Spec. Rept. 61B, 1962.
13. McMahon, T. F., and Halstead, W. J. Quality Assurance in Highway Construction: Part 1—Introduction and Concepts. Public Roads, Vol. 35, No. 6, Feb. 1969, pp. 129-134.

EFFECTS OF METHODS A AND B BACKFILL ON FLEXIBLE CULVERTS UNDER HIGH FILLS

David W. Spannagel, Raymond E. Davis, and Alfred E. Bacher,
California Department of Transportation

Two large-diameter, structural steel plate pipes embedded in deep embankments were instrumented and tested to assess circumferential soil stress distributions, deformations, and internal strains. Construction techniques included the "imperfect trench" method (method B backfill) and positive projection (method A backfill). Method B uses layers of baled straw over a 114-in. (290-cm) pipe under 89 ft (27 m) of overfill. Method A consists of ordinary embankment material surrounding twin, 108-in. (274-cm) pipes under 160 feet (49 m) of overfill. Method B soil stress-fill height functions were nonlinear; strains and strain gradients in the pipe walls were larger than those observed for the method A installation. Radial displacements were smaller than those observed for the method A installation. Method A soil stress-fill height functions were essentially linear. Observed deformations and stresses were compared with theoretical values obtained from Marston's theory, the Iowa deflection formula, and the ring compression method. The ring compression method provided correlations that were sufficient for design purposes. Internal strains were correlated with external, measured pressures by neutral point and finite element methods. Baled straw inclusions are not recommended for future designs of flexible pipe culverts. Design can be based on ring compression with a safety factor of 4, but a 70 percent increase in soil densities may be anticipated over a period of time after fill completion.

•TWO techniques are commonly employed in backfilling culverts. The first, method A backfill, consists entirely of soil backfill from the foundation to the final grade. A second, originally suggested by Anson Marston of Iowa State University, is called the "imperfect trench" method or method B backfill; it uses a compressible inclusion in the embankment directly above the crown to reduce overburden pressure. This paper presents the results of 2 research projects conducted in California to determine the effects of these backfill types on large-diameter flexible pipe culverts embedded in deep embankments.

PURPOSE

The objectives of these projects were threefold. The first was to assess the behavior of a structural plate pipe culvert under a high fill by measuring (a) the magnitude of deformations, lateral movements, longitudinal dilations, and settlements occurring at each installation; (b) the distribution of soil pressure around the culvert periphery and in the embankment; and (c) the strain distribution within the pipe walls. The second was to assess current analytical and design techniques and compare them to observed pipe behavior. Among the design theories evaluated were Marston's theory of loads on buried conduits, Spangler's Iowa deflection formula, and White and Layer's ring compression theory. Two analytical techniques for determining internal stresses and moments from external applied loads, the neutral point and finite element methods, were also assessed. The third objective was to study the behavioral similarities and differences

Publication of this paper sponsored by Committee on Subsurface Soil-Structure Interaction.

between the 2 prototypes. Recommendations concerning the design of flexible culverts were developed from this comparison.

DESCRIPTION OF THE PROTOTYPES

Method B backfill was employed in a prototype culvert in Chadd Creek canyon in Humboldt County, California, during the fall of 1965 and spring of 1966. The culvert was a 114-in.- (290-cm-) diameter, number 1 gauge, structural steel plate pipe having 6- by 2-in. (15.2- by 5.0-cm) corrugations. An initial ellipticity was produced by a 5 percent vertical diameter elongation. The culvert periphery comprised 6 segments of 60-deg arc each with longitudinal seams at the horizontal diameter. The pipe was installed in a 7-ft- (2.1-m-) deep trench, having shaped bedding; it was backfilled with well-graded, granular backfill to a height of 1 to 2 ft (0.3 to 0.6 m) above the pipe crown. Baled straw was placed in layers 3 to 5 ft (0.9 to 1.5 m) thick, above the structure backfill. The maximum fill height, measured from the culvert crown, was 89 ft (27.1 m). Figure 1 shows the Chadd Creek installation where 3 stations were instrumented extensively to determine the effects of the following parameters (1 ft = 0.3 m):

Station	Max. Fill Height Over Crown (ft)	Structure Backfill Depth (ft)	Baled Straw Depth (ft)
A (0-96)	81	1	5
B (0+44)	89	2	5
C (1+00)	76	2	3

Method A backfill was used in the second prototype culvert, which was constructed at Apple Canyon in Los Angeles County, California, during the spring of 1966. This culvert comprised twin, 108-in.- (274-cm-) nominal-diameter, structural steel plate pipes, which were elongated 5 percent in the vertical dimension. Both pipes were constructed from six 6- by 2-in. (15.2- by 5.0-cm) corrugated plates formed into 60-deg arcs. However, various plate thicknesses, ranging from 0.109 in. [2.77 mm (number 12 gauge)] to $\frac{3}{8}$ in. (9.5 mm), were used along the culvert axis. The twin pipes were placed 4 ft (1.2 m) apart on shaped bedding in an 8-ft- (2.4-m-) deep by 24-ft- (7.3-m-) wide trench with sloping sides. Structure backfill surrounding the pipes was well-graded, granular material placed to a height of 1 ft (0.3 m) above the culvert crowns. One of the pipes was instrumented at 2 stations. Station D, at the centerline of the embankment, was covered by 160 ft (488 m) of overfill; station E, under the sideslope, was covered by 68 ft (20.7 m). Figure 2 shows the Apple Canyon installation.

INSTRUMENTATION

The instrumentation layout was essentially the same at each test station and is shown in Figures 3 and 4. Relative shape changes and wall movements were assessed by measuring the lengths of 14 chords as defined by steel spheres affixed to each pipe's internal periphery at the octant points. Assuming that the vertical diameter remained vertical, chord lengths were used to calculate the position of each sphere in a Cartesian coordinate system with origin at the pipe inversion. No attempt was made to determine the degree of rigid body rotation at either location. A second set of spheres, placed at the quadrant points [2 corrugations or 12 in. (30.5 cm) away from the primary set] was used to assess local, longitudinal elongations.

Soil pressures acting normal to the pipe periphery were measured by modified Carlson soil stressmeters made up of standard, oil-filled stressmeter metal discs fitted with linear variable differential transformers as strain transducers. Each meter was calibrated before installation by placing it between steel blocks and applying a uniaxial compression. Stressmeters were carefully embedded at pipe octant points in the structure backfill, 6 in. (15 cm) from the pipe and tangent to it. Three stressmeters were placed in the embankment material above the pipe as shown in Figure 3.

Figure 1. Culvert installation and cross section for method B backfill at Chadd Creek.

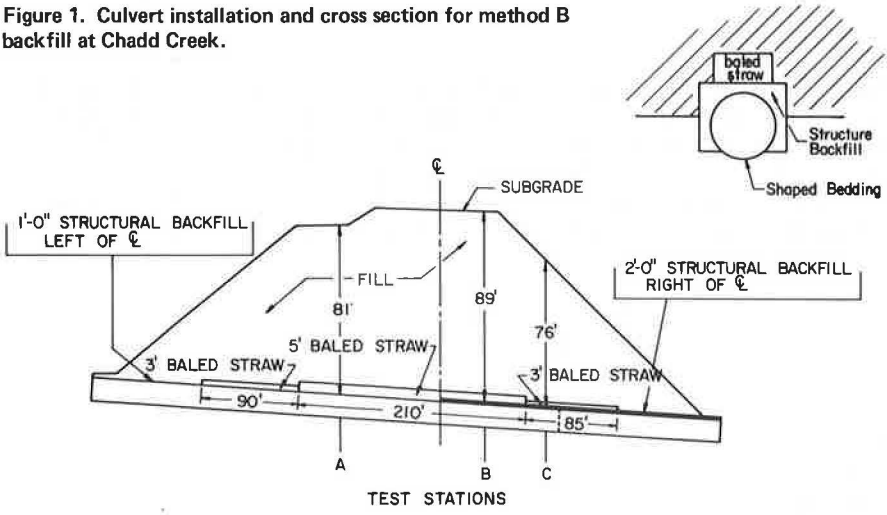

Figure 2. Culvert installation and cross section for method A backfill at Apple Canyon.

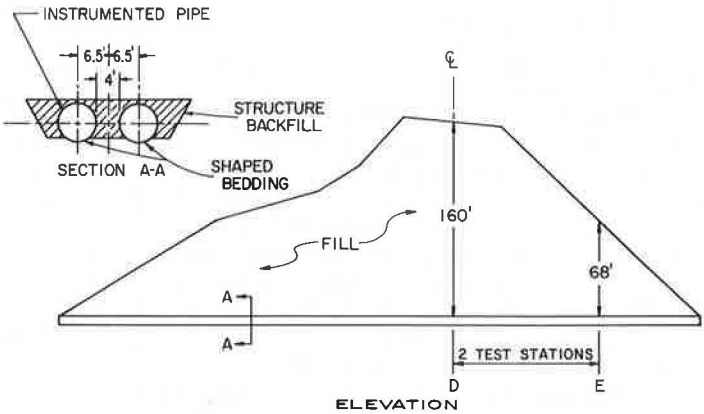

Figure 3. Typical culvert instrumentation.

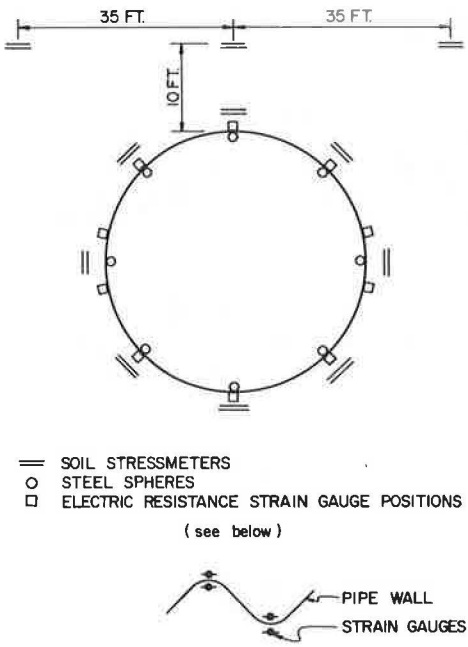

Figure 4. Typical embankment instrumentation.

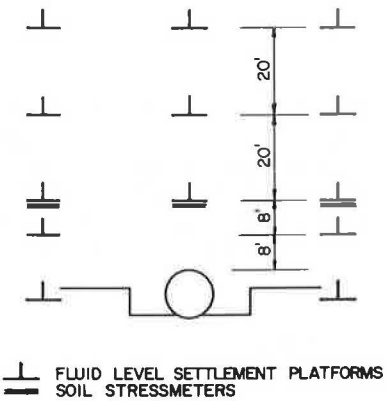

Electric resistance strain gauges were placed in quadruplets at each of the 3 upper and 3 lower octant points. Four additional quadruplets straddled the longitudinal seams at points 12 in. (30.5 cm) above and below the horizontal diameter to avoid the double plate thickness at the splice. Each quadruplet had gauges with 2 orthogonal elements at the inner and outer corrugation crowns and valleys. Gauge elements were oriented longitudinally and circumferentially. The following equations were employed for calculating stresses from observed strains:

$$\sigma_L = E(\epsilon_L + \nu\epsilon_T)$$

$$\sigma_L = E(\epsilon_T + \nu\epsilon_L)$$

where

σ_L = longitudinal stress,
σ_T = transverse stress,
ϵ_L = longitudinal strain,
ϵ_T = transverse strain,
E = Young's modulus, and
ν = Poisson's ratio.

Soil settlements were assessed by sealed, fluid-level settlement platforms installed within the embankment as shown in Figure 4. Each platform comprised an elongated, water-filled U-tube with a standpipe sealed in a closed pipe of larger diameter and buried in the embankment. The standpipe was filled with water, and an armored plastic tube connected it to a transparent tube mounted on a post on the embankment's side slope. Settlement of the platform lowered the free water surface in the visible tube where levels could be referenced to distance benchmarks. An airline and drain tube were provided to maintain atmospheric pressure at the buried standpipe and to remove overflow water. Culvert lengthening because of embankment dilation, changes in pipe camber, and lateral pipe movements were evaluated by periodic tape and level surveys through the culverts. Survey monuments were placed at intervals along the culverts to determine test station movements.

Compressive strains in the baled straw layers over the Chadd Creek culvert were measured by inverted riser settlement platforms that were made up of plates placed at the upper and lower layer surfaces and of attached reference rods that extended into the culvert below. Deformation of the straw layer was determined by measuring the distance between the pipe crown and the end of each rod.

RESULTS OF OBSERVATION

Soils Data

Physical properties of embankment soils at the 2 culvert installations were determined. Triaxial tests, the results of which are shown in Figures 5 and 6, were made by using specimens compacted in the laboratory to field-measured densities. The properties for Chadd Creek, which was sampled at 10-ft (3-m) intervals of fill depth, and Apple Canyon, which was sampled once at the surface, were as follows (1 pcf = 16 kg/m^3; 1 psf = 4.9 kg/m^2; and 1 deg = 0.02 rad):

Item	Chadd Creek	Apple Canyon
Description	Silty, sandy clay with sandstone and shale fragments	Clayey, sandy gravel derived from soft shale
Density		
Average	137 pcf	
90 percent compaction		109 pcf
Range	126 to 142 pcf	
Avg. moisture content	12 percent	
Avg. cohesion	1,690 psf	1,430 psf
Avg. internal friction angle	26 deg	28 deg

Figure 5. Triaxial test data for embankment soil at Chadd Creek.

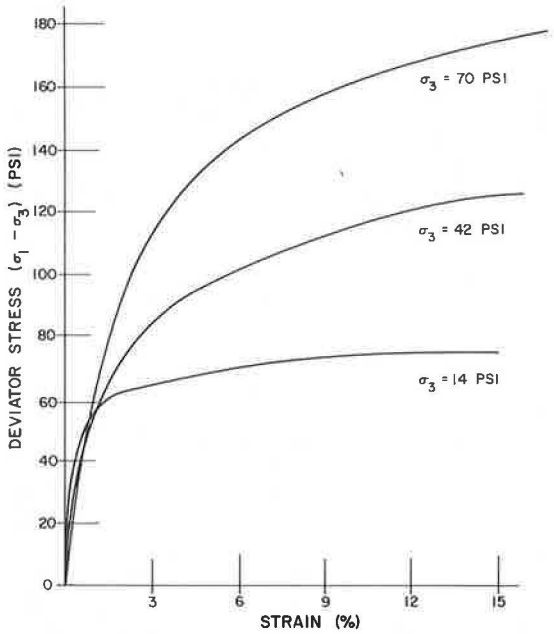

Figure 6. Triaxial test data for embankment soil at Apple Canyon.

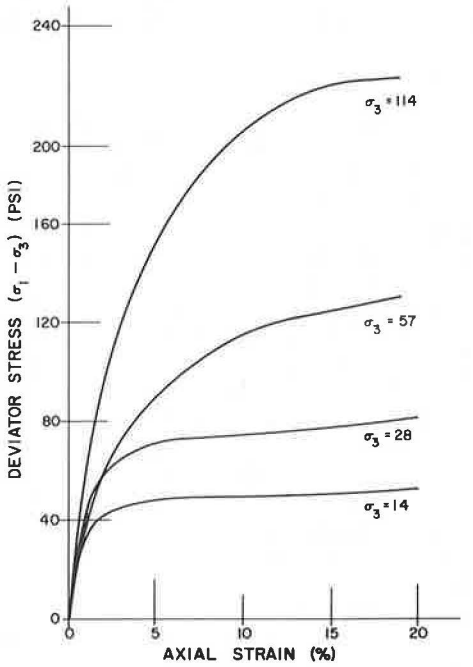

Figure 7. Axial compression tests for baled straw at Chadd Creek.

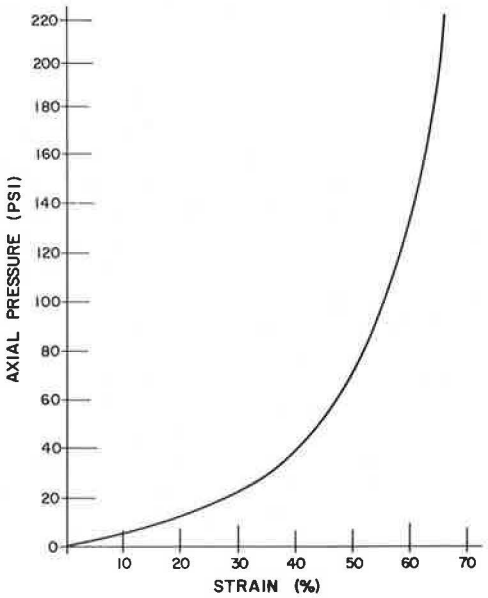

A modulus of elasticity for baled straw was assessed by uniaxial compression tests on 18- by 24- by 48-in. (46- by 61- by 122-cm) bales confined in an open-ended, rigid wooden box. A stress-strain curve is shown in Figure 7. Total compaction amounted to 12 in. (30 cm) under a 250-kip (1 112-kN) load.

Displacements

Typical, measured changes in pipe dimensions are shown in Figures 8 and 9. Horizontal diameters decreased and vertical diameters increased at both installations until fill material reached the crown level. Thereafter the trend reversed; at 8 ft (2.5 m) of overfill at Chadd Creek and 15 to 20 ft (5 to 6 m) at Apple Canyon, the measured diameters assumed their original lengths. The trend again reversed at 20 to 40 ft (6 to 12 m) of overfill at all 3 stations at Chadd Creek, but no such reversal was observed at Apple Canyon.

The final displaced shape of the Chadd Creek culvert indicated that the vertical diameter had shortened at 2 stations and had returned to its initial length at the third. Horizontal displacements ranged from an increase of 0.4 in. (1.0 cm) to a decrease of 0.5 in. (1.3 cm). These changes were relatively small; the largest occurred at station C under the thinnest overfill and straw layers. Final displacements at Apple Canyon were much larger than those at Chadd Creek. Under 160 ft (49 m) of overfill the vertical diameter at station D decreased 2 in. (5 cm) and the horizontal diameter increased 1.5 in. (4 cm). Station E diameter changes were smaller.

Transverse embankment dilation resulted in elongation of prototype barrels at both sites. Local elongations, measured at each station, were as large as 0.10 in./ft (0.833 cm/m) at Chadd Creek. Tape surveys made between stations A and C indicated an average elongation of 0.025 in./ft (0.208 cm/m) over a 140-ft (43-m) distance.

Local elongation at Apple Canyon amounted to 0.01 in./ft (0.083 cm/m) at station D and 0.02 in./ft (0.167 cm/m) at station E. The average elongation determined by surveys was 0.004 in./ft (0.033 cm/m). These apparent contradictions may be explained by the fact that the overall elongations were measured across the center of embankment dilation where no stretching would be expected.

Soil Pressure Data

Typical soil pressure-fill heights for Chadd Creek and Apple Canyon are shown in Figures 10 and 11. Chadd Creek pressure functions were nonlinear during the fill construction period. For 19 months after fill completion, most stressmeters exhibited temporary stabilization or slight decreases. The majority of meters showed higher pressures after 28 months. Soil pressures at station C under the side slope evidenced distinct longitudinal overburden distribution as they continued to increase at nearly the same rate during the 3-month interval between reaching maximum overfill at that station and fill completion at the roadway centerline.

Pressure-fill height functions at Apple Canyon were nearly linear (Fig. 11) during fill construction. Pressure increases that occurred at station E side slope during the placement of additional fill at station D are evidenced clearly in the center portion of the plot. Pressures rose rapidly for 6 months after fill completion and then at a slower rate to an average level 70 percent higher 36 months after fill completion.

Figures 10 and 11 also depict typical variations in soil effective density as a fraction of fill height. Effective density is the equivalent fill density required to produce a given measured pressure under hydrostatic conditions. The relationship between pressure and effective density is

$$ED = \frac{\Delta P}{\Delta H} \times C$$

where

ED = effective density,
ΔP = change in pressure in psi for a given change in fill height,

Figure 8. Typical measured changes in culvert diameter for method B backfill at Chadd Creek.

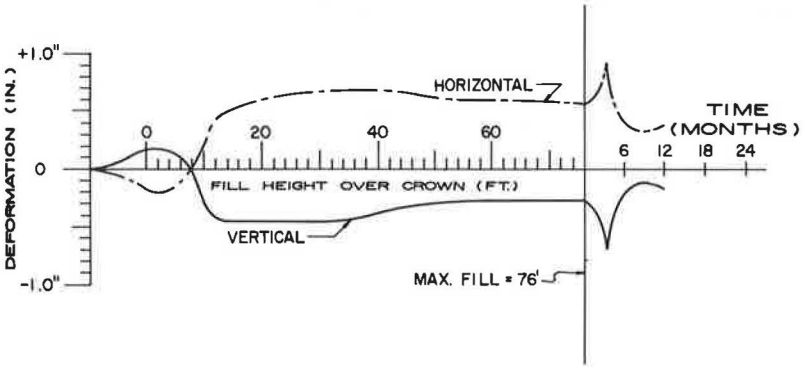

Figure 9. Measured changes in culvert diameter for Method A backfill at Apple Canyon.

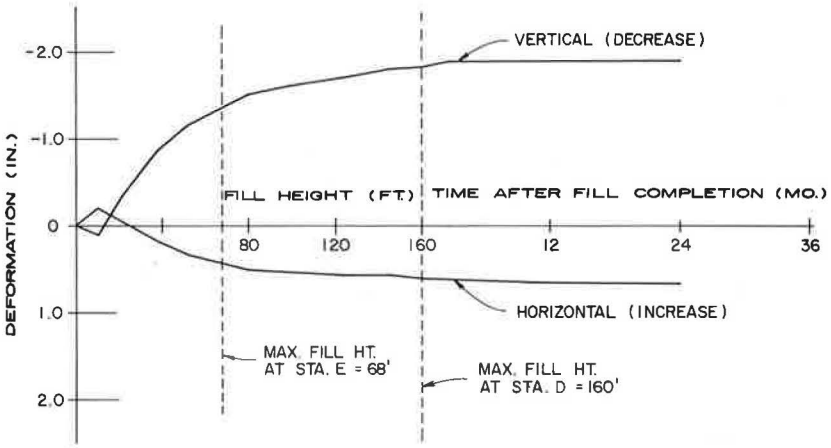

Figure 10. Soil pressure and effective density as functions of fill height and time at Chadd Creek.

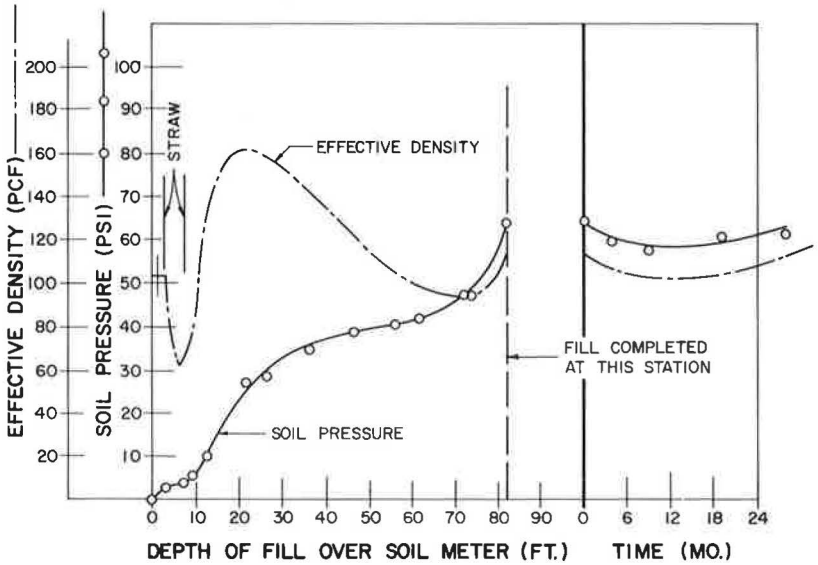

Figure 11. Soil pressure and effective density as functions of fill height and time at Apple Canyon.

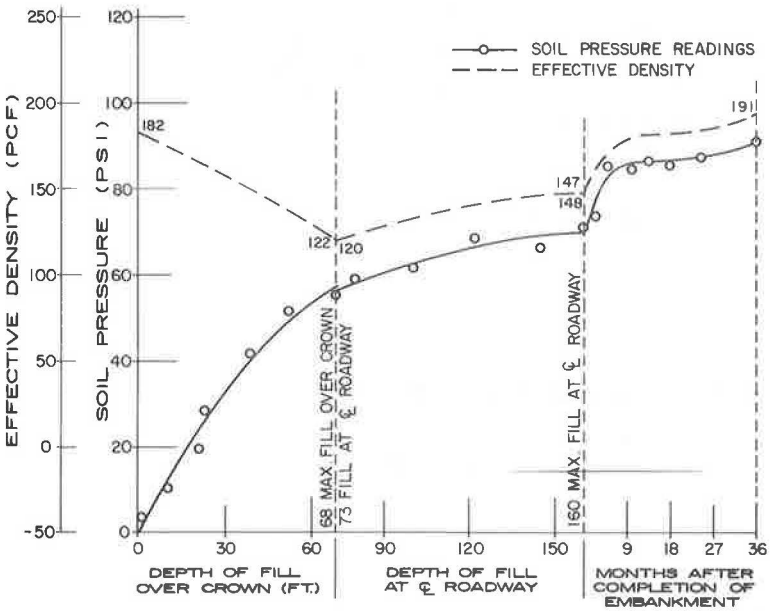

Figure 12. Composite effective density profile for 80 feet of overfill at Chadd Creek.

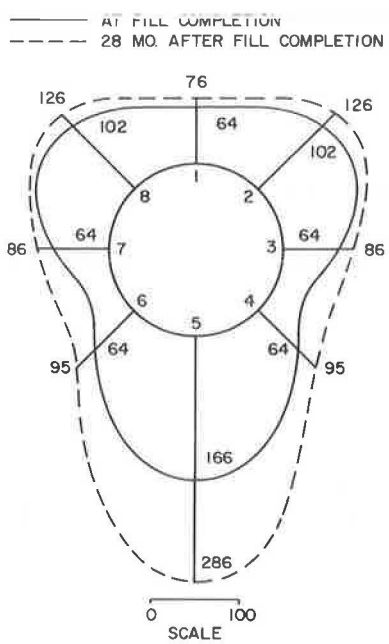

Figure 13. Effective density profile for 160 ft of overfill at Apple Canyon.

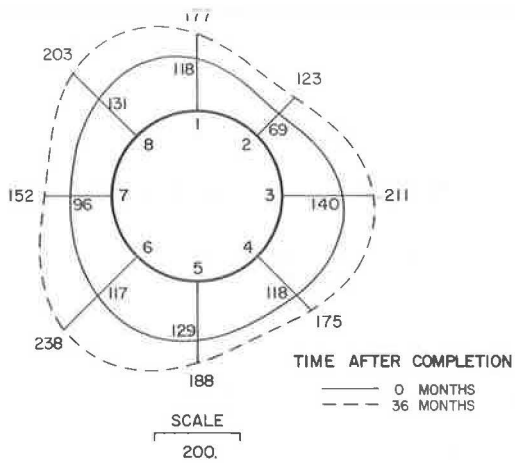

ΔH = fill height in feet, and
C = a constant required for units conversion (144 sq in./sq ft in this case).

Typically, the effective densities at Chadd Creek were highly nonlinear and reached relative maxima when the embankment was 10 to 60 ft (3 to 18 m) above the meters and relative minima at fill heights of 70 to 85 ft (21 to 26 m). These extremes occurred in the lower portion of each range for most meters. Apple Canyon exhibited linear effective density functions that decreased slightly during fill construction and showed increases commensurate with pressure changes thereafter.

Composite, circumferential effective density distributions for Chadd Creek are shown in Figure 12. These profiles were constructed by averaging the readings from all test stations to produce a distribution symmetrical about the vertical diameter. During the averaging process, each meter position was characterized by a number of readings that were close to each other in magnitude and 1 reading that differed greatly from the rest. These odd readings, which might be attributed to meter idiosyncrasies and local soil heterogeneity, were eliminated before developing the composite profiles.

The profiles depict the influence of the compressible inclusion in distributing the vertical load across the top of the pipe. Large bulbs of effective density were noted at both upper octant points and the inversion. The density increases that occurred 28 months after fill completion also are shown; the largest increases were observed at the invert.

The effective density profiles for Apple Canyon are shown in Figure 13. Because only 1 station was located under the maximum fill height, averaging to obtain symmetry was not possible. These profiles indicate a tendency toward a circumferential distribution. A small degree of asymmetry may be attributed to the closeness of the second pipe and to relatively large lateral movements. Effective density increases after fill completion averaged 60 to 70 percent.

At Chadd Creek, large effective densities that were twice the actual density as determined by compaction tests were observed in the exterior prisms as a result of transfer of load from the settling interior prism over the straw by shearing forces. Apple Canyon exhibited exterior prism densities that were lower than those over the pipe crown.

Observed Strains

Stretching of both prototype culverts because of embankment dilation as evidenced by the surveys and local longitudinal deformations was also evidenced in strain patterns of those elements of the resistance strain gauges that were oriented longitudinally along the pipe axis. Most of the inner and outer crown elements exhibited compressive strains although the corrugation valley elements manifested tensile strains (as might be expected when pipe is stretched like an accordion). Exceptions to this behavior were noted at each installation at stations B and D near the center of the embankment where a small amount of dilation would be expected. These exceptions probably resulted as differential settlement reduced the culvert camber and produced a longitudinal bending moment in the pipe with its upper half in compression.

Circumferential strain data plotted for cross sections of the pipe wall at both culverts indicated that plane sections remained plane for all gauge quadruplets at each test station. Variations in individual gauge strains as fill height increased were smooth, nonlinear functions; the nonlinearity probably was the result of strain redistribution.

Strain data were used in conjunction with material properties to determine the longitudinal and circumferential stresses. Specified yield and ultimate strengths were 28,000 and 42,000 psi (193 000 and 290 000 kPa) respectively for both pipes. Tests of coupons taken from the corrugated and curved pipe plates produced average yield values and ultimate strengths for the Chadd Creek pipe of 45,900 and 56,400 psi (316 500 and 388 900 kPa) respectively. Corresponding test values for the Apple Canyon pipe averaged 57,300 and 69,300 psi (395 100 and 477 800 kPa).

Figures 14 and 15 show typical stress profiles for the Chadd Creek and Apple Canyon pipes respectively. Circumferential strains commensurate with measured yield

Figure 14. Extreme fiber stress profile for 80 ft of overfill at Chadd Creek.

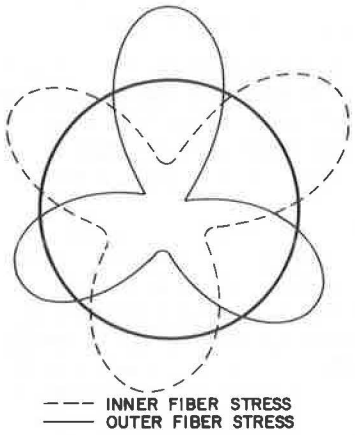

Figure 15. Extreme fiber stress profile for 80 ft of overfill at Apple Canyon.

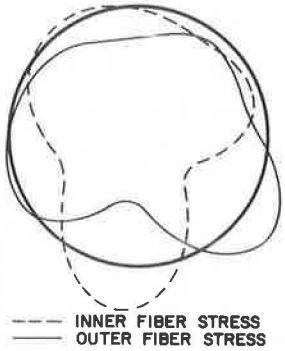

Figure 16. Comparison of moment profiles for method A backfill at Apple Canyon and method B backfill at Chadd Creek.

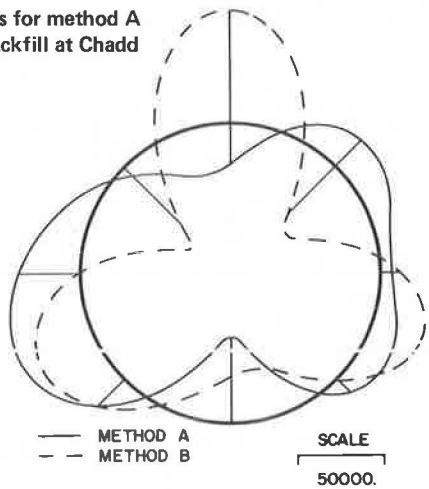

Figure 17. Comparison of crown pressures calculated by various theories and those actually observed for method B backfill.

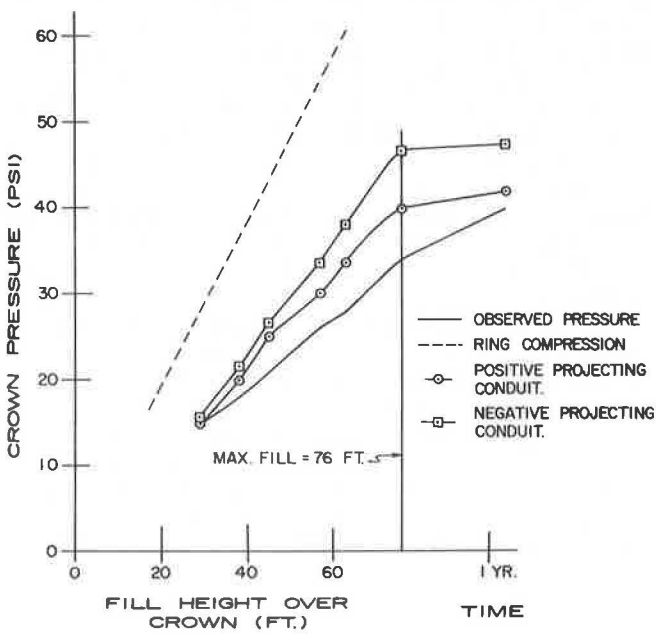

strength were first observed at Chadd Creek at the crown of each test station with between 63 and 71 ft (19 and 22 m) of overfill. Subsequently, stresses at station A indicated yield along the right side of the pipe from the crown to the inversion. Circumferential yield stresses at the remaining stations were confined to the crown and upper left octant points. Longitudinal yield stresses were observed at the crown and just below the left quadrant point after fill completion at station A only.

Yield strains were measured in the Apple Canyon pipe at station D only. Initial circumferential yield occurred at the inversion under 160 ft (49 m) of overfill and subsequently spread to the lower left octant point, right quadrant point area, and the crown. Longitudinal yield strains were recorded at the crown area at various times following embankment completion.

Station E at Apple Canyon was located in a section of number 1 gauge pipe as were all 3 stations at Chadd Creek. Therefore, stresses, moments, and thrusts observed in the 2 culverts were compared for a fill height of 62 ft (19 m) above each culvert crown, an elevation at which data were collected at all test stations. The maximum tensile stress was found to be about 35 percent higher in the Chadd Creek pipe than in the Apple Canyon pipe, but the maximum compressive stress was only about 4 percent larger. The stress gradient, the difference between stress values at adjacent octant points, averaged 43 percent larger at Chadd Creek.

Circumferential stresses were used in conjunction with pipe section properties to calculate bending moments and thrusts in culvert walls. The influence of curvature on the bending moments was assessed and found to be negligible. At Chadd Creek the largest observed moments and thrusts occurred at the crown at each test station. Maximum values at Apple Canyon were observed at the inversion.

The method used for comparing stresses of the 2 prototypes was also used for comparing bending moments and thrusts. The observed differences between maximum positive and negative moments were negligible, but the moment gradient was about 57 percent higher at Chadd Creek. Figure 16 shows a comparison of moment profiles for both culverts. The maximum thrust and thrust gradient were significantly larger at Apple Canyon.

THEORETICAL ANALYSES

Marston's Theory

The theory of loads on buried conduits, developed by Anson Marston, is 1 method used to determine the vertical load on a culvert crown. The theory and nomenclature are well documented (1, 3). The analysis considers the relationship of settlement of the mass of fill directly over the culvert to that of adjacent fill masses and the resulting transfer of load by shear forces from 1 mass to the other.

The data obtained from the sealed, fluid-level settlement platforms; level surveys; and riser settlement platforms were used to determine the crown load at each tested station by Marston's theory. The settlement ratio, an abstract quantity representing the relative settlement of the soil masses above and to the sides of the conduit, normally is assumed in design but, in this case, was calculated from the settlement data at both culverts. The plane of equal settlement, the horizontal plane above which the settlements of the interior and exterior prisms are equal, was also calculated and compared to the observed embankment settlements.

The Chadd Creek culvert with its baled straw inclusion was classified as an imperfect trench conduit according to Marston's theory. The imperfect trench condition was analyzed as a negative projecting conduit. However, because the pipe actually was placed on original ground, and a trench with sloping sides then was artificially constructed around the barrel, the installation also resembled a positive projecting conduit. For comparison, crown loads were calculated for both classifications.

The observed plane of equal settlement lay between 30 and 32 ft (9 and 10 m) above the crown at Chadd Creek. The negative projecting conduit equations predicted the location of this plane more accurately than did the positive projecting conduit equations. Agreement between the theoretical and observed pressures was poor. Positive projecting conduit crown pressures averaged 17 percent too high at the time of fill com-

pletion and ranged from 5 percent low to 50 percent high after 1 year. Negative projecting conduit pressures were high by 8 to 37 percent at the time of fill completion and were high by 13 to 36 percent 1 year later. Figure 17 shows the comparison between theoretical and observed crown pressures for Chadd Creek.

Placement of the twin pipe culverts at Apple Canyon in a wide, shallow trench also produced conditions resembling both positive and negative projecting conduits. Accordingly, crown loads were calculated for both conditions. During fill placement, excellent correlations were obtained between the theoretical and observed crown pressures for both test stations. The average difference between the negative projecting conduit pressures and the measured values was only about 3.3 percent during fill construction, but, as shown in Figure 18, the theory failed to predict the pressure increases after completion.

Spangler's Iowa Deflection Formula

Spangler developed an expression for the anticipated pipe deformations known as the Iowa deflection formula (2, 3). The formula is based on Marston's crown pressures and an assumed peripheral pressure distribution and pipe shape. This formula was applied to both culvert prototypes even though the measured pressure distributions and initial pipe shapes did not correspond to the theory's assumptions.

Design based on the formula requires a knowledge of the installation geometry and the use of assumed constants based on soil compaction (modulus of soil reaction, E') and ratio of final to instantaneous deflections (deflection lag factor, D_L). Observed moduli of soil reaction have been reported to range from 230 to 8,000 psi (1 590 to 55 160 kPa). AASHO specifications suggest a value of 1,400 psi (9 650 kPa) for E', and 1.25 for D_L, when backfill is placed at 95 percent compaction.

At Chadd Creek use of the AASHO design values resulted in calculated deflections that ranged from 10 to 16 times larger than the measured vertical displacements. The appropriate value for E' at Chadd Creek would be from 16,000 to 20,500 psi (110 300 to 141 300 kPa).

Application of the Iowa deflection formula at Apple Canyon using specified E' and D_L values resulted in theoretical deformations 8 to 11 times larger than those observed. Calculated values for E' were about 16,400 psi (113 100 kPa). The extremely large E' values at both culverts can probably be attributed to the confinement afforded by the trenches in which the culverts were placed. This confinement limits the horizontal displacement and thus reduces vertical movements.

Ring Compression Theory

White and Layer's ring compression theory (3) is a method for determining required pipe wall thickness. The theory assumes that the total load on a culvert, the hydrostatic weight of soil above the pipe, is resisted by the wall thrusts. A safety factor of 4 is normally applied to the loads. The crown pressures as calculated for hydrostatic loading are compared with the observed crown pressures at each prototype as shown in Figures 17 and 18.

Ring compression thrust at Chadd Creek was about 6 percent larger than actual wall thrusts when a safety factor of 1 was used; this indicates that design based on the normal safety factor would be adequate in this case. For Apple Canyon, calculated thrusts were only 52 percent of the measured thrusts when the safety factor was 1. A safety factor of 4 yielded thrusts slightly above twice the observed value.

Neutral Point Analysis

Correlations between external applied loads and internal stresses and displacements were established using the neutral point method of analysis. This method is an extension of the general method of indeterminate structures, the theoretical basis of which is described by Grintner (4). For analysis, a culvert subjected to an arbitrary external pressure distribution is made statically determinate by assuming the pipe to be cut at its invert. Loads are applied to a number of small segments of equal

Figure 18. Comparison of crown pressures calculated by various theories and those actually observed for method A backfill.

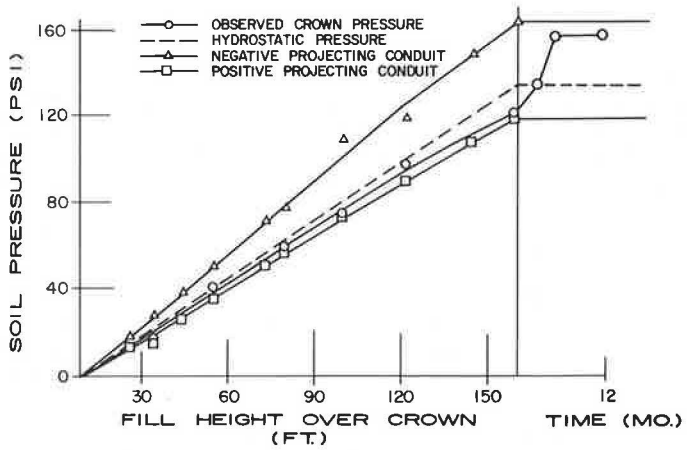

Figure 19. Comparison of observed bending moments and those calculated by the neutral point method for method B backfill.

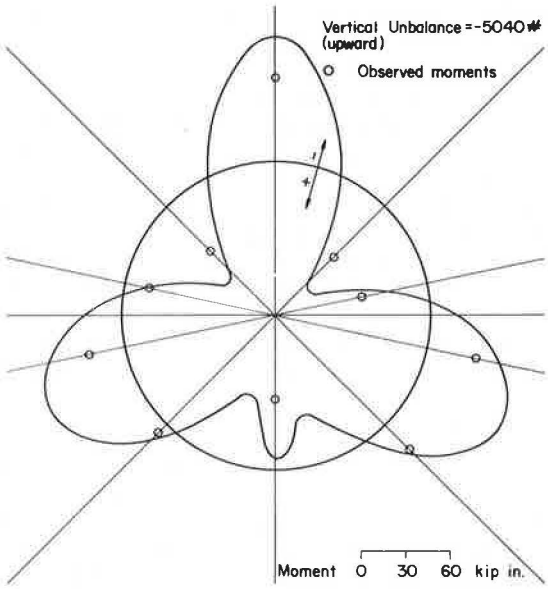

Figure 20. Comparison of observed stresses and those calculated by the neutral point method for method B backfill.

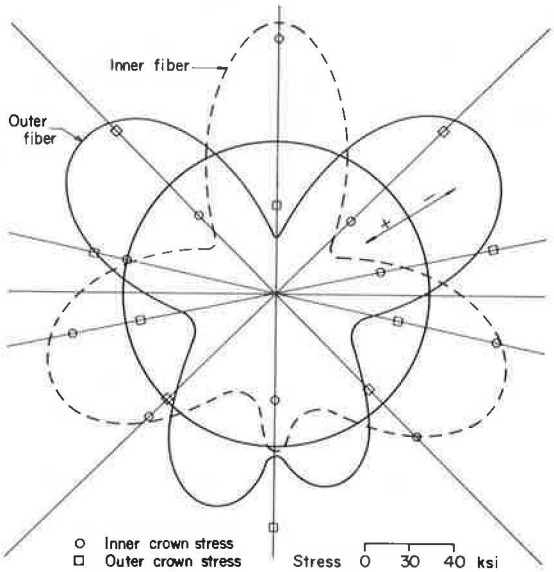

length called voussoirs. One end of the cut ring is assumed to be clamped to a rigid support and the other end is connected by a hypothetical rigid bracket to the centroid of elastic weights or neutral point. Restoration of compatibility after loads are applied is achieved by the application of redundant forces at the neutral point. Moments, thrusts, shears, and displacements are calculated from these forces and the applied loading.

Determining accurate pressure distribution and true pipe shape was a critical phase of the analysis. For low fill heights, the tolerance of the pressure meters was a considerable percentage of the readings, and transducer errors were possible causes for poor correlations between analytical and experimental results. Another problem was the lack of static balance of forces acting on the culvert. The soil shear stresses must be known to produce equilibrium, but, because shear stress transducers were not available, these data were not obtained. Attempts to force static balance by using either a soil friction component or an assumed shear stress distribution reduced the load unbalance but did not improve the correlations with observed quantities.

The analysis was extremely sensitive to small variations in pipe shape. The procedure that best described the shape used 2 vertical semiellipses established from the positions of the octant point steel spheres.

Good correlations were obtained between the theoretical bending moments and stresses and those actually observed at Chadd Creek when a horizontally balanced average pressure distribution and the final displaced shape were used as input. Figure 19 shows the correlation of bending moment. Extreme fiber stress correlations are shown in Figure 20. An analysis using the initial pipe shape also was made, the results of which indicated that stresses and displacements could be predicted with reasonable accuracy if the pipe shape and soil pressures could be predetermined accurately. It was noted, however, that the sensitivity of the method to small errors in either parameter requires that both be predicted precisely.

At Apple Canyon the exact pipe shape was known, but because of the unavailability of soil shear stress data the pipe static equilibrium could not be established. Hence, the neutral point method did not predict pipe behavior accurately.

Finite Element Analysis

The finite element method was used to analyze the Apple Canyon installation, and the output was compared to the measured soil pressures, pipe displacements, moments, thrusts, and embankment settlements. For large embankments, analysis must be based on accurate soil properties and geometric models. At this installation extensive soil property data were not available and no foundation investigation was performed. Soil samples taken from the completed embankment provided the only available data.

Finite element analyses were based on a linear, elastic soil model and a nonlinear, hyperbolic model developed by Kulhawy, Duncan, and Seed (5). Both models resulted in computed peripheral soil pressure distributions that agreed with the observed pressures within 20 percent, but correlations between measured and theoretical displacements, settlements, and pipe stresses were very poor.

CONCLUSIONS

The single pipe installation at Chadd Creek produced nearly symmetric density, stress, and moment profiles for method B backfill. The dual pipe configuration of Apple Canyon was at least partially responsible for the asymmetry observed for method A backfill. We believe, however, that the effects of these construction differences are not of sufficient significance to invalidate any comparisons between the 2 projects.

The nearly uniform pressure profile, linear pressure-fill height functions, and small stress and moment gradients observed at Apple Canyon suggest that method A backfill provides more favorable conditions for flexible culverts than does method B backfill. Control of deflections, a critical consideration in present culvert design, was adequate with either method, although vertical deflections under method B were smaller. Based on the results of these 2 research projects, the use of method B backfill for flexible culverts is not recommended.

Observations at Apple Canyon suggest a uniform peripheral distribution of pressure as a basis for design. However, the large fiber strains demonstrate that significant bending moments may result from small departures from either a circular pipe configuration or a uniform pressure distribution. Such departures are highly probable and should be considered in design.

In general, the design methods discussed in this paper did not predict the observed culvert behavior accurately. Good correlations were obtained between observed crown pressures and theoretical pressures determined by Marston's theory during construction. This method, however, failed to determine the large increases in pressure that occurred after construction was completed, and it provided no facility for predicting the remainder of the peripheral pressure distribution. Moreover, the method requires prediction of soil properties that cannot be accurate. The ring compression theory, including the safety factor, proved conservative in all cases. It is recommended that soil densities used in the ring compression theory be increased by 70 percent to account for long-term effective density increases and to provide a long-term factor of safety of 4.

ACKNOWLEDGMENTS

This research was financed in part by and conducted in cooperation with the Federal Highway Administration. The work was performed under the direction of the California Department of Transportation, Office of Structures. The contents reflect the views of the authors and not necessarily those of the Federal Highway Administration or the California Department of Transportation.

REFERENCES

1. Spangler, M. G. Field Measurements of the Settlement Ratios of Various Highway Culverts. Eng. Exp. Station, Iowa State Univ., Bull. 170, 1950.
2. Spangler, M. G. The Structural Design of Flexible Pipe Culverts. Eng. Exp. Station, Iowa State Univ., Bull. 153, 1941.
3. Krizek, R. J., Parmelee, R. A., Kay, J. N., and Elnaggar, H. A. Structural Analysis and Design of Pipe Culverts. NCHRP Rept. 116, 1971.
4. Grinter, L. E. Theory of Modern Steel Structures. Macmillan Publishing Co., Inc., Vol. 2, Chapter 8, Riverside, N. J., 1949.
5. Kulhawy, F. H., Duncan, J. M., and Seed, H. B. Finite Element Analysis of Stresses and Movements in Embankments During Construction. College of Engineering, Univ. of California, Berkeley, Rept. No. S-69-8, 1969.

PERFORMANCE OF A REINFORCED EARTH FILL

Jerry C. Chang, Raymond A. Forsyth, and John L. Beaton,
California Department of Transportation

Design methods and field performance studies are presented for the reinforced earth embankment on Cal-39 in Los Angeles County. Rankine's state of stress theory was employed to derive the equations for designing the reinforcement. Strain energy principle was introduced to develop the equations for designing the steel skin plate. Comprehensive instrumentation was installed to study the field behavior. The field-observed data indicate close agreement between the design assumptions and field behavior. Recommendations concerning stability analyses and corrosion were also included.

•REINFORCED earth is soil mass composed of fill strengthened by metal or plastic reinforcements and enclosed at the front face by skin elements. Since at least Roman times, builders have been aware of the stabilizing effect of including reinforcing elements in earthwork. In his commentaries, Julius Caesar (1) stated

> All Gallic walls are commonly of this fashion: straight beams are laid together upon the ground at equal intervals of two feet, their inner ends braced together, while along the outer front the interspaces are packed with large blocks of stone, and the whole is covered with earth. Upon these is laid a second similar row of beams, so that while the same interval is maintained, the beams of the two rows are not contiguous. . . .In this way the whole wall is built up course by course until the full height is maintained.

The beams described were to reinforce the earth with a stone outer face to resist impact or battering. The use of earthwork reinforcement based on rational design was reported in 1969 by Henri Vidal (2). In October 1972, the first application of reinforced earth to highway construction in the United States was carried out by the California Department of Transportation to reopen a section of Cal-39 in the San Gabriel Mountains, Los Angeles County, that had been closed by a surficial debris slide during a heavy spring storm in 1969. A description of the slide and the rationale for selecting reinforced earth for its correction were reported by Chang, Forsyth, and Smith (3) in 1972. They also presented the results of soil investigation and stability analysis and equations developed for analyzing the stresses in the reinforcing strips. By using these equations, the size, length, and spacings of the suggested reinforcement were evaluated.

In this paper, equations for analyzing the stresses in the skin plates, comparisons between the field instrumentation data, and analytical results for both reinforcing strips and skin plates are presented. Results of field pulling tests on the reinforcement are included also.

EMBANKMENT GEOMETRY

The reinforced earth fill was constructed on top of a random fill embankment founded over the slide debris. At the bottom of the slide debris a toe buttress was built to act as a stabilizing fill embankment. The overall height of the system was approximately 360 ft. The reinforced earth fill had a maximum height of 55 ft and length of 528 ft.

Publication of this paper sponsored by Committee on Embankments and Earth Slopes.

Figure 1. Plan and profile.

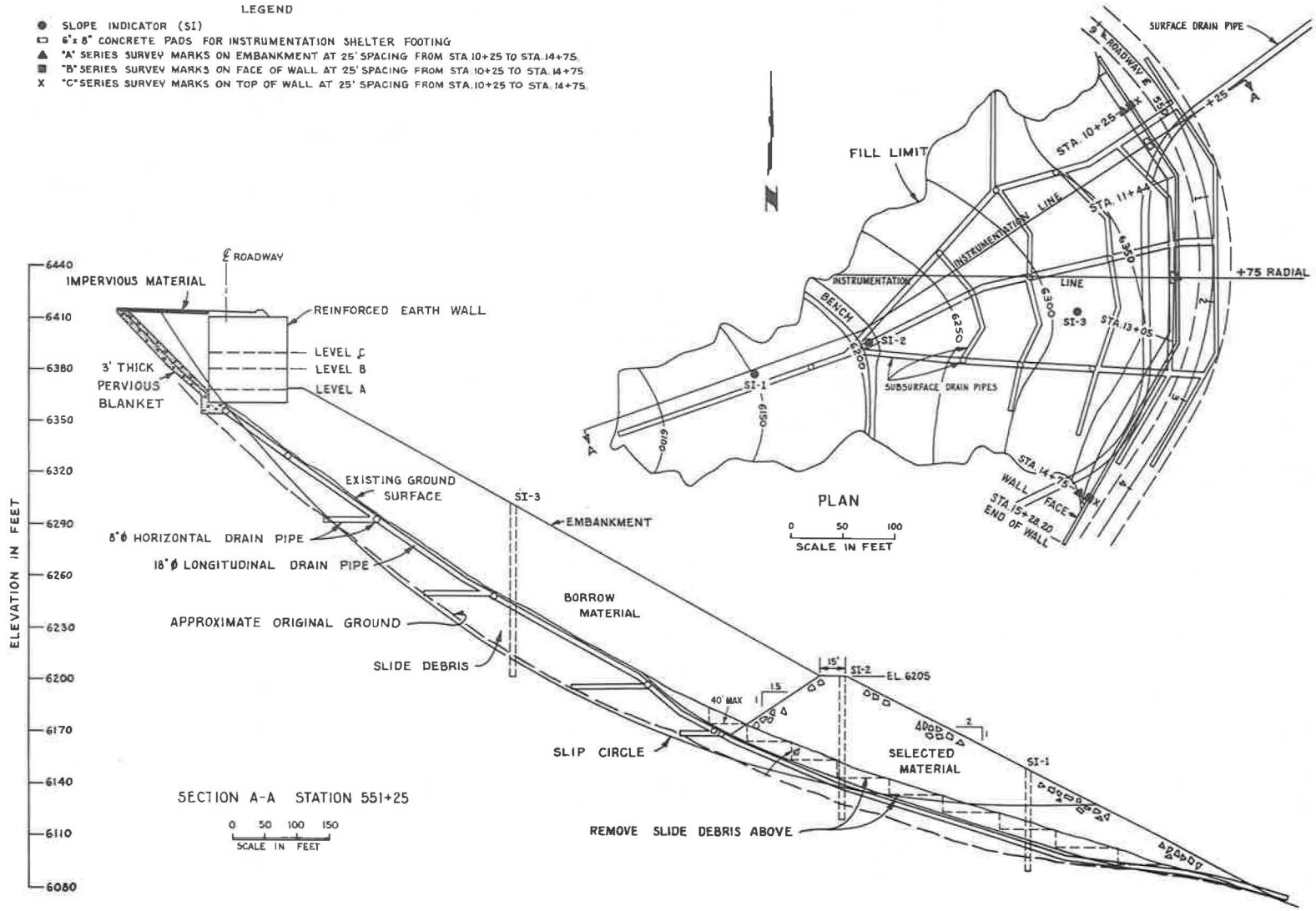

A system of surface and subsurface drain pipes was installed to remove surface water and seepage. The embankment is shown in plan and profile in Figure 1.

DESIGN OF REINFORCEMENT

The 2 basic equations for analyzing the reinforcement design were based on Rankine's state of stress theory and the principles shown in Figures 2 and 3. The equations were developed as follows assuming a Rankine's active earth pressure, p, acts on the inner face of the skin plate (3):

$$p = K_a \gamma H$$

where

K_a = coefficient of active earth pressure,
γ = unit weight of soil, and
H = height of fill.

A force, T, will be developed in the reinforcing strip, and it tends to either pull the strip out or fail it in tension. The pull force, T, and the stress, f_s, developed in the strip will be

$$T = K_a \gamma H d \Delta H \tag{1}$$

$$f_s = \frac{K_a \gamma H d \Delta H}{bt} \tag{2}$$

where

d = horizontal spacing of strips,
ΔH = vertical spacing of strips,
b = width of steel strip, and
t = thickness of steel strip.

Figure 2. Schematic of reinforced earth fill.

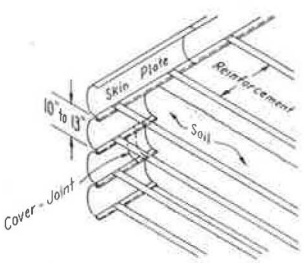

Figure 3. Schematic of reinforced earth block.

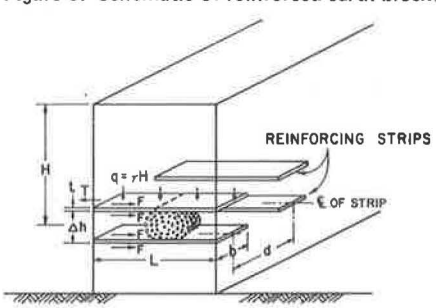

Let the skin-friction angle be ϕ_u. A friction force, F, will be developed on each face of the strip so that

$$F = \gamma H b L \tan\phi_u \tag{3}$$

The factor of safety against slippage, S.F., will be

$$S.F. = \frac{2F}{T} = \frac{2\gamma H b L \tan\phi_u}{K_a \gamma H d \Delta H} = \frac{2bL\tan\phi_u}{K_a d \Delta H} \tag{4}$$

Equation 2 was used to compute theoretical steel stresses for comparison to those measured by field instrumentation.

DESIGN OF SKIN PLATES

The standard shape of the skin plate consisted of a semielliptical element 10 to 13 in. high with a thickness of about $\frac{1}{8}$ in.

To simplify the stress analysis, the following assumptions were made for a semicircular section of skin plate: (a) the soil pressure distribution and deformation

Figure 4. Loading diagram on skin plate.

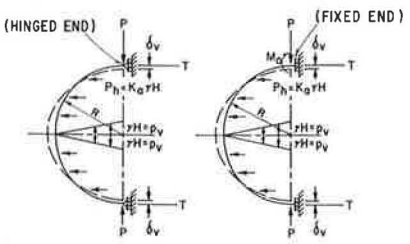

configuration as shown by Figure 4 and (b) that a vertical load, P, representing a resultant force transferred from a uniform vertical pressure acting along an effective length of reinforcing strip will cause a vertical deformation, δ_v. This vertical deformation was assumed to have the same magnitude as the settlement of the soil mass caused by a uniform vertical soil pressure acting on the top and bottom row of reinforcement.

By using strain energy principles described by Seely and Smith (5), the equations for computing the vertical load, P, and the end moment, M_a, were developed as follows (4): For hinged-end conditions as shown in Figure 4

$$P = \frac{4EI\delta_v}{R^3\pi} - \frac{4K_a\gamma HR}{3\pi} - \frac{\gamma HR}{24\pi}(3\pi - 32) \tag{5}$$

and for fixed-end conditions

$$P = \frac{\delta_v EI}{\pi R^3}\left(4 - \frac{32}{8 - \pi^2}\right) + \gamma HR\left(\frac{4 - 4K_a}{3\pi} - \frac{1}{8}\right) - \frac{8\gamma HR}{8 - \pi^2}\left[\frac{4 - 4K_a}{3\pi} - \frac{(1 + \pi - \pi K_a)}{8} + \frac{1}{9}\right] \tag{6}$$

and

$$M_a = \frac{8\delta_v EI}{R^2(8 - \pi^2)} + \frac{2\pi\gamma HR^2}{(8 - \pi^2)}\left[\frac{4 - 4K_a}{3\pi} - \frac{(1 + \pi - \pi K_a)}{8} + \frac{1}{9}\right] \tag{7}$$

The magnitude of P depends on the restraint conditions at the ends and the value of vertical settlement, δ_v. When the unknown load, P, and the unknown bending moment, M_a (Fig. 4), are determined, the stresses developed in the skin plate can be calculated. Equations 5, 6, and 7 can be solved by measuring the vertical deformations, δ_v, in field performance studies or laboratory scale model tests. For design purposes, a value of δ_v can be determined by estimating the embankment settlement.

CONSTRUCTION MATERIAL

Triaxial tests (consolidated drained condition) on the backfill material resulted in a friction angle, ϕ, of 40 deg at 95 percent relative compaction. From this, Rankine's coefficient of active earth pressure, K_a, was calculated to be 0.22. The coefficient of earth pressure at rest, K_o, was computed to be 0.36 based on Jaky's expression (6), $K_o = 1 - \sin\phi$. Laboratory skin friction tests between the galvanized steel strip and the soil resulted in a skin-friction angle of 31 deg.

The dimensions of the steel reinforcing strips were as follows:

1. Thickness: 0.118 in.,
2. Width: 2.362 in., and
3. Length: 22.79 to 46.0 ft.

Laboratory tests resulted in a yield strength of 37,000 psi; an ultimate strength of 40,000 psi; a Young's modulus of 28.5×10^6 psi; and a Poisson's ratio of 0.28.

INSTRUMENTATION

To monitor the behavior of the completed structure, comprehensive instrumentation

was installed in the field. Included were

1. Slope indicators to measure internal deformation of the embankment and slide debris;
2. Settlement platforms to measure vertical settlements;
3. Extensometers to measure soil strains;
4. Soil pressure cells to measure soil stresses;
5. Strain gauges to measure stresses developed in the reinforcing strips and skin plates; and
6. Gauge points to measure deformations of the skin plates and the wall face. Locations of the instruments are shown in Figures 1 and 5. All instruments were read periodically during construction and for approximately 1 year after completion of the embankment.

STRESSES IN THE REINFORCING STRIPS

The daily history of the axial stresses in the steel strips is shown in Figure 6. They were calculated based on average strain recorded on top and bottom of the strip and a modulus of elasticity of 28.5×10^6 psi. For comparison, steel stresses assuming active earth pressure and at rest cases were computed by using Eq. 2 superimposed on Figure 6. The lowest axial stresses were measured near the wall face. After completing the fill, the stresses near the wall face decreased with time and eventually became compressive at level A. This phenomenon probably was due to the restraint provided by the berm. At 15 and 25 ft from the wall face, the stresses in the strips increased with time and finally reached the calculated stress, σ_a, based on coefficient of active pressure, K_a. At level B, the steel stresses at 15 ft from the wall face decreased with time to values much lower than σ_a; the stresses at 25 ft from the wall face increased with time and approached the calculated stress, σ_o, based on coefficient of earth pressure at rest, K_o. At level C, the magnitude of all steel stresses decreased with time and approached σ_a.

SOIL STRESSES

Figure 7 shows the soil stresses measured at section III, station 551+75. The ratio, K, between the horizontal stress and vertical stress is also plotted on this figure. The γH lines represent the theoretical vertical soil stresses computed by using a unit weight, γ, of 143 pcf and the corresponding depth of fill, H, over each instrumentation level. The K values varied irregularly during and immediately after construction presumably because of the effect of compaction. As the height of fill increased over the instrumentation level, the influence of compaction diminished. After completion of the fill, the K values still varied between 0.5 and 0.8 at this section as compared to the calculated K_a of 0.22 and K_o of 0.36. At the other sections (not shown) the K values varied from 0.11 to 0.41.

STRESSES IN THE SKIN ELEMENTS

Figure 8 shows the daily history of stresses in the skin element. The locations and the identification numbers of the strain gauges are shown on top of the figure. Gauges 1, 5, and 9 measured axial strain on the outside of the face; gauges 3, 7, and 11 measured axial strains on the inside. Gauges 2, 6, and 10 measured circumferential strain on the outside of the face; gauges 4, 8, and 12 measured circumferential strain on the inside. The actual deformation of the skin elements closely approximated the deformation assumed in developing Eqs. 3, 4, and 5. Accordingly, tensile circumferential stresses developed on the outside of the face, and compressive circumferential stresses developed on the inside. Deformations of the skin elements were measured at 5 gauge points on the faces of the skin plates with a specially designed vernier-micrometer caliper capable of accurately measuring to 0.001 in. The measured relationship between the vertical deformation of the skin plate and fill height is shown in Figure 9. Based on the vertical deformations observed in the field, the stresses in the skin plates were calculated for both hinged- and fixed-end conditions. A comparison of the measured and com-

Figure 5. Instrumentation sections.

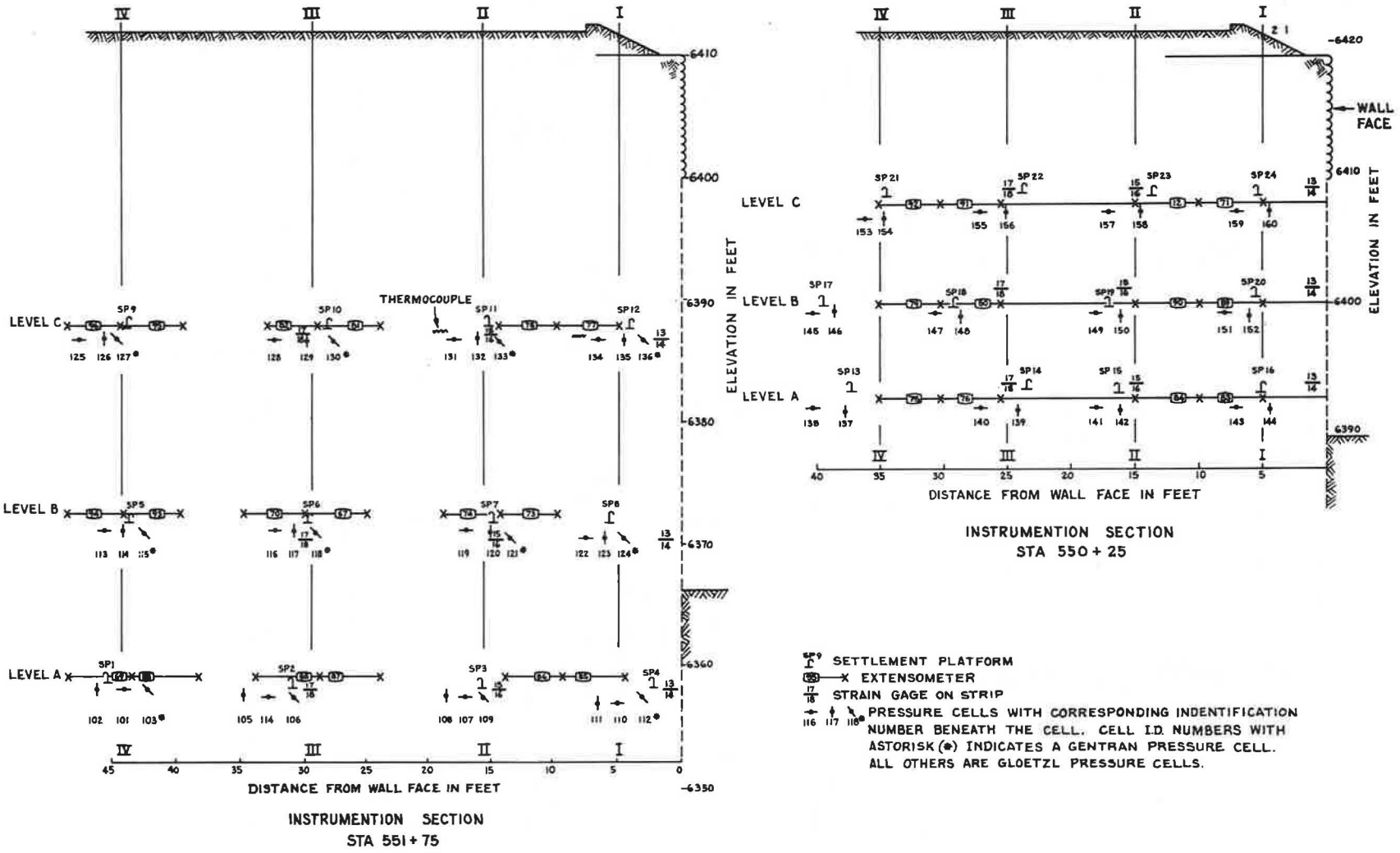

Figure 6. Daily history of stresses in steel strip.

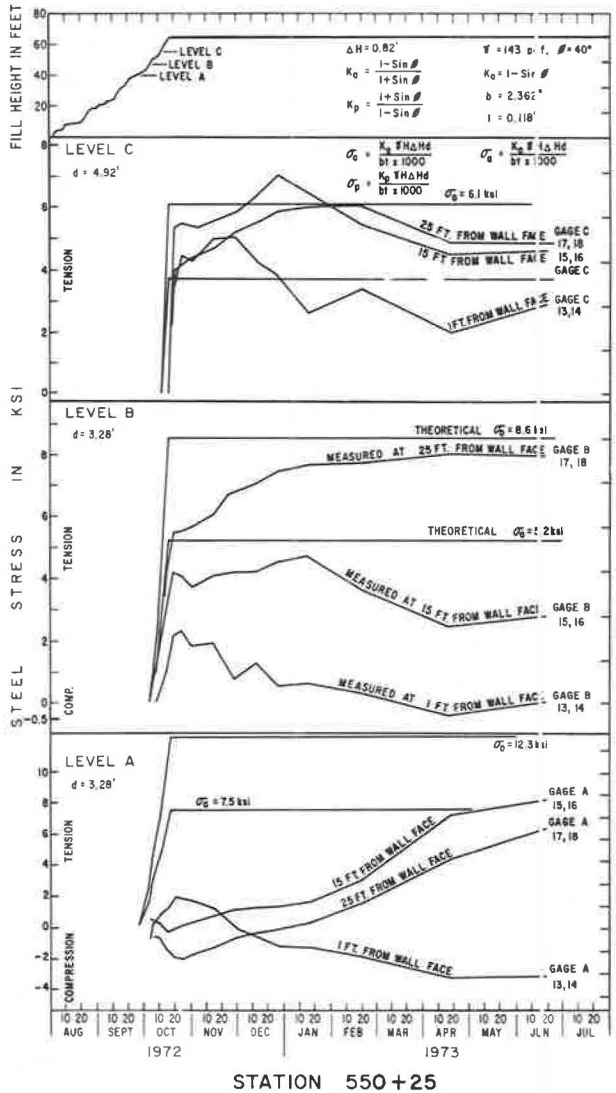

Figure 7. Daily history of soil stress.

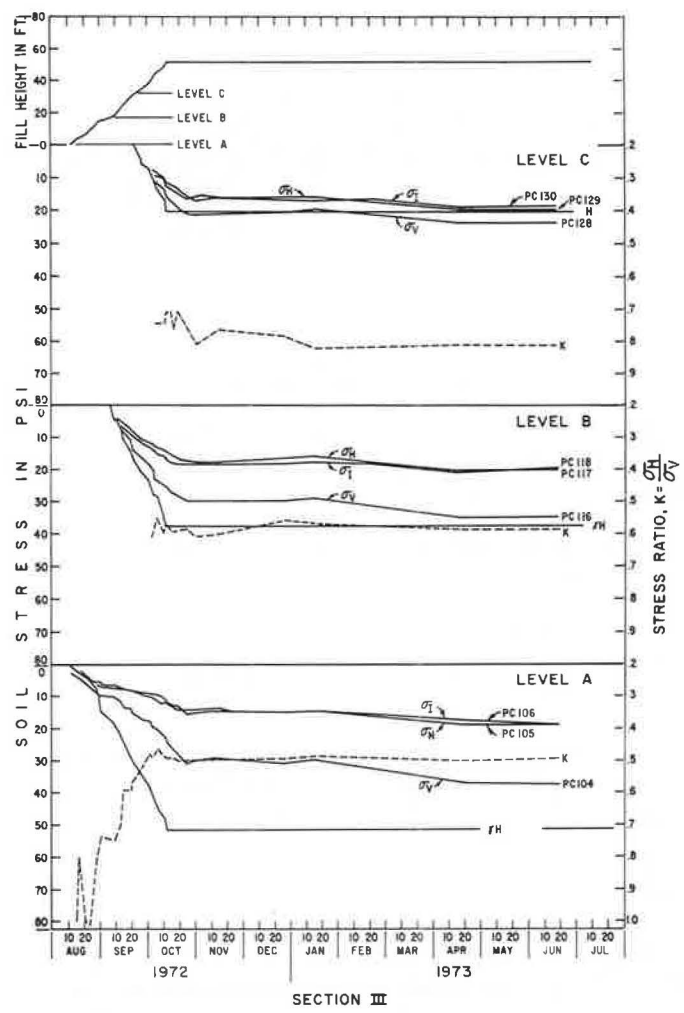

Figure 8. Daily history of stress in skin element.

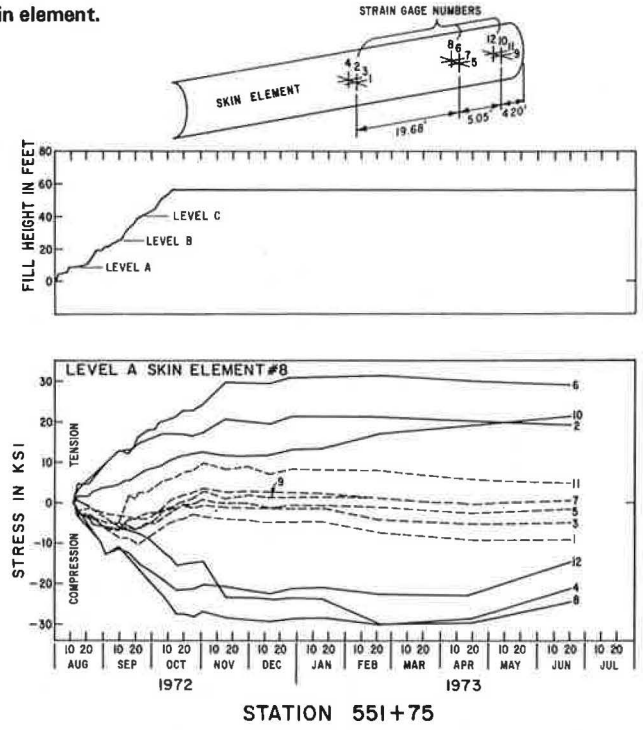

Figure 9. Field behavior of steel skin element.

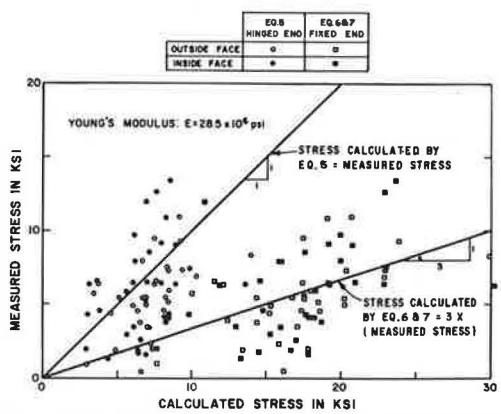

(a) COMPARISON OF MEASURED AND CALCULATED CIRCUMFERENTIAL STRESS AT SPRING LINE OF SKIN PLATE

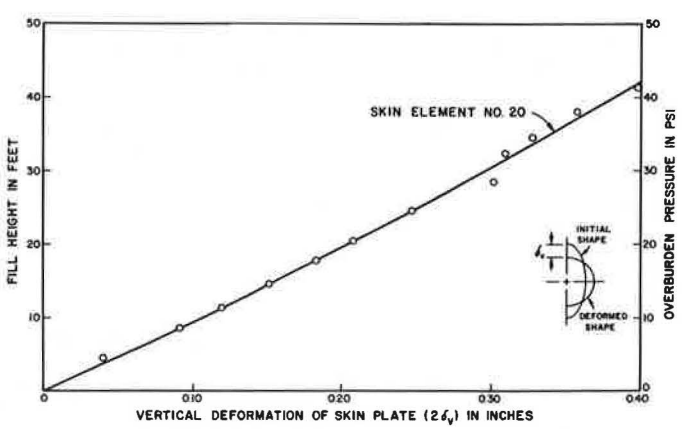

(b) RELATIONSHIP BETWEEN FILL HEIGHT AND SKIN PLATE DEFORMATION STATION 551+75

puted circumferential stresses also is shown in Figure 9. The calculated stresses based on hinged-end assumption (Eq. 5) agreed reasonably well with the measured data although the calculated stresses based on the fixed-end condition (Eqs. 6 and 7) were almost 3 times larger than those measured.

FIELD PULLING TESTS

To test the validity of Eqs. 3 and 4, dummy reinforcing strips were installed in the fill at 5 levels for field pulling tests. Three strips, 5, 10, and 15 ft in length, were embedded at each of 3 levels under overburden heights of 7.5, 12.4, and 18.2 ft. Three 23-ft strips were embedded at a depth of 18 ft; three 46-ft strips were embedded at a depth of 38 ft. One of the 23-ft strips and 1 of the 46-ft strips were instrumented with strain gauges on both top and bottom at 5-ft intervals.

A typical load deformation curve obtained from field pulling tests is shown in Figure 10 for a 5-ft strip. Three pulling loads were defined for analysis and indicated on the curves. These were

1. Yield loads representing the proportional limit of the load-deformation relationship,
2. Peak load representing the maximum pulling load, and
3. Residual load representing the pulling load when deformation increases appreciably without a change in the pulling load.

Figure 11 shows the relationships between the residual pulling load, overburden load, overburden height, and strip length. The skin-friction angles, ϕ_u, of 31 deg obtained from the residual pulling load plots agreed well with the laboratory test results at equal overburden pressure. For a constant overburden height, the residual loads were proportional to the overburden loads, which are the products of the overburden height, H; the unit weight, γ; the width of steel strip, b; and the length of the steel strip, L. Because γ, b, and H are constant under a given overburden height, the residual loads are proportional to the strip length. Because the peak load represents the maximum mobilized friction grip, it was used to calculate the factor of safety for the failure condition. The design tensile loads were calculated by using Eq. 1. The relationships between overburden height, H, strip length, L, and slipping factor of safety are shown in Figure 12. For a fill height of 10 ft, the minimum strip length may require only 9 ft for a factor of safety of 4. Figure 13 shows the relationship between peak pull load and the calculated skin-friction force (3). Peak pull loads exceeded the skin-friction force as the strip length exceeded 10 ft. We may conclude that strip length should be at least 10 ft.

AXIAL FORCES IN DUMMY STRIPS BECAUSE OF STATIC LOADING

Figure 14 shows the relationship between overburden loads and the maximum axial force observed in the 46-ft and the 23-ft strips at 10 to 15 ft from the wall face. The axial forces developed during construction were all lower than the calculated tensile force, T_a, from Eq. 1 based on the Rankine's active earth pressure coefficient, K_a. However, after the fill was completed the axial force continued to increase and the maximum axial force reached T_a in the 23-ft strip. In the 46-ft strip, the maximum axial force finally reached T_o, the calculated tensile force from Eq. 1, based on the at rest earth pressure coefficient, K_o. The continuous increase in tensile force after completion of the fill probably was due to the continuing settlement. At completion of construction and 8 months later, the settlements on levels B and C, station 551+75, varied from 1.5 to 2.5 ft. However, on level A, the settlement varied from 2.5 to 3.5 ft. Also, the face of the wall has moved a maximum of 0.7 ft horizontally downslope since completion of the fill. Both horizontal movement and settlement are attributed primarily to densification of the uncompacted slide debris.

SUMMARY AND CONCLUSIONS

The measured vertical soil stresses generally agreed with the calculated vertical earth pressures. The stress ratios, K, between the horizontal and vertical soil stresses

Figure 10. Typical load deformation curve.

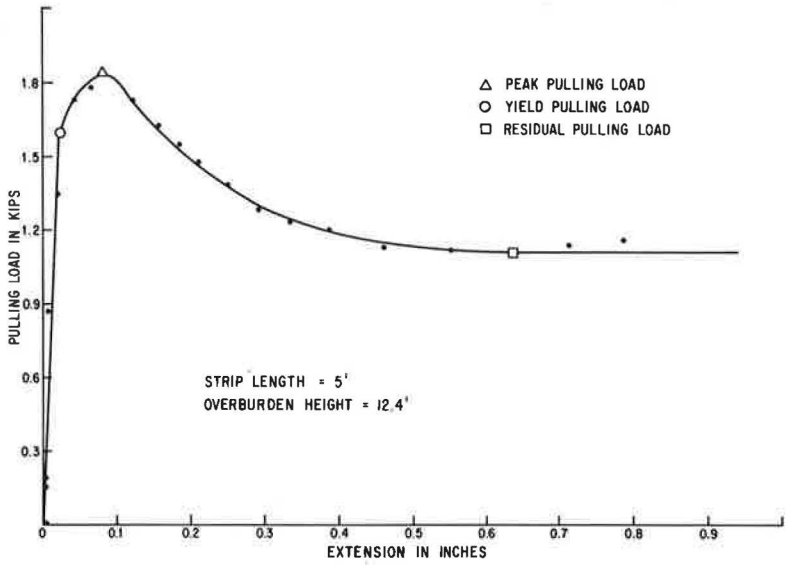

Figure 11. Residual pulling load, overburden load, overburden height, and strip length relationship.

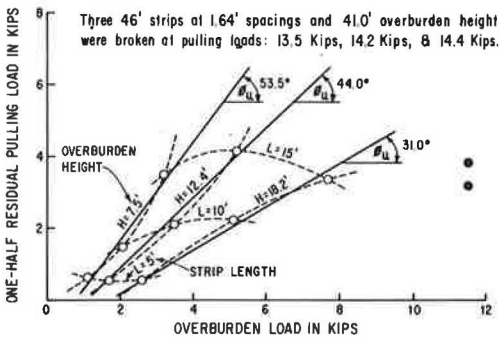

Figure 12. Overburden height, strip length, and slipping factor safety relationship.

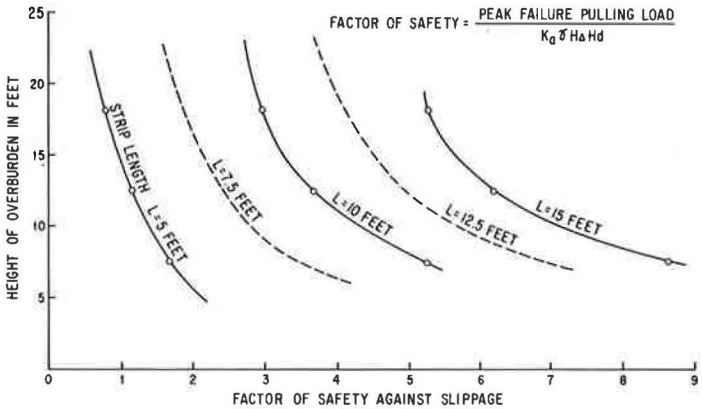

Figure 13. Relationship between pull load and skin-friction force.

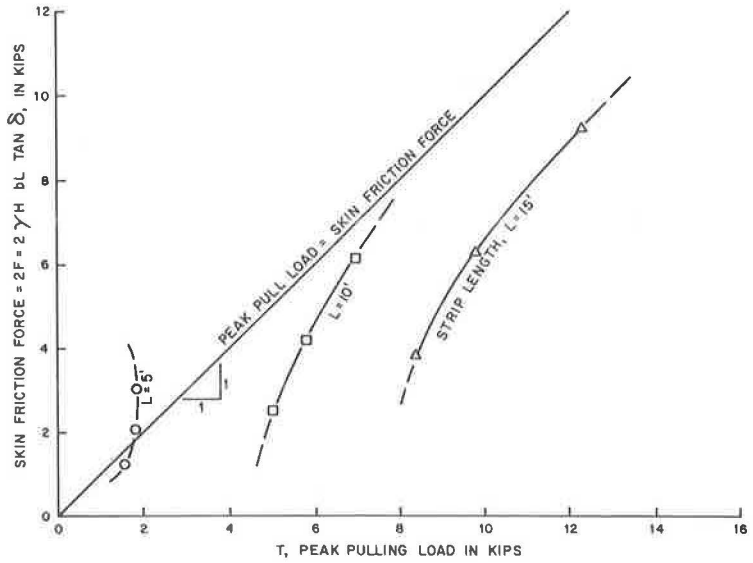

Figure 14. Relationship between overburden height and axial force in steel strip.

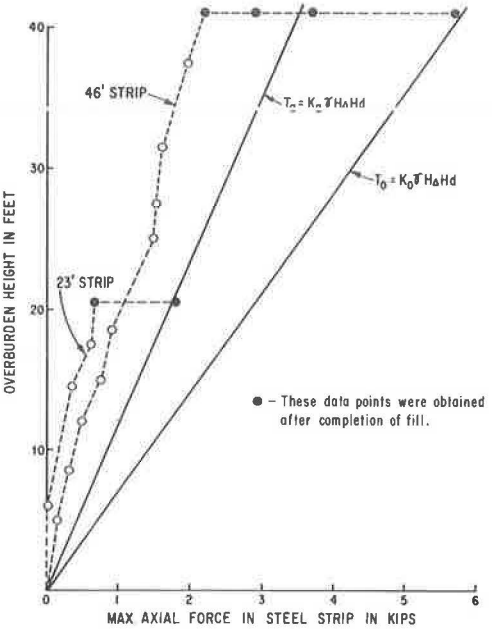

were highest during the early stages of construction and later decreased with large variations from point to point after completion of the fill.

The measured stresses in the steel strips near the wall face were generally smaller than, but approached, the calculated theoretical stresses, σ_a, based on Rankine's active stress condition. The highest steel stresses developed in the inner middle portion of the reinforced earth section. Steel stresses may increase to the values corresponding to theoretical at rest earth pressure. Equation 1, presented in this paper for the design of reinforcing strips, has been verified. The use of the active earth pressure coefficient, K_a, for calculating the steel stress is applicable for the end portion of the reinforcements. For the middle portion of the reinforcement, K_o should be used.

Field pulling test results indicated that the load-deformation curves resembled the stress-strain curves obtained from laboratory triaxial compression tests on dense sand when the strips were pulled loose. The yielding, peak, and residual load points were all defined clearly. The frictional forces developed on the steel strips were proportional to the overburden load for each overburden height. The field-measured skin-friction angle agreed well with the laboratory test results under equal overburden height. The relationships between the overburden height, strip length, and the factor of safety against slippage as shown in Figure 12 can be used for determining the minimum length of reinforcement for different overburden height, providing the requirement for stability is met. However, strip length should be at least 10 ft.

The structural behavior of the skin plates followed the hinged-end assumption in deformed shape and stress values. The vertical deformation of the skin plate, which is a measurement of settlement within each skin element, was proportional to the overburden height. Design Eq. 5, developed in this paper for design of the steel skin plate, accurately predicted the stresses developed in the skin plate. Use of the vertical deformation, δ_v, of the skin plate for one of the major functions in design has proven to be a satisfactory approach. Figure 9(b) can be used to estimate the vertical deformation, δ_v, for design of skin plate at different heights of reinforced earth fill. The assumption of a semicircular shape simplified the calculation of the stresses in the skin plate and accurately predicted the measured stresses.

The settlement and horizontal movement of the reinforced earth embankment was primarily attributable to the densification of the deep foundation slide debris. These movements were probably the main cause of continuing change in stresses of the steel and soil after completion of the fill.

ACKNOWLEDGMENTS

This paper presents the results of a federally financed research project. The writers wish to acknowledge and thank Gary Bork and John Kenan who were in charge of overall project design. The patience and cooperation of Robert F. Britton, who provided valuable assistance in installing the instrumentation during construction, also are gratefully acknowledged. This work was done under the HPR Work Program in cooperation with the Federal Highway Administration. The contents of this paper reflect the views of the authors, who are responsible for the facts and the accuracy of the data presented herein. The contents do not necessarily reflect the official views or policies of the State of California or the Federal Highway Administration.

REFERENCES

1. Duncan, W. Caesar. Vol. 1, Book 2, p. 201.
2. Vidal, H. The Principle of Reinforced Earth. Highway Research Record 282, 1969, pp. 1-16.
3. Chang, J. C., Forsyth, R. A., and Smith, T. W. Reinforced Earth Highway Embankment—Road 39. Highway Focus, Federal Highway Admin., Vol. 4, No. 1, Jan. 1972.
4. Chang, J. C., Durr, D. L., and Forsyth, R. A. Earthwork Reinforced Techniques. Transportation Lab., California Department of Transportation, TL No. 632115, Feb. 1974.

5. Seely, F. B., and Smith, J. O. Advanced Mechanics of Materials. John Wiley and Sons, Inc., New York, July 1962, pp. 421-437.
6. Jaky, J. Pressure in Silos. Proc. 1st Conf. on Soil Mech. and Found. Engineering, Rotterdam, 1948.

BEARING CAPACITY OF ANISOTROPIC AND NONHOMOGENEOUS CLAYS UNDER LONG FOOTINGS

M. Livneh and J. Greenstein, Technion—Israel Institute of Technology, Haifa, Israel

There is experimental evidence that saturated clays in undrained conditions have depth-dependent anisotropic strength properties. Hence there is a need for an appropriate strength law to determine the failure field for the medium in question. The critical bearing capacity of a footing in this medium was determined by a modified version of Hill's failure mechanism. According to this, in a nonhomogeneous medium where strength increases depth, failure takes place closer to the surface than it does according to Prandtl's mechanism. Anisotropy and nonhomogeneity must be taken into consideration in general.

•ANISOTROPIC or nonhomogeneous materials are the subject of numerous studies (1, 2, 3, 4, 5, 6, 7, 8). In engineering applications there is frequently a shear line along which the anisotropic strength is correlated (9, 10, 11, 12, 13). Livneh, Greenstein, and Shklarsky (14, 15, 16, 17) claim, however, that this approach is meaningless in an anisotropic medium and is thus inapplicable for practical purposes. The strength of saturated clay in undrained conditions is known to be anisotropic (2, 18) and to increase with depth (19). Therefore, to determine critical bearing capacity under long footings we have to formulate the strength law (yield function) and from it derive the field of failure (slip-line field) for the given medium. The notations used in the formulations in this paper are as follows:

c = cohesion,
c_o = surface value of cohesion,
$\bar{C}$ = material constant in Hill's model,
$D_1, D_{\pi/4}, D_2$ = material constants,
$D(\psi, x, y)$ = strength factor,
G = depth gradient of D,
f = yield function,
i, j = characteristic directions,
J_2 = second invariant of stress deviator,
k = material constant,
N_c = critical bearing-capacity factor,
p = mean stress in plane,
q = critical bearing capacity,
u, v = axial velocity components,
x, y = coordinate system in plane,
λ_y, n_λ = anisotropic functions,
ξ = angle between x and major principal strain-rate directions,
σ_1, σ_3 = principal components of stress tensor,
$\sigma_x, \sigma_y, \tau_{xy}$ = components of stress tensor in (x, y) plane, and
ψ = angle between x and major principal stress directions.

Publication of this paper sponsored by Committee on Foundations of Bridges and Other Structures.

YIELD FUNCTION

The principal mechanical property of a cohesive 2-dimensional medium such as the clay described previously is a yield function independent of the mean stress whose general form is

$$f = J_2^{1/2} - D = 0 \tag{1}$$

where D = strength factor, which is D (ψ, x, y). D also equals the radius of the Mohr circle at failure; in an anisotropic medium it is not identical with cohesion (14, 15, 16, 20). That is to say,

$$J_2 = \tfrac{1}{2}S_{ij}S_{ij} = \left(\frac{\sigma_1 - \sigma_3}{2}\right)^2 = \frac{(\sigma_x - \sigma_y)^2}{4} + \tau_{xy}^2 \tag{2}$$

For a homogeneous medium, the yield function reduces to a model such as that proposed by Hill (21) or Davis and Christian (2).

In this study, we present for practical purposes the following pattern for D:

$$D = D(\psi)_{y=0} + Gy \tag{3}$$

where

ψ = angle (positive counterclockwise) between x and σ_1 directions (Fig. 1), and
G = $\partial D/2y$, the depth gradient of D (Fig. 2).

The first term in Eq. 3 represents the surface variation (y = 0), as follows:

$$D(\psi)_{y=0} = D_1 - \left(D_1 - D_{\pi/4} + \frac{D_2 - D_1}{2^k}\right)\sin^{2k}2\psi + (D_2 - D_1)\sin^{2k}\psi \tag{4}$$

where

D_1, $D_{\pi/4}$, and D_2 = ψ = 0, $\pi/4$, and $\pi/2$ respectively [Fig. 3 (2)], and
k = material constant.

This paper deals with cases of constant G (19).

FIELD OF FAILURE IN ANISOTROPIC INHOMOGENEOUS CLAY

To determine the stress field in an anisotropic clay medium, the components of the stress tensor at failure should be formulated as follows:

$$\sigma_{x,y} = p \pm D\cos2\psi$$
$$\tau_{xy} = D\sin2\psi \tag{5}$$

When Eq. 5 is substituted, the equilibrium equations read:

$$\frac{\partial p}{\partial x} + 2D(-\sin2\psi + n_o\cos2\psi)\frac{\partial \psi}{\partial x} + 2D(n_o\sin2\psi + \cos2\psi)\frac{\partial \psi}{\partial y} + G\sin2\psi = 0 \tag{6}$$

$$\frac{\partial p}{\partial y} + 2D(n_o\sin2\psi + \cos2\psi)\frac{\partial \psi}{\partial x} + 2D(\sin2\psi - n_o\cos2\psi)\frac{\partial \psi}{\partial y} - G\cos2\psi = 0 \tag{7}$$

where

$$n_o = \frac{\dfrac{\partial D}{\partial \psi}}{2D} = \tfrac{1}{2}\frac{\partial}{\partial \psi}\ln[D(\psi)_{y=0} + Gy] \tag{8}$$

Figure 1. Description of the coordinate system.

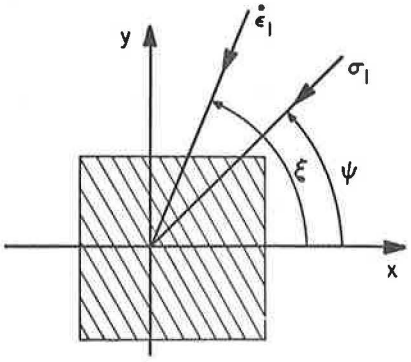

Figure 2. Variation of the strength factor, D, with depth.

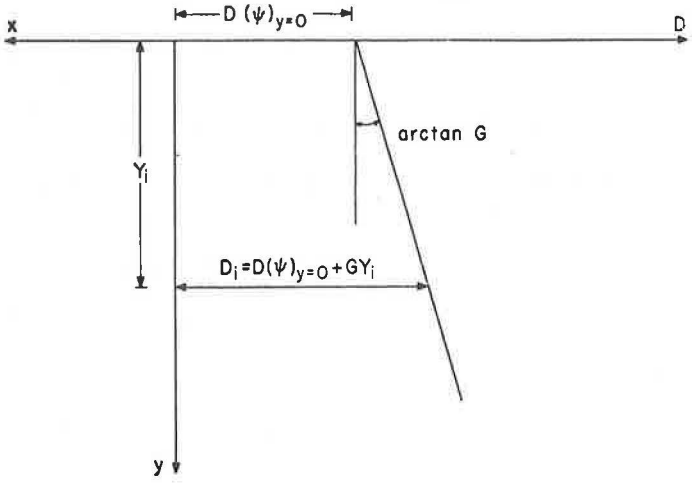

Figure 3. Anisotropic strength properties of clay.

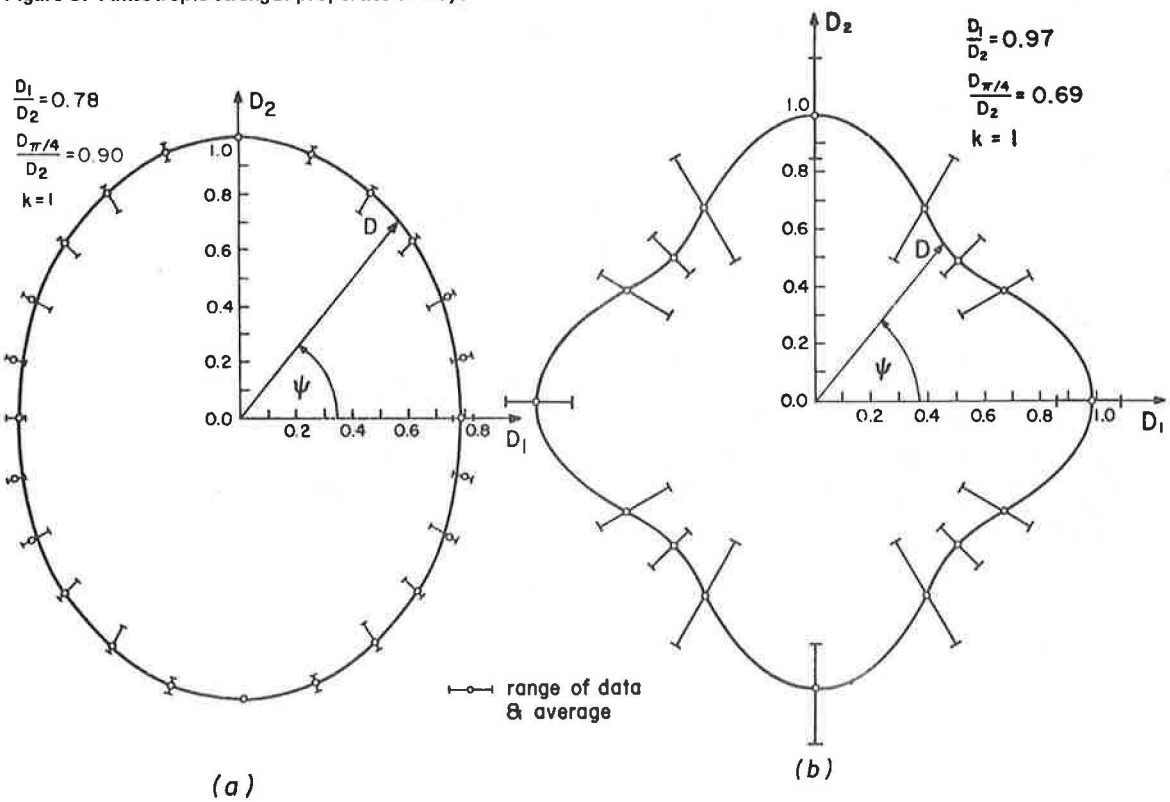

This is not exclusive for a strength factor that obeys Eq. 4, but it is valid for any plausible continuous pattern, such as Hill's or Davis' models. Equations 7 and 8 are hyperbolic and yield

$$\begin{vmatrix} 1 & 0 & 2D(-\sin 2\psi + n_o \cos 2\psi) & 2D(n_o \sin 2\psi + \cos 2\psi) \\ 0 & 1 & 2D(n_o \sin 2\psi + \cos 2\psi) & 2D(\sin 2\psi - n_o \cos 2\psi) \\ dx & dy & 0 & 0 \\ 0 & 0 & dx & dy \end{vmatrix} = 0 \qquad (9)$$

which in turn has 2 roots

$$\frac{dy}{dx} = \frac{\sin 2\psi - n_o \cos 2\psi \pm \sqrt{1 + n_o^2}}{\cos 2\psi + n_o \sin 2\psi} = y'_{i,j} \qquad (10)$$

which represent the slopes of the characteristic lines in the stress field. These lines, in the anisotropic-inhomogeneous cohesive media, meet at right angles.

The compatibility equations of the stress field that are satisfied along characteristic lines are as follows:

$$dp + \bar{\lambda}_y d\psi + G(\sin 2\psi - \cos 2\psi\, y'_i)dx = 0 \qquad \text{along i line} \qquad (11)$$

$$dp - \bar{\lambda}_y d\psi + G(\sin 2\psi - \cos 2\psi\, y'_j)dx = 0 \qquad \text{along j line} \qquad (12)$$

where

$$\bar{\lambda}_y = 2[D(\psi)_{y=0} + Gy]\sqrt{1 + n_o^2} \qquad (13)$$

Equations 11 and 12 are the equilibrium equations and reduce to those of Hill and Davis for their particular models in a homogeneous medium and to those of Hencky in an isotropic-homogeneous one, where D represents cohesion.

The stress field is identical with the velocity characteristics of the following model, which represents the particular case of displacement under plastic deformation:

$$\frac{\partial u}{\partial x} + \frac{\partial v}{\partial y} = 0 \qquad (14)$$

$$\cot 2\,\xi = \frac{\dfrac{\partial u}{\partial x} - \dfrac{\partial v}{\partial y}}{\dfrac{\partial u}{\partial y} + \dfrac{\partial v}{\partial x}} = \frac{1 + n_o \tan 2\psi}{\tan 2\psi - n_o} \qquad (15)$$

where

u and v = axial velocity components, and
ξ = the angle (positive counterclockwise) between the x and major principal strain-rate directions.

Equation 14 indicates that the plastic deformation involves no change of volume; Eq. 15 indicates that in an anisotropic medium, the directions of the principal stresses and strain rates are not coincidental. Such is the case, for example, with Hill's model (21), for which Eq. 15 reduces to

$$\tan 2\,\xi = (1 - \bar{C}) \tan 2\,\psi \qquad (16)$$

In an isotropic medium ($n_o = 0$), $\psi = \xi$, and the directions coincide.

BEARING CAPACITY OF FOOTING IN ANISOTROPIC, NONHOMOGENEOUS CLAY MEDIUM

Figure 4 shows that the case in question is symmetric, and that along the edge in fields 1 and 2, $\psi = 0$ and $\pi/2$ respectively; for both of which, $\partial D/\partial\psi = 0$ (D obeys Eq. 4). Hence, in these zones, $n_o = 0$, and the compatibility Eqs. 11 and 12 reduce to

$$dp - G\cos 2\psi\, y'_{i,j}\, dx = 0 \qquad \text{along i, j line} \tag{17}$$

If we substitute $y'_{i,j}$, we have

$$dp \pm G dx = 0 \qquad \text{along i, j line} \tag{18}$$

Equation 10 shows that along the edge in fields 1 and 2 $y'_1 = -y'_j$ ($dx_i = -dx_j$). Accordingly, in the symmetric case with a constant mean stress, the compatibility equations are satisfied by straight lines. In other words, in an anisotropic, nonhomogeneous medium when D increases only vertically, each failure field consists of 2 families of straight lines that meet at right angles.

In the homogeneous and weightless case (anisotropic or isotropic), the critical bearing capacity according to Hill is identical with its Prandtl counterpart. However, for the case under discussion in this paper, when D increases with depth, the critical bearing capacity according to Hill is lower. This could be expected because the material undergoes shear closer to the surface. By symmetry, point E in Figure 4 must be the midspan of the footing; this agrees with Hill's mechanism. The assumption for the fan-shaped field 3 is that it is rigid and that the shear line j (BC in Fig. 4) is circular. This assumption signifies that the characteristic line i passes through the singularity S (along BC, the j line, $y'_i = y/x$). In these circumstances it can be shown that the following set of equations is satisfied along the j line:

$$\left.\begin{aligned} \frac{dx}{d\psi} &= x\frac{\frac{dy'_i}{d\psi}}{y'_j - y'_i} \\ \frac{dy}{d\psi} &= xy'_j\frac{\frac{dy'_i}{d\psi}}{y'_j - y'_i} \\ \frac{dp}{d\psi} &= \bar{\lambda}_y - G(\sin 2\psi - \cos 2\psi\, y'_j)\frac{dx}{d\psi} \end{aligned}\right\} \tag{19}$$

Equation 14 was shown by Ince (22) to have a unique solution for given initial conditions, in this case, for point A—$\overline{p_A} = D_1$, $y_A = 0$, $x_A = B/2$, and $\psi_A = 0$. This solution represents an approximate upper bound for the critical bearing capacity as follows:

$$N_c = \frac{q}{D_2} = \frac{q}{D_E} = \frac{p_E}{D_2} + 1 \tag{20}$$

where D_E and p_E refer to point E, at which $\psi = \pi/2$.

Figure 5 shows N_c plotted against D_1/D_2 [with $(G/D_2)(B/10)$ and $D_{\pi/4}/D_2$ as parameters] where the dimension of B is identical to that of D_2/G. For the total error because of noninclusion of the anisotropy and nonhomogeneity, it is seen that when $D_1/D_2 = 1.25$, $D_{\pi/4}/D_2 = 1.0$, and $(G/D_2)(B/10) = 0.1$, the exact value is about 50 percent higher than its isotropic counterpart, $N_c = \pi + 2$. The comparison refers to an undisturbed surface sample tested under routine laboratory conditions ($\psi = \pi/2$). In certain circumstances, 1 component of the error cancels the other out, in which case [$(G/D_2)(B/10) = 0.05$, $D_1/D_2 = 0.6$, and $D_{\pi/4}/D_2 = 0.75$] the isotropic value may be used.

In an isotropic medium where $c = c_o + Gy$, the compatibility Eqs. 11 and 12 reduce to

Figure 4. Rupture mechanism for bearing capacity determination.

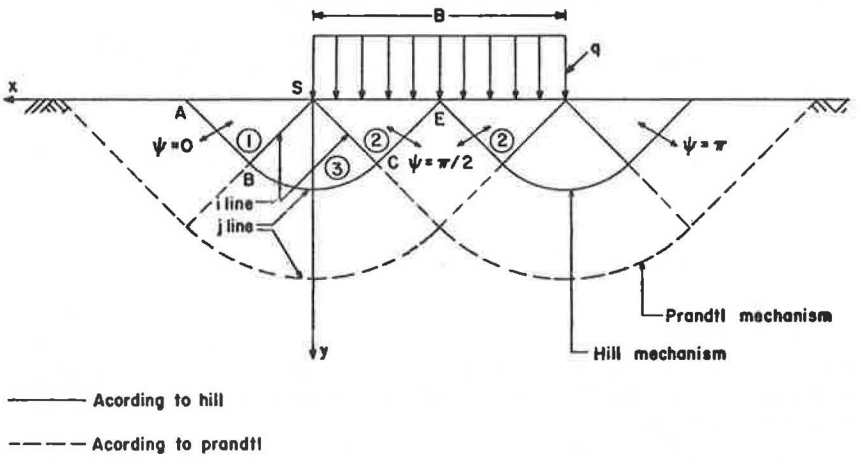

Figure 5. Effect of anisotropy and nonhomogeneity on N_c.

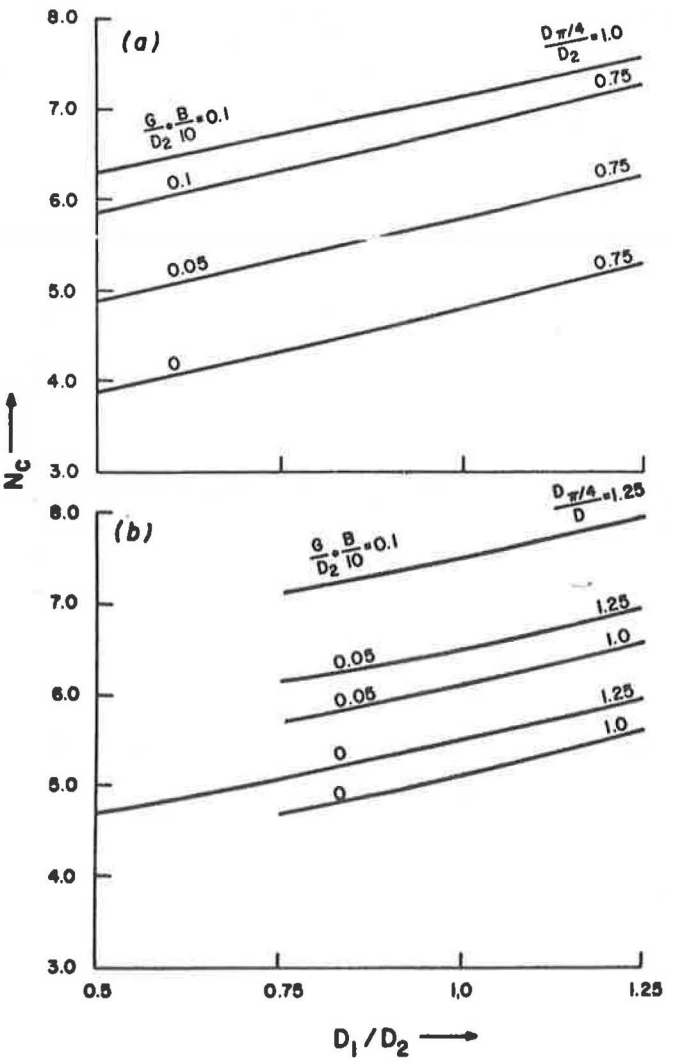

$$dp + 2cd\psi - Gdx = 0 \quad \text{along i line}$$
$$dp + 2cd\psi + Gdx = 0 \quad \text{along j line} \tag{21}$$

According to Livneh and Greenstein (23), integration of the above yields the upper bound

$$q = (\pi + 2)\, c_{0.4B} \tag{22}$$

where $c_{0.4B}$ = cohesion at depth y = 0.4B.

CONCLUSIONS

In an anisotropic medium where the strength factor D increases with depth (as in the symmetric problem in Fig. 4), there are 2 fields of failure consisting of straight lines that meet at right angles.

Critical bearing capacity is determined by Hill's failure mechanism, as modified, in which the material is sheared closer to the surface than in Prandtl's model. Critical bearing capacity N_c is determined from a set of equations with a unique solution for given initial conditions, namely $P_A = D_1$, $Y_A = 0$, and $x_A = B/2$ (Fig. 4).

Anisotropy and nonhomogeneity may sometimes have a considerable effect on N_c compared to the isotropic value, $\pi + 2$, although in certain cases their contributions may cancel each other out. In an isotropic medium ($n_o = 0$) with depth-dependent strength, critical bearing capacity is obtained by multiplying the cohesion at depth 0.4B by the isotropic N_c.

REFERENCES

1. Baker, W. H., and Krizek, R. J. Mohr-Coulomb Strength Theory for Anisotropic Soils. Jour. Soil Mech. and Found. Div., Proc. ASCE, Vol. 96, No. SM1, 1970, pp. 269-291.
2. Davis, E. H., and Christian, J. T. Bearing Capacity of Anisotropic Cohesive Soil. Jour. Soil Mech. and Found. Div., Proc. ASCE, Vol. 97, No. SM5, 1971, pp. 753-769.
3. Davis, E. H., and Booker, J. R. The Effect of Increasing Strength With Depth in the Bearing Capacity of Clays. Univ. of Sydney, Australia, Res. Rept. R175, 1971.
4. Delory, F. A., and Lai, H. N. Variation in Undrained Shearing Strength by Semi-confined Tests. Canadian Geotech. Jour. 8, 1971, pp. 538-545.
5. Duncan, J. M., and Seed, H. B. Anisotropy and Stress Reorientation in Clay. Jour. Soil Mech. and Found. Div., Proc. ASCE, Vol. 92, No. SM5, 1966, pp. 21-50.
6. Duncan, J. M., and Seed, H. B. Strength Variations Along Failure Surfaces in Clay. Jour. Soil Mech. and Found. Div., Proc. ASCE, Vol. 92, No. SM6, 1966, pp. 81-104.
7. Kowalczyk, U. Indentation Problem of a Semi-Infinite Transversally Non-Homogeneous Body Acted on by a Rigid Punch. Bull. de L'Académie Polonaise de Sciences, Vol. 13, No. 4, 1965, pp. 193-200.
8. Sobotka, Z. The Limiting Equilibrium of Non-Homogeneous Soils. Proc. Internat. Union of Theoretical and Applied Mechanics, Pergamon Press, New York, 1959, pp. 227-240.
9. Button, S. J. The Bearing Capacity of Footings on a Two-Layer Cohesive Sub-Soil. Proc. 3rd Internat. Conf. Soil Mech. and Found. Engineering, Vol. 1, 1953, pp. 332-335.
10. James, C. H. C., Krizek, R. J., and Baker, W. H. Bearing Capacity of Purely Cohesive Soils With a Nonhomogeneous Strength Distribution. Highway Research Record 282, 1969, pp. 48-56.
11. Reddy, A. S., and Srinivasan, R. J. Bearing Capacity of Footings on Layered Clays. Jour. Soil Mech. and Found. Div., Proc. ASCE, Vol. 93, No. SM2, 1967, pp. 83-99.

12. Reddy, A. S., and Srinivasan, R. J. Bearing Capacity of Footings on Clays. Soils and Foundations, Japanese Society of Soil Mech. and Found. Engineering, Vol. 11, No. 3, 1971, pp. 51-64.
13. Reddy, A. S., and Srinivasan, R. J. Bearing Capacity of Deep Foundations in Saturated Clays. Soils and Foundations, Japanese Society of Soil Mech. and Found. Engineering, Vol. 11, No. 4, 1971, pp. 1-4.
14. Livneh, M., Greenstein, J., and Shklarsky, E. Discussion of "Bearing Capacity of Footings on Anisotropic Soils." Jour. Soil Mech. and Found. Div., Proc. ASCE, Vol. 97, No. SM10, 1971, pp. 1491-1493.
15. Livneh, M., and Greenstein, J. State of Failure Stress in a Medium With Anisotropic Cohesion and Isotropic Internal Friction Angle. Israel Jour. of Tech., Vol. 9, No. 5, 1971, pp. 411-425.
16. Livneh, M., and Greenstein, J. Discussion of "Bearing Capacity of Anisotropic Cohesive Clays." Jour. Soil Mech. and Found. Div., Proc. ASCE, Vol. 98, No. SM2, 1972, pp. 232-234.
17. Livneh, M., and Greenstein, J. Discussion of "Bearing Capacity of Deep Foundations in Saturated Clays." Soils and Foundations, Japanese Society of Soil Mech. and Found. Engineering, Vol. 12, No. 4, 1972, pp. 82-83.
18. Lo, K. Y. Stability of Slopes in Anisotropic Soils. Jour. Soil Mech. and Found. Div., Proc. ASCE, Vol. 91, No. SM4, Proc. Paper 4405, 1965, pp. 85-106.
19. Insley, A. A Deep Excavation and a Raft Foundation in Soft Clay. Canadian Geotech. Jour., Vol. 9, No. 3, 1972, pp. 237-248.
20. Greenstein, J. The Effect of Anisotropy of Asphaltic Mixtures on Their Bearing Capacity. Technion—Israel Inst. Tech., DSc thesis, 1973.
21. Hill, R. The Mathematical Theory of Plasticity. Clarendon Press, Oxford Univ., England, Chapter 12, 1950.
22. Ince, E. L. Ordinary Differential Equations. Dover Publications, Inc., New York, 1953.
23. Livneh, M., and Greenstein, J. The Bearing Capacity of Footings on Nonhomogeneous Clays. Proc. 8th Internat. Conf. Soil Mech. and Found. Engineering, Moscow, 1973.
24. Sreenivasulu, V., and Ranganathan, B. V. Bearing Capacity of an Anisotropic Non-Homogeneous Medium Under $\phi = 0$ Condition. Soils and Foundations, Japanese Society of Soil Mech. and Found. Engineering, Vol. 11, No. 3, 1971, pp. 17-27.

BEHAVIOR OF BEAMS ON RANDOMLY NONHOMOGENEOUS BASES

Raymond J. Krizek, Technological Institute, Northwestern University; and
Eduardo E. Alonso, Soil Mechanics Laboratory, McGill University

The behavior of infinite beams resting on randomly nonhomogeneous bases is analyzed within the framework of random function theory. The coefficient of soil reaction is described as a random function of the spatial coordinate, and a linearization procedure is used to derive the necessary functional relationship in terms of an impulsive load. Once the spectral structure of the solution is constructed, a convenient form for the variance of the settlement is found. This method is applied for 3 basic types of load, including a concentrated load, a concentrated moment, and a uniformly distributed load over a finite length of beam. In all cases a particular family of autocorrelation functions for the coefficient of soil reaction is used to evaluate the influence of the different parameters. Solutions are presented in the form of graphs that give the variance of the settlement at different locations along the beam. Finally, these results are applied to a particular case involving randomness in both total and differential settlement of an infinite beam that is uniformly loaded over a finite length.

•THE WINKLER theory, which states that the reaction forces against the foundation are proportional at every point to the deflection of the structure at that point, commonly is used to characterize the foundation medium when the deformational behavior of 1- or 2-dimensional structures resting on soil is dealt with. This theory's main attraction is its mathematical simplicity. The deflection of a beam resting on such a base is governed by a fourth-order linear differential equation with constant coefficients; this equation is readily solvable for a variety of loads, geometrical configurations, and boundary conditions. As shown in Figure 1, this theory yields suitable results when an appropriate choice for the constant of proportionality between force and deflection is made. This figure also illustrates the main problem to be addressed in this paper—whether the degree of variability of the beam behavior can be predicted from a probabilistic definition of the soil parameter and whether probability statements rather than a deterministic estimate can be made concerning the predicted behavior of the beam. Figure 1 shows that, even though the predicted curves closely resemble the measured curves in the mean, significant deviations can be found at some locations.

In most engineering applications, a close prediction of mean values is sufficient; attempts to make more accurate predictions do not seem justified. However, the strict limitations imposed on the differential settlement in delicate structures such as particle accelerators or high-speed transportation systems require more refined solutions. The complex nonhomogeneous character of natural and man-made soils indicates the advantages of a probabilistic approach to the problem. The random problem based on Winkler's hypothesis will be formulated and additional restrictions will be explained; then, the method of solution for the infinite beam will be developed for 3 basic loads and the variance of the beam settlement will be presented in terms of dimensionless parameters. These parameters provide all the information that is required to handle

Publication of this paper sponsored by Committee on Mechanics of Earth Masses and Layered Systems.

Figure 1. Deflections and stresses in a rail.

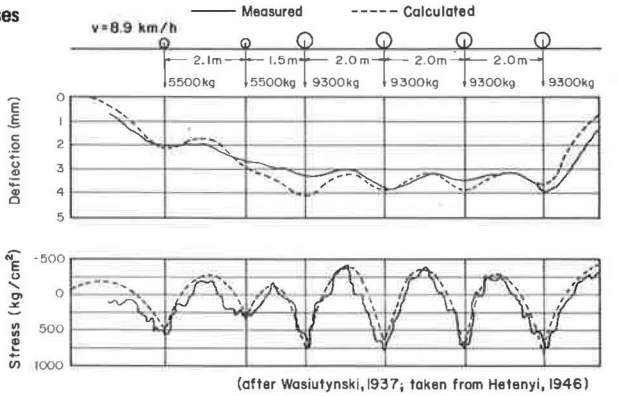

Figure 2. Random problem.

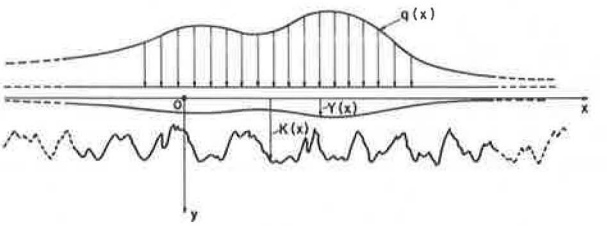

Figure 3. Modified random problem.

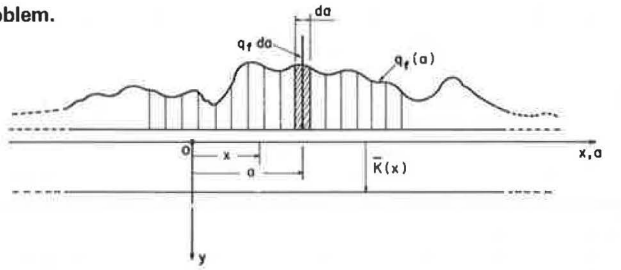

Figure 4. Settlement frequency response function.

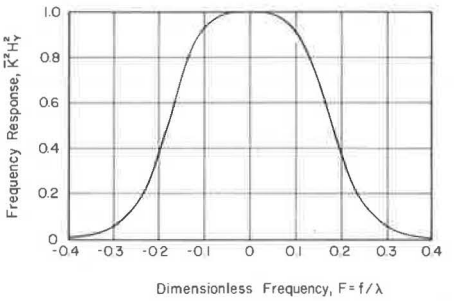

Figure 5. Settlement spectrum versus frequency for concentrated load.

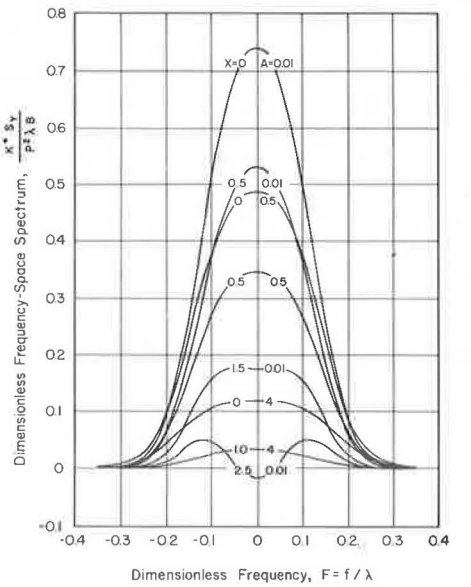

a broad class of problems because, if the probability distribution of the soil coefficient is normal, the probabilistic answer to the problem becomes completely characterized by the variance of the settlement.

FORMULATION OF THE PROBLEM

Within the framework of classical strength of materials applied to prismatic beams, the equilibrium of a differential element of a prismatic beam resting on a Winkler base [defined by its variable coefficient of soil reaction, k(x)] and arbitrarily loaded by q(x) leads to the following ordinary differential equation for the deflection of the beam, y(x):

$$q(x) = EI \frac{d^4y}{dx^4} + k(x)y(x) \tag{1}$$

where

E = modulus of elasticity of the beam material, and
I = moment of inertia of the cross section of the beam.

Figure 2 shows the problem and shows the reference axis. Note that, although the coefficient k is represented as having a continuous dependence on x, such continuity is not assumed in this simplified medium; in fact, the common representation of a beam resting on a number of independent springs better illustrates the situation analyzed in this study. Thus, the "transmission" of deformation through the soil is guaranteed only by continuity of the beam.

If k(x) in Eq. 1 is considered to be a random function, K(x), of the spatial parameter, x, which defines the longitudinal coordinate of points along the beam, then Eq. 1 becomes a random ordinary differential equation with random coefficients as follows:

$$q(x) = EI \frac{d^4Y(x)}{dx^4} + K(x)Y(x) \tag{2}$$

where capital letters denote random functions. Without losing generality, K(x) and Y(x) can be resolved into their mean values, $\overline{K}(x)$ and $\overline{Y}(x)$, and centered random functions, $K^*(x)$ and $Y^*(x)$, as follows:

$$K(x) = \overline{K}(x) + K^*(x) \tag{3}$$

$$Y(x) = \overline{Y}(x) + Y^*(x) \tag{4}$$

Upon introduction of these expressions into Eq. 2, we get

$$q(x) = EI \frac{d^4\overline{Y}(x)}{dx^4} + EI \frac{d^4Y^*(x)}{dx^4} + \overline{K}(x)\overline{Y}(x) + \overline{K}(x)Y^*(x) + K^*(x)\overline{Y}(x) + K^*(x)Y^*(x) \tag{5}$$

which is nonlinear in its random terms. This nonlinearity poses mathematical difficulties in obtaining a solution. If stiff or homogeneous soil conditions allow $K^*(x)$ and $Y^*(x)$ to be small when compared to the mean values, $\overline{K}(x)$ and $\overline{Y}(x)$, Eq. 5 can be simplified to

$$q(x) = EI \frac{d^4\overline{Y}(x)}{dx^4} + EI \frac{d^4Y^*(x)}{dx^4} + \overline{K}(x)\overline{Y}(x) + \overline{K}(x)Y^*(x) + K^*(x)\overline{Y}(x) \tag{6}$$

Consider now the action of the expectation operator on Eq. 6; taking into account the interchangeability of the mathematical expectation operator and a linear differential operator, we can write

$$q(x) = EI\frac{d^4\overline{Y}(x)}{dx^4} + EI\frac{d^4\{E[Y^*(x)]\}}{dx^4} + \overline{K}(x)\overline{Y}(x) + \overline{K}(x)E[Y^*(x)] + \overline{Y}(x)E[K^*(x)] \quad (7)$$

By definition the expected values of $Y^*(x)$ and $K^*(x)$ are zero, and Eq. 7 reduces to

$$q(x) = EI\frac{d^4\overline{Y}(x)}{dx^4} + \overline{K}(x)\overline{Y}(x) \quad (8)$$

which is the usual deterministic equation for the mean deflection of a beam; however, Eq. 8 is valid from a probabilistic point of view provided the values of the mean centered coefficient of subgrade reaction are small when compared to the mean value. If Eq. 8 is combined with Eq. 6, then the random differential equation governing the deflection of the beam is simplified to

$$-K^*(x)\overline{Y}(x) = EI\frac{d^4Y^*(x)}{dx^4} + \overline{K}(x)Y^*(x) \quad (9)$$

In this equation randomness is introduced through a fictitious random load term that accounts for the actual load in an indirect way, namely, through the deformation $\overline{Y}(x)$ that it produces in the mean problem of Eq. 8. Note that, even if the process describing the coefficient of subgrade reaction is considered homogeneous in the stochastic sense (the case considered herein), the random load term of Eq. 9 is a nonhomogeneous process because of the modulation provided by the function $\overline{Y}(x)$.

METHOD OF SOLUTION

To obtain the solution for the case of an infinite beam, one may rewrite Eq. 9 as follows:

$$q_f(x) = EI\frac{d^4Y(x)}{dx^4} + \overline{K}(x)\overline{Y}(x) \quad (10)$$

$$q_f(x) = -\overline{Y}(x)K(x) \quad (11)$$

where

$Y(x)$ and $K(x)$ = mean centered values, and
$q_f(x)$ = random (fictitious) load.

The objective in this problem is to determine the variance of the beam settlement, specifically, that settlement that is consistent with the definition of the subgrade coefficient. Because we are dealing with mean centered functions, the variance is directly the mean square value. When the solution for an impulsive type of load is known, the solution to Eq. 10 is constructed by superposition; if the solution for a unit concentrated load located at point a in Figure 3 can be obtained, then the deflection at any point x can be written as follows:

$$Y(x) = \int_{-\infty}^{\infty} h_v(x, a)q_f(a)da \quad (12)$$

where $h_v(x, a)$ = settlement at point x due to a unit load at point a. This superposition method is justified by the linearity of the governing field equation. For an infinite beam the influence factor, $h_v(x, a)$, is only a function of the difference x - a if a convenient location for the reference system is chosen. Based on Eq. 12 the autocorrelation function of the settlement, Y, can be written formally as follows:

$$R_Y(x_1, x_2) = E[Y(x_1)Y(x_2)]$$

$$= E\left[\int_{-\infty}^{\infty}\int_{-\infty}^{\infty} h_Y(x_1 - a)h_Y(x_2 - b)q_f(a)q_f(b)dadb\right] \tag{13}$$

After a number of well-known transformations (2) occur, the Wiener-Khintchine relation can be established as follows:

$$S_Y(f_1, f_2) = H_Y^*(f_1)H_Y(f_2)S_{q_f}(f_1, f_2) \tag{14}$$

where

$S_Y(f_1, f_2)$ and S_{q_f} = double frequency power spectra density functions (generalized spectral density functions) of the settlement and the fictitious load, q_f, respectively,
$H_Y(f)$ = frequency response function of the system governed by Eq. 10, and
$H^*(f)$ = the complex conjugate, $H(f)$.

The relationship given by Eq. 14 is a general expression for the spectral structure of the "output" of a linear system when a nonhomogeneous process is the "input". When the expression for the power spectra is found, the nonhomogeneous autocorrelation function for Y and the particular case of its mean square value is obtained by a double inverse Fourier transform of the power spectra density function. However, the special structure of the random load, q_f, as a product of a known deterministic function, $\overline{Y}(x)$, and a zero-mean homogeneous random function, $K^*(x)$, introduces convenient simplifications. In fact, if we define an instantaneous power spectra function of the fictitious load (frequency-space spectra function) as follows:

$$S_{q_f}(f, x) = \int_{-\infty}^{\infty} R_{q_f}(\tau, x)e^{-i2\pi f\tau}d\tau \tag{15}$$

where x and $\tau = \frac{1}{2}(x_1 + x_2)$ and $\frac{1}{2}(x_2 - x_1)$ respectively, which define 2 points with coordinates x_1 and x_2, and $r_{q_f}(\tau, x)$ = autocorrelation function of $q_f(x)$, then the following relationship, as shown by Alonso (1), holds for the frequency-space spectra function of the settlement, $S_Y(f, x)$:

$$S_Y(f, x) = |H_Y(f)|^2 S_{q_f}(f, x) \tag{16}$$

where

$$S_Y(f, x) = \int_{-\infty}^{\infty} R_Y(\tau, x)e^{-i2\pi f\tau}d\tau, \tag{17}$$

$$R_Y(\tau, x) = E[Y(x - \tau/2)Y(x + \tau/2)], \text{ and} \tag{18}$$

$$H_Y(f) = \int_{-\infty}^{\infty} h_Y(\gamma)e^{-i2\pi f\gamma}d\gamma. \tag{19}$$

$H_Y(f)$ is the frequency response function of the system. The simple expression given by Eq. 16 enables the frequency-space spectra function of the settlement to be computed

analytically; then, inverse Fourier operations can be used to write

$$R_Y(\tau, x) = E[Y(x - \tau/2)Y(x + \tau/2)] = \int_{-\infty}^{\infty} S_Y(f, x)e^{i2\pi f\tau}df \tag{20}$$

The mean square value (variance, in this case) for the settlement is therefore

$$R_Y(0, x) = E[Y^2(x)] = Var[Y(x)] = \int_{-\infty}^{\infty} S_Y(f, x)df \tag{21}$$

This relationship will be used subsequently to derive the variance of the settlement. Note that the frequency response function, $H_Y(f)$, is invariant with the actual load distribution over the beam. When it is known, it can be applied to any configuration of external load. This function will be computed herein by using its definition as a starting point.

Settlement Frequency Response Function

The influence function, $h_Y(\gamma)$, which appears in Eq. 19, can be found from Hetenyi's elementary beam analysis (3).

$$h_Y(\gamma) = h_Y(x - a) = \frac{\lambda}{2\overline{K}} e^{-\lambda|x-a|}(\cos\lambda|x - a| + \sin\lambda|x - a|) \tag{22}$$

where $1/\lambda$ = characteristic length of the beam. It is defined by

$$1/\lambda = (4EI/\overline{K})^{1/4} \tag{23}$$

Because of the symmetry of $h_Y(\gamma)$, Eq. 19 can be simplified to

$$H_Y(f) = 2\int_0^{\infty} h_Y(\gamma)\cos 2\pi f\gamma d\tau = 2\int_0^{\infty} \frac{\lambda}{2\overline{K}} e^{-\lambda\tau}(\cos\lambda\tau + \sin\lambda\tau)\cos 2\pi f\tau d\tau$$

which, after integration and substitution of the dimensionless frequency, $F = f/\lambda$, becomes

$$H^2_{Y_{ad}} = \frac{1 + \pi F}{1 + (1 + 2\pi F)^2} + \frac{1 - \pi F}{1 + (1 - 2\pi F)^2} \tag{24}$$

where $H^2_{Y_{ad}}$ = dimensionless frequency response function. The plot of this function in Figure 4 shows the dominant influence of this weighting function in the dimensionless frequency interval -0.3 to 0.3. Although there is no practical significance to a negative frequency, the mathematical formulation of the 2-sided spectra, $S_{q_f}(f, x)$ and $S_Y(f, x)$, uses negative frequencies in a conceptual way.

Analysis of Load Conditions

The next step in this analysis requires the consideration of specific loading conditions including concentrated vertical load, concentrated moment, and uniform continuous vertical load over finite length. According to Eq. 16 the loading conditions are reflected only in $S_{q_f}(f, x)$, the frequency space density function of the fictitious load, q_f.

By using the definition given by Eqs. 15 and 18, we will calculate this function for specific fundamental types of loading. The actual load enters this expression through the deformation, $\overline{Y}(\cdot)$, that it causes in a beam resting on a base with mean characteristics, $\overline{K}$; only the case for constant mean value of K has been considered herein. Although analyses for more complex mean values do not introduce any conceptual changes, they will lead to difficulties in obtaining the required integrations.

The soil influence in Eq. 15 enters through the autocorrelation function, $R_K(\tau)$. Arbitrary autocorrelation functions from observed data can be either approximated by simple mathematical expressions suitable for analytical development in Eq. 15 or introduced in their actual form with the use of some numerical integration procedure, such as the fast Fourier transform (2). The first procedure is best suited to provide a systematic picture of the influence exerted by the various parameters affecting the beam behavior, and it will be used in this study. However, numerical procedures will be required to handle the detailed analysis of a particular case that might involve soil autocorrelation functions that differ significantly from the family used herein.

According to Ignatov and Vershinin (4), Sobolev proposed the following simple decaying exponential type of function for $R_K(\tau)$:

$$R_K(\tau) = Be^{-a|\tau|} \tag{25}$$

B can be identified with the variance of the subgrade coefficient; a governs the correlation dependence of the coefficient of soil reaction with distance. The same form of autocorrelation function was found by Alonso (1) in a study of the random function characterization of 20 deep static sounding records of homogeneous sandy soils (5). The parameters that characterize a particular type of soil are $\overline{K}(x)$ and B, the mean value and variance respectively of the coefficient of subgrade reaction and the coefficient a, a measure of the degree of correlation between the values of K(x) along the beam. High values of a imply that successive values of K(x) along the beam are relatively independent of each other, whereas low values of a indicate significant correlations over long distances.

The specific values for $\overline{K}(x)$, B, and a for use in a particular study can be properly chosen only if adequate records of K(x) with distance are available within the immediate vicinity; the methods and techniques used in analyses of this type have been discussed by Alonso (1). But, if data are limited, a reliable estimate for $\overline{K}(x)$ and B can be obtained in most cases, and approximate bounds for a, which requires continuous or quasi-continuous records, can be deduced from general trends based on studies of existing records. For example, in a study of 17 vertical records of soil properties ranging from Atterberg limits to bearing pressure in static sounding tests in a variety of soil types, Alonso (1) found that the numerical value of parameter a oscillated between 0.16 and 1.90 m^{-1}. Further studies of this type are necessary before narrower limits can be determined for different soils and properties.

Infinite Beam With Concentrated Load

The deflection of a beam resting on a soil with a constant subgrade coefficient because of a load, P, can be written from Eq. 22 as

$$\overline{Y}(x) = \frac{P\lambda}{2\overline{K}} e^{-\lambda|x|}(\cos\lambda|x| + \sin\lambda|x|) \tag{26}$$

By introducing the dimensionless variables

$$X = x\lambda \quad , \quad Z = \tau\lambda \quad , \quad \text{and} \quad A = a/\lambda \tag{27}$$

the expression for S_{q_t} becomes

$$S_{q_f} = \frac{P^2\lambda B}{4\bar{K}^2} \int_{-\infty}^{\infty} (\cos|X + Z/2| + \sin|X + Z/2|)(\cos|X - Z/2| + \sin|X - Z/2|)$$

$$\cdot e^{-A|Z|}e^{-|X + Z/2|}e^{-|X - Z/2|}e^{-j2\pi FZ}dZ \tag{28}$$

Integration of Eq. 28 yields, according to Alonso (1),

$$S_{q_f} = \frac{P^2B}{\bar{K}^2} S_{q_{fad}} \tag{29}$$

where $S_{q_{fad}}$ = dimensionless function depending on F, X, and A. Defining a dimensionless expression for the frequency-space spectra density function of the settlement, Y, as

$$S_{Y_{ad}} = \frac{\bar{K}^4 S_Y}{P^2\lambda B} \tag{30}$$

we can write the dimensionless counterpart of Eq. 16 as

$$S_{Y_{ad}} = |H_{Y_{ad}}|^2 S_{q_{fad}} \tag{31}$$

As noted by Bendat and Piersol (2), Eq. 21, which relates the mean square values of the settlement to the frequency-space density function, suggests that the function S_Y can be interpreted as the distribution of the variance in the frequency-space plane. Hence, additional information should be obtained for the range of frequencies that exert the maximum influence on the mean square value considered. Figure 5 shows a dimensionless plot of S_Y as a function of frequency for some particular values of the parameters involved; as before, the presence of negative frequency values is merely a mathematical convenience. The frequencies near zero influence the mean square value most significantly, and there is rapid decay in the area under the curves with increases in the longitudinal coordinate, X. A similar trend is observed for parameter $A = a/\lambda$, which defines the autocorrelation function of the soil reaction coefficient.

The final goal of calculating the mean square value or variance, Ψ_Y^2, of the settlement along the beam is accomplished by use of Eq. 21 in terms of dimensionless parameters. If we define

$$\Psi_{Y_{ad}}^2 = \frac{\bar{K}^4}{P^2\lambda^2 B} \Psi_Y^2 \tag{32}$$

then the corresponding dimensionless version of Eq. 21 is easily established to be

$$\Psi_{Y_{ad}}^2 = \int_{-\infty}^{\infty} S_{Y_{ad}} dF \tag{33}$$

This is the expression that has been used to compute the variances. The complexity of the expression for $S_{Y_{ad}}$ necessitated the use of a computer to perform the integrations. The numerical integration involved a parabolic composite scheme with variable spacing along F according to the rate of change of the S_Y function. It did not present any difficulty because of the rapid decay in the frequency-space spectra functions for increasing values of F. As expected, the more rapid the oscillation of soil properties, the smaller the influence that can be attributed to them. Figure 6 shows the result of this computation in terms of dimensionless parameters, and it illustrates the variation of the variance with distance from the load and the soil parameter a. As one could anticipate, the maximum variability in the results occurs immediately under the load. Also,

Figure 6. Settlement variance versus distance to load for concentrated load.

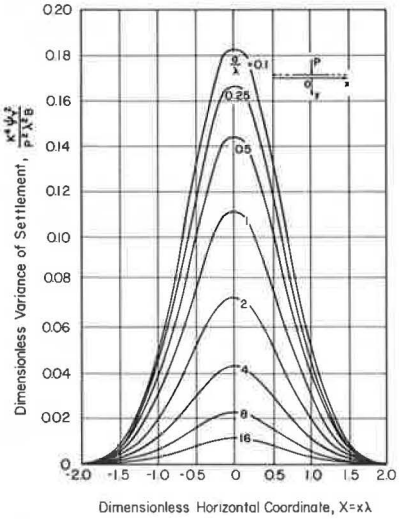

Figure 7. Settlement spectrum versus frequency for concentrated moment.

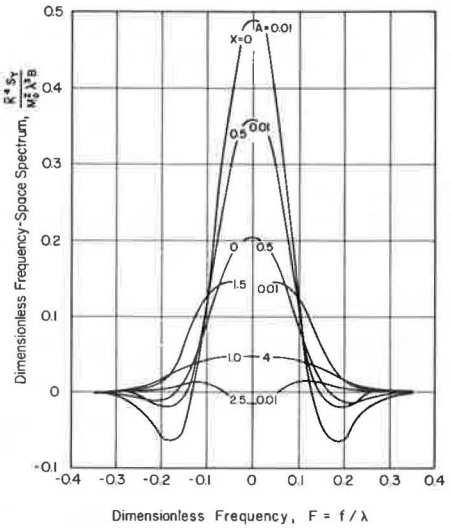

Figure 8. Settlement variance versus distance to load for concentrated moment.

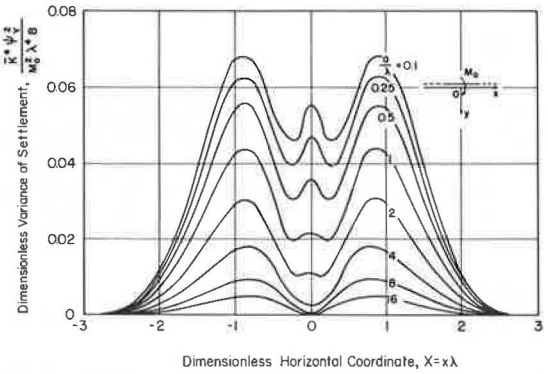

Figure 9. Settlement spectrum versus frequency for uniform load.

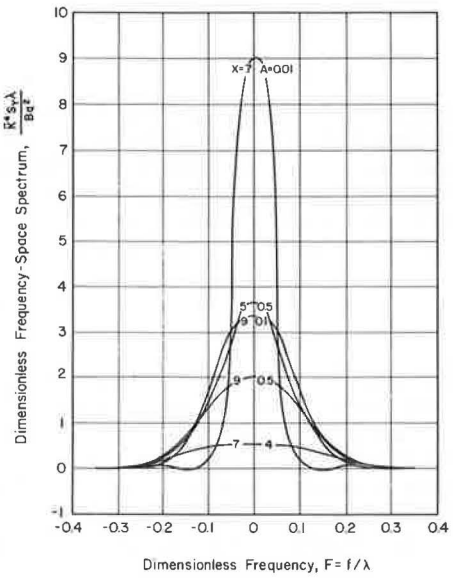

the uncertainty introduced by soil heterogeneity at a distance of 2 characteristic lengths from the location of the load is negligible compared to the uncertainty at the location of the load. The formulation of the problem in dimensionless terms indicates the general dependence of the mean square values on the parameters defining the beam characteristics. In fact, the variance of the settlement given by Eq. 32 can be written as

$$\Psi_Y^2 = \frac{P^2\lambda^2 B}{\bar{K}^4}\Psi_{Y_{ad}}^2 = \frac{P^2 B}{2(EI)^{1/2}K^{7/2}}\Psi_{Y_{ad}}^2 \tag{34}$$

Thus, larger loads and larger variances in the soil reaction coefficient, B, will lead to a larger expected variability in the settlement. Note also the strong influence of the mean soil parameter, $\bar{K}$, in reducing the uncertainty.

Infinite Beam With Concentrated Moment

The deflection of an infinite beam because of a concentrated moment, M_0, at the origin can be written as follows (3):

$$\bar{Y}(x) = \frac{M_0\lambda^2}{\bar{K}} e^{-\lambda x}\sin\lambda x \qquad x \geq 0 \tag{35}$$

$$\bar{Y}(x) = \frac{M_0\lambda^2}{\bar{K}} e^{\lambda x}\sin\lambda x \qquad x \leq 0 \tag{36}$$

When the operations involved in Eqs. 15 and 16 were carried to completion, a dimensionless form of the frequency-space spectra of the settlement due to a concentrated moment was found to be as follows (1):

$$S_{Y_{ad}} = \frac{\bar{K}^4}{BM_0^2\lambda^3} S_Y \tag{37}$$

in terms of which the relationship given by Eq. 33 still holds. Figure 7 is a plot of this function for a few particular values of the parameters X (dimensionless length along the beam) and A = a/λ (definition of the autocorrelation function of the soil). Frequencies near zero are the most significant. Values of F larger than 0.3 do not contribute appreciably to the variance, and we observe a general decay in the area under the curves for increasing values of A and X. If we define

$$\Psi_{Y_{ad}}^2 = \frac{\bar{K}^4\Psi_Y^2}{M_0^2\lambda^4 B} \tag{38}$$

then Eq. 33 can be used to compute the variance of the settlement along the beam by the same numerical technique mentioned previously. Figure 8 shows the resulting values for the dimensionless variance as a function of the parameter a/λ and the distance from the point of application of the load. The maximum uncertainty occurs at a distance of about 1 characteristic length from the origin, and, at a distance of 3 characteristic lengths, the randomness of the settlement is negligible. Additional information on the variables affecting the variance can be obtained by writing Ψ_Y^2 as

$$\Psi_Y^2 = \frac{M_0^2\lambda^4 B}{\bar{K}^4}\Psi_{Y_{ad}}^2 = \frac{M_0^2 B}{4EI\bar{K}^3}\Psi_{Y_{ad}}^2 \tag{39}$$

Note the larger influence of the rigidity of the beam in reducing the variance, as compared to that for a single vertical load. Again, the applied moment and the variance of the soil properties contribute to the uncertainty in the settlement, whereas the mean coefficient of soil reaction does the opposite.

Infinite Beam With Uniformly Distributed Load

The deflection of a beam under a uniform load distributed along a distance 2ℓ can be written as follows (3):

$$y = \frac{q}{2\bar{K}}\left[e^{\lambda x}\cos\lambda x - e^{-\lambda(2\ell - x)}\cos\lambda(2\ell - x)\right] \quad \text{if } x \leq 0 \tag{40}$$

$$y = \frac{q}{2\bar{K}}\left[2 - e^{-\lambda x}\cos\lambda x - e^{-\lambda(2\ell - x)}\cos\lambda(2\ell - x)\right] \quad \text{if } 0 \leq x \leq 2\ell \tag{41}$$

$$y = \frac{-q}{2\bar{K}}\left[e^{-\lambda x}\cos\lambda x - e^{-\lambda(x - 2\ell)}\cos\lambda(x - 2\ell)\right] \quad \text{if } x \geq 2\ell \tag{42}$$

when the origin is located at the left extremity of the loaded zone. As before, a closed form solution can be found for S_{q_f} when the integration indicated in Eq. 15 is performed. A more convenient dimensionless form for S_{q_f} can be shown as follows (1):

$$S_{q_{f\,ad}} = \frac{\lambda \bar{K}^2}{Bq^2} S_{q_f} \tag{43}$$

This expression can be used to compute the frequency-space density function of the random settlement, $S_Y(f, x)$. Figure 9 shows the behavior of this function for $2\ell = 10/\lambda$ and for several particular values of the parameters A and X. Again, only the frequencies near zero have a significant influence on the mean square values; note also the influence of A in spreading the range of influence of F. If we define the dimensionless version of the variance of the settlement as

$$\Psi^2_{Y_{ad}} = \frac{\bar{K}^4}{Bq^2} \Psi^2_Y \tag{44}$$

Eq. 33, which was established for a single concentrated load, can be used here without modification to compute the variance of the settlement by means of the same numerical procedure mentioned previously. Figure 10 shows the final results of these computations for different values of the parameter $L = \lambda\ell$. Observe the slow decay of the variance in the region beyond the loaded interval for small values of the loaded length (compared to the characteristic length of the beam, $1/\lambda$). However, when L increases, the significant randomness of the settlement is limited to the loaded length, as shown in Figure 10d. The almost constant value assumed for Ψ^2_Y within the interval is shown in Figure 10d. A somewhat different behavior is observed in this regard when L decreases as illustrated in Figures 10a and 10b. In general, the point of maximum uncertainty is located at the middle of the loaded zone. Figure 11 shows the dependence of the variance values and the length ℓ for the central point of the loaded zone. After a region of rapid increase of Ψ^2_Y for values of L where 2L is less than 3.5, a fairly constant value of Ψ^2_Y exists. As in the preceding cases, the expression for the variance may be rewritten in terms of the dimensionless factor $\Psi^2_{Y_{ad}}$ to examine the effect of the variables involved on the variance of the settlement:

$$\Psi^2_Y = \frac{Bq^2}{\bar{K}^4} \Psi^2_{Y_{ad}} \tag{45}$$

Again, the magnitude of the applied load and the soil variance have a positive influence in increasing the uncertainty of settlement, whereas the mean soil reaction coefficient has the opposite effect.

The general case in which the load extends over an infinite beam can be viewed as a superposition of the types of loads considered. It was noted previously that the load distribution enters the analysis through the deformation, $\bar{Y}(x)$, produced in the beam resting on a foundation with a deterministic mean soil coefficient. Because the linearity

Figure 10. Settlement variance versus distance for uniform load.

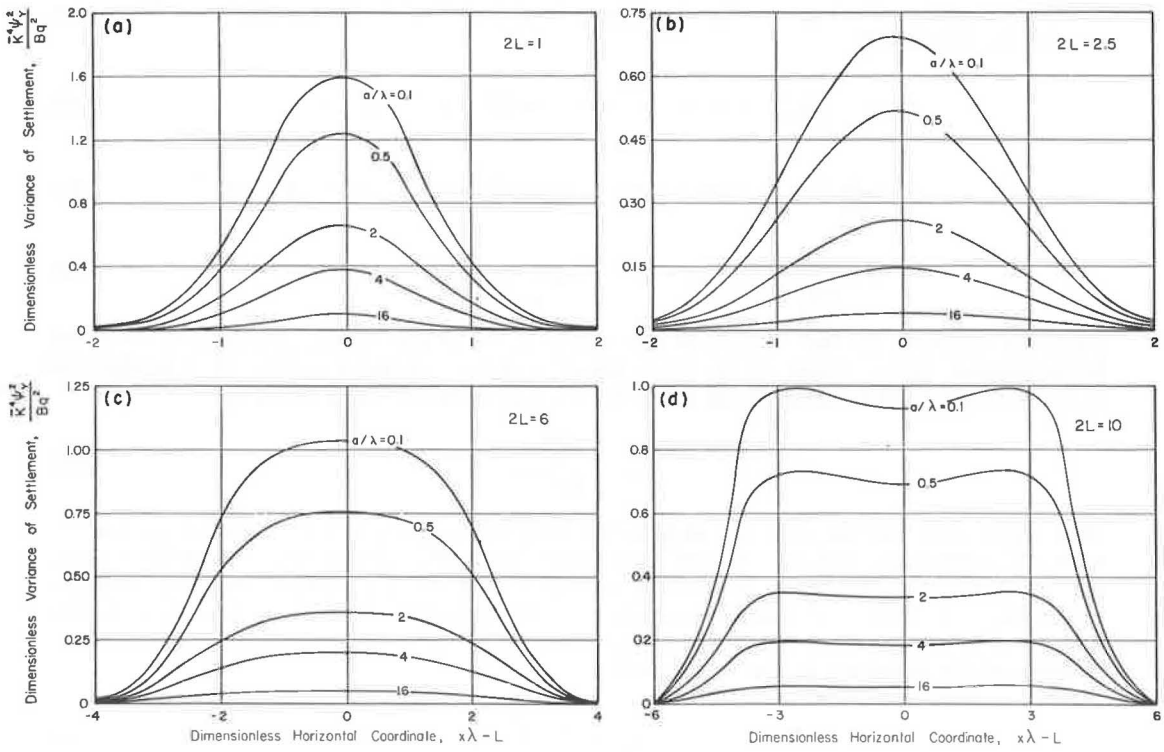

Figure 11. Settlement variance at center point versus loaded length.

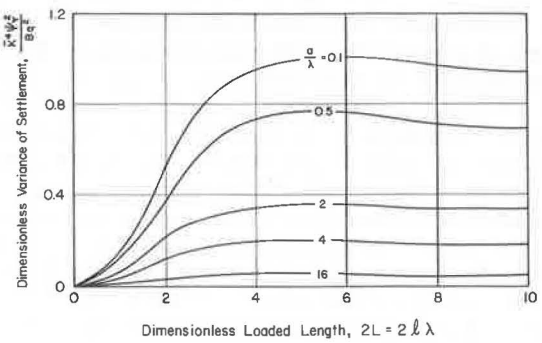

of the problem enables such a deformation to be considered as the superposition of deformations caused by basic types of load, one is tempted to add the variance contributions for each type of load. However, Eq. 15 for S_{q_i} has a nonlinear character in $\overline{Y}(\cdot)$ as illustrated by Eq. 18. Because this will give rise to mixed terms not directly considered herein, an analysis similar to this must be performed on the mixed terms. In general, only double products of the settlement functions considered here will appear in Eq. 15.

EXAMPLE

To illustrate the applicability and proper implementation of the preceding results in practical cases, consider the hypothetical example of a reinforced concrete prismatic beam resting on a sandy soil whose reaction is assumed to be of the Winkler type. From previous experience and a random function analysis of actual soil data (1), the coefficient of soil reaction can be approximated by a homogeneous random process with an assumed constant mean of 8 kg/cm^3 and a coefficient of variation of 0.2. The autocorrelation function can be described by an exponentially decaying function in which the parameter a is chosen to be 1 m^{-1}. The cross section of the beam is an inverted symmetric T (the larger side is in contact with the soil) with an effective elastic modulus of 200 000 kg/cm^2, dimensions of 50 by 20 cm and 20 by 20 cm for the lower part and upper part respectively, and a uniformly distributed load of 50 ton/m over a length of 20 m. The longitudinal dimension of the beam is sufficiently long to justify the assumption of an infinite length for purposes of settlement calculations.

Equation 23 where $\overline{K} = bK_0$ can be used to find $1/\lambda = 2$m; therefore, $2L = 2\ell/\lambda = 10$ and $a/\lambda = 2$. The maximum dimensionless variance, $\overline{K}^4\Psi_Y^2/Bq^2$, for a large portion of the beam can be found from Figure 10c to be 0.34. Using these values, we obtain $\Psi_Y^2 = \text{Var}(Y) = 0.0206$ cm^2; the standard deviation for the settlement is $\sigma_Y = 0.144$ cm. A deterministic analysis based on Eq. 41 shows that the mean settlement, $\overline{Y}$, for the center of the loaded zone is 1.25 cm; hence, a coefficient of variation of 0.144/1.25 = 0.115 is found for the settlement of the beam.

If no further assumptions are made concerning the probabilistic structure of K(x), one is forced to use nonparametric statistics to obtain confidence intervals for the settlement. In many cases, however, a normality assumption is justified; it suffices to check this assumption only in the process describing the soil behavior because the differential equation governing the phenomenon is linear and the preservation of the normality condition is thereby guaranteed. Even if the soil coefficient process departs slightly from normality, this assumption will still give more accurate results than the use of nonparametric statistics, because the complete generality of its assumptions usually leads to very conservative statements. Suppose, for example, that one is interested in a 90 percent confidence interval for the settlement of the center point of the loaded zone. If a normal model is used, the unit normal variate, u, becomes 1.65 and limits of 1.01 cm and 1.49 cm can be established for the settlement. When a normal model is justified, the determination of the degree of randomness involved in the total settlement is a straightforward exercise.

An estimate of the maximum differential settlement at a given significance level poses a more difficult problem. Because differential settlement is associated with a distance between 2 points of interest, the probabilistic dependence of these 2 points must be investigated. Although the nonhomogeneous autocorrelation function provides a first approximation for such information for a nonhomogeneous process, the 2-dimensional function is not known in this case and a rigorous analysis cannot be undertaken. In this context we may employ the heuristic argument that, if 2 points are uncorrelated for soil characteristics, it is unlikely that the settlement at those 2 points will be correlated; this reasoning defines, by a simple examination of the autocorrelation function, a distance between points where independence of the random variables defining the settlement can be assumed. In this case ($a/\lambda = 2$) the distance can be fixed as 5 m according to Eq. 25, provided correlations smaller than 10 percent of the variance are taken as a virtual lack of correlation. Within the framework of a normal model, consider now the random variables defining the settlement at 2 different points x_1 and x_2

$$Y_1 = N(\overline{Y}_1,\ \sigma_{Y_1})$$

$$Y_2 = N(\overline{Y}_2,\ \sigma_{Y_2})$$

At a significance level of α, we are interested in the differential settlement, δ, so that $P[(Y_1 - Y_2) > \delta] = \alpha$. The random variable, $V = Y_1 - Y_2$, is characterized by its mean

$$\overline{V} = \overline{Y}_1 - \overline{Y}_2$$

and its variance

$$\mathrm{Var}(V) = \mathrm{Var}(Y_1) + \mathrm{Var}(Y_2) - 2\rho_{Y_1,Y_2}\sigma_{Y_1}\sigma_{Y_2}$$

The correlation coefficient, ρ_{Y_1,Y_2}, will become approximately zero if x_1 and x_2 are a distance, d, apart; in this case we have

$$\mathrm{Var}(V) = \mathrm{Var}(Y_1) + \mathrm{Var}(Y_2)$$

The variable V can be defined in terms of known quantities. Consider the 2 representative points $x_1 = 5$ m and $x_2 = 10$ m; for the first point we can use Eq. 41 to obtain $Y_1 = 1.29$ cm. Because the variance is almost identical at both locations, the differential settlement will behave as a normal random variable with a mean of 0.04 cm and a standard deviation of 0.202 cm. The probability of exceeding a differential settlement, δ, can be rewritten by using the unit normal variate, U, as follows:

$$P[(Y_1 - Y_2) > \delta] = 1 - P(V \leq \delta) = 1 - P\left(U \leq \frac{\delta - \overline{V}}{\sigma_U}\right) = 1 - F_U\left(\frac{\delta - \overline{V}}{\sigma_V}\right) = \alpha$$

At a 10 percent significance level, we get $F_U\left(\frac{\delta - \overline{V}}{\sigma_V}\right) = 0.9$, whereupon

$$\delta = 1.30\sigma_V + \overline{V} = 0.262 + 0.04 = 0.302 \text{ cm}$$

Note that only 13 percent of this settlement comes from the deterministic solution, although more unfavorable conditions can be found along the beam by studying the deterministic settlement curve. The above computations represent a differential settlement of 0.0006 cm/cm, which is significant only in very sensitive structures. Note, however, that this value can be increased if lower significance levels are desired. To find a more critical differential settlement along the beam, one can use a trial procedure and a comparison of the deterministic deformation law with the curve of variances to determine the worst situation.

DISCUSSION OF LIMITATIONS

The foregoing method of analysis uses a linearization procedure that is justified only when the dispersion of the coefficient of soil reaction is relatively small when compared to the mean value. If a completely different situation is encountered as would be the case when different soils are present, a larger dispersion in the settlement of the beam would be expected. A deterministic approach, however, can be attempted in this case if the extension of these heterogeneities can be evaluated. Engineering judgment will dictate the worst situation according to loading conditions.

The boundary conditions associated with beams of finite length do not allow the simplified analysis presented herein to be applied; in fact, the influence factor, $h_Y(x, a)$, is no longer a function of x - a, and therefore the full nonhomogeneous case must be considered. In general, this leads to complex double integrals that require considerable computation. A superposition principle normally used for the finite beam in the deterministic case is not valid because of the cross correlations among the quantities involved. An analysis of such cross correlations would complicate the problem even more.

Finally, the autocorrelation function for the coefficient of soil reaction in this analysis has been assumed to be an exponentially decaying relationship. Although the qualitative conclusions based on this dimensionless analysis apparently are unchanged if another function is selected, different results will be obtained for the dimensionless variance of settlement.

CONCLUSIONS

Probability and random process theory provides a convenient and natural approach to the analysis of settlement based on levels of confidence.

Although there can be significant scatter in the total settlement computation, the proposed type of analysis allows a probabilistic evaluation of the scatter once the assumptions incorporated into the analysis are justified.

The random nature of the soil seems to affect the differential settlement less than the total settlement; however, because differential settlement may be important in delicate structures, confidence levels may have to be increased.

The so-called nondimensional variance takes on its maximum values near the loaded zone and, in general, decays rapidly with distance from the loaded area; this is less evident for uniform loads when small loaded lengths are encountered.

A dimensionless formulation of the problem allows the general dependence of the variance on the other parameters of the system to be established. The mean coefficient of soil reaction always exerts a strong influence on reducing uncertainty, which is maximum for a concentrated moment. The linear dependence between the variance of the settlement and the variance of the soil coefficient is apparent in all cases, whereas the mean square value of the settlement varies with the square of the applied load. Finally, the bending rigidity of the beam has a moderate influence on reducing the uncertainty of the settlement for the cases where the beam is loaded by a concentrated moment and a concentrated load.

REFERENCES

1. Alonso, E. E. Application of Random Function Theory to Settlement Problems in Soil Engineering. Dept. Civil Engineering, Northwestern Univ., Evanston, Ill., PhD dissertation, 1973.
2. Bendat, J. S., and Piersol, A. G. Random Data: Analysis and Measurement Procedures. Wiley-Interscience, New York, 1971.
3. Hetenyi, M. Beams on Elastic Foundation: Theory With Applications in the Fields of Civil and Mechanical Engineering. Univ. of Mich. Press, Ann Arbor, Mich., 1946.
4. Ignatov, V. P., and Vershinin, S. A. A Numerical Method for the Analysis of Finite Beams on a Statistically Nonhomogeneous Foundation. Osnovaniya, Fundamenty i Mekhanika Gruntov, Vol. 3, 1970, pp. 7-9.
5. Schmertmann, J. H. Dutch Friction Cone Penetrometer Exploration of Research Area at Field 5, Eglin AFB, Fla., Rept. No. S-69-4, U.S. Army Engineer Waterways Experiment Station, Vicksburg, Miss., 1969.

SPONSORSHIP OF THIS REPORT

GROUP 2—DESIGN AND CONSTRUCTION OF TRANSPORTATION FACILITIES
W. B. Drake, Kentucky Department of Transportation, chairman

SOIL MECHANICS SECTION
John A. Deacon, University of Kentucky, chairman

Committee on Strength and Deformation Characteristics of Pavement Sections
Richard D. Barksdale, Georgia Institute of Technology, chairman
Stephen F. Brown, B. E. Colley, Hsai-Yang Fang, F. N. Finn, R. G. Hicks, Frank L. Holman, Jr., Ignat V. Kalcheff, Bernard F. Kallas, William J. Kenis, Thomas W. Kennedy, Milan Krukar, H. Gordon Larew, Kamran Majidzadeh, William M. Moore, Quentin Robnett, Eugene L. Skok, Jr., Ronald L. Terrel

Committee on Embankments and Earth Slopes
Lyndon H. Moore, New York State Department of Transportation, chairman
Raymond A. Forsyth, David S. Gedney, Roger D. Goughnour, Wilbur M. Haas, William P. Hofmann, Henry W. Janes, Philip Keene, Charles C. Ladd, Richard E. Landau, Harry E. Marshall, Glen L. Martin, R. M. Mattox, Melvin W. Morgan, Robert L. Schuster, Edgar Pierron Ulbricht, Walter C. Waidelich, William G. Weber, Jr., Donald L. York

Committee on Foundations of Bridges and Other Structures
M. T. Davisson, University of Illinois, chairman
David R. Antes, Edwin C. Beethoven, William Bootz, Bernard E. Butler, Harry M. Coyle, Jacob Feld, Frank M. Fuller, David S. Gedney, Stanley Gordon, Bernard A. Grand, Robert J. Hallawell, T. J. Hirsch, Horace E. Hoy, Hal W. Hunt, Philip Keene, Richard E. Landau, Clyde N. Laughter, G. A. Leonards, R. M. Mattox, Thomas D. Moreland, A. Rutka

Committee on Subsurface Soil-Structure Interaction
Ernest T. Selig, State University of New York at Buffalo, chairman
Jay R. Allgood, Mike Bealey, Bernard E. Butler, T. Y. Chu, Hameed A. Elnaggar, Lester H. Gabriel, Delon Hampton, John G. Hendrickson, Jr., Raymond J. Krizek, Don A. Linger, Steven Majtenyi, F. Dwayne Nielson, Harry H. Ulery, Jr., R. K. Watkins

Committee on Mechanics of Earth Masses and Layered Systems
Russell A. Westmann, University of California at Los Angeles, chairman
Richard G. Ahlvin, Richard D. Barksdale, A. Alexander Fungaroli, Charles M. Gerrard, Delon Hampton, M. E. Harr, Robert L. Kondner, Raymond J. Krizek, Fred Moavenzadeh, Keshavan Nair, Robert L. Schiffman, Awtar Singh, Robert D. Stoll, Aleksandar S. Vesic, Harvey E. Wahls, William G. Weber, T. H. Wu

John W. Guinnee, Transportation Research Board staff

Sponsorship is indicated by a footnote on the first page of each report. The organizational units and the chairmen and members are as of December 31, 1973.